Construction of Novel Semi-Empirical Tire Models for Combined Braking and Cornering

Gäfvert, Magnus; Svendenius, Jacob

2003

Document Version:
Publisher's PDF, also known as Version of record

ISSN 0280–5316
ISRN LUTFD2/TFRT--7606--SE

Construction of Novel Semi-Empirical Tire Models for Combined Braking and Cornering

Magnus Gäfvert
Jacob Svendenius

Department of Automatic Control
Lund Institute of Technology
April 2003

Contents

1. Introduction

The forces generated in the contact between the tires and the road are of major importance for the dynamic behavior of a road vehicle. Hence, accurate tire models are necessary components of complete vehicle models aimed at analyzing or simulating vehicle motion in real driving conditions. There are many previous models which describe the tire-forces generated at conditions of pure braking, driving, or cornering, as well as models which describe the tire forces resulting from mixed conditions of simultaneous braking (or driving) and cornering. Some models are theoretical in the sense that they aim at modeling the physical processes that generate the forces. Other models are empirically oriented and aim at describing observed phenomena in a simple form. Theoretical models are generally based on simplifying assumptions which limit their practical use. They often involve parameters which are difficult to identify. Empirical models are, in general, based on functional approximations of experimental data. Pure-condition tire-forces may be described well by rather compact and simple empirical models that are widely accepted. Pure-slip tire data from test-bench experiments are often available for calibration. The situation for mixed conditions is somewhat different. The transition from one to two dimensions makes it more difficult to apply functional approximation. Empirical models tend to be either rough approximations or quite complex and difficult to understand. Accurate models rely on parameters that need to be calibrated with mixed-condition experimental data. This is a drawback since such data are only rarely available for a specific tire.

The main result in this report is the derivation of a mixed-condition model that is based on pure-condition models and do not rely on available combined-slip data for calibration. The idea behind the proposed model is to extract enough information from pure-condition empirical models to construct the mixed-condition tire-forces. The procedure is based on the standard brush-model for tire mechanics in which the rubber layer of the tire is modeled as elastic bristles. The proposed model has several attractive features:

- It reduces exactly to the empirical model at pure-slip.
- It gives a smooth transition from small-slip to large-slip behaviour which agrees with empirical observations.
- Only few parameters are needed which all have clear physical interpretations.
- Nominal parameter values may be derived automatically from the empirical pure-slip models.
- The model does not include any singular expressions.
- Differences between driving and braking conditions are accounted for.
- Velocity dependence is included even when using velocity-independent pure-slip models.

The remaining part of this section describes the qualitative behaviour of pneumatic tires. Definitions commonly used in tire modeling are introduced. A brief survey of previous models for tire-force generation then completes the introduction. In Section 2 the theoretical brush-model is presented. Section 3 presents a procedure to decompose empirical pure-condition tire-forces into components of adhesive forces and sliding forces. It is described how mixed-condition forces may be constructed from these components. In Section 4 semi-empirical models of mixed-condition tire-forces are described. Practical implementation of the models is discussed. Results and validation of the models are then presented in Section 5. The report concludes with a summary in Section 6.

For convenience the following notations will be used: Vectors are used to describe planar entities and are therefore assumed to have two components unless

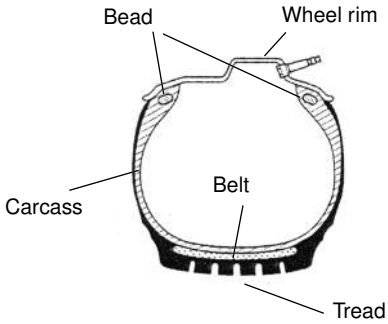

Figure 1 Schematic of a radial truck tire. (Reprinted from [3].)

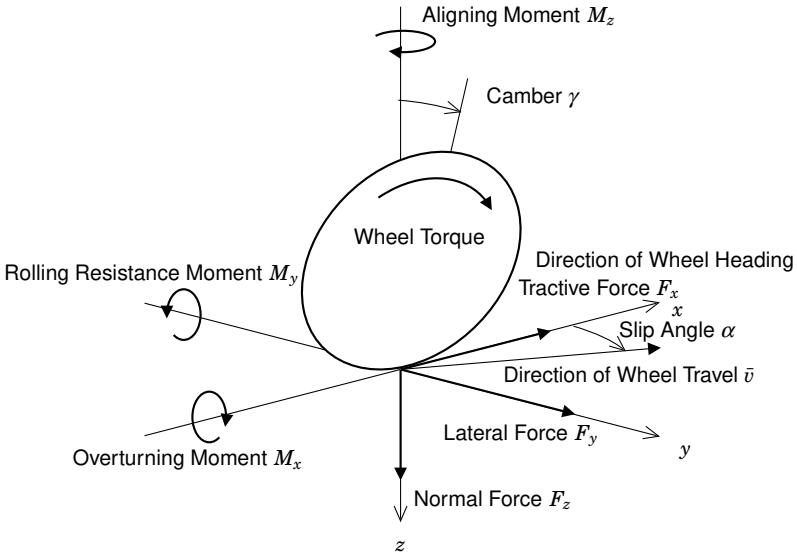

Figure 2 Forces and moments acting on a tire [27].

stated otherwise. Vectors are denoted by a bar as in $\bar{v}$, and the corresponding components and magnitude are denoted by v_x, v_y, and v.

1.1 The Tire

The now predominating radial tire [3] is built on a carcass of steel cords running radially from bead to bead. The beads clamp the tire to the wheel rim. A stabilizing belt of crossed steel-cords surrounds the carcass. The rubber tread is bonded on the belt and sculpted with a tread pattern. See Figure 1. In the contact patch between the tire and the road the rubber is partly gripping and partly sliding on the road surface, resulting in adhesive and sliding forces. The adhesive force is generated by elastic deformation of the tire and the sliding force from sliding friction. Hence, different physical processes are present simultaneously in different regions of the contact patch. The generated forces under different driving conditions depend on the motion of the tire carcass relative to the road. There are various ways to describe this motion depending on choice of reference systems and normalizations. The choice of reference system in this work largely follows the SAE standard [27], with the longitudinal x-axis aligned with the wheel heading, the lateral y-axis perpendicular to the wheel, and the vertical z-axis pointing downwards, as of Figure 2. The forces of interest in vehicle-handling studies are the planar lateral and longitudinal forces, F_x and F_y, and the self-aligning mo-

ment M_z. The longitudinal tire force F_x is generated when braking or driving[1], and the lateral force F_y and the torque M_z when cornering. The self-aligning moment results from the fact that the planar forces have a point of action which is not positioned exactly under the wheel center. The rolling-resistance and overturning moment are not of primary interest for vehicle handling and will not be regarded in the following. Likewise, it will be assumed that the camber angle γ is zero. For heavy vehicles this is normally a reasonable approximation.

1.2 Tire Kinematics

This section describes the relevant tire kinematics and definitions that are used in the following. Refer to Figure 3 for illustration of the described entities.

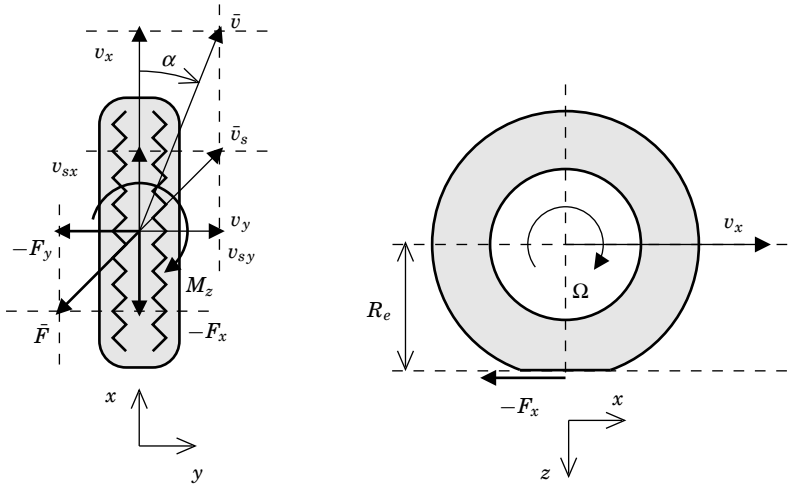

Figure 3 Kinematics of an isotropic tire during braking and cornering. Force vectors are also included. (Left: top view; Right: side view)

The *wheel travel velocity* $\bar{v} = (v_x, v_y)$ deviates from the wheel heading by the slip angle α

$$\tan(\alpha) = \frac{v_y}{v_x} \tag{1}$$

The *circumferential velocity* of the wheel is

$$v_c = \Omega R_e \tag{2}$$

where Ω is the *wheel angular velocity*, and R_e the effective *rolling radius* of the tire. The *slip velocity*, or the relative motion of the tire in the contact patch to ground, is

$$\bar{v}_s = (v_x - v_c, v_y) \tag{3}$$

The direction of the slip velocity is denoted by

$$\tan(\beta) = \frac{v_{sy}}{v_{sx}} \tag{4}$$

In tire modeling the slip velocity is often normalized with a reference velocity, to yield a dimensionless *tire-slip* entity. Common slip definitions are

$$\bar{\sigma} = \frac{\bar{v}_s}{v_c} \tag{5a}$$

$$\bar{\kappa} = \frac{\bar{v}_s}{v_x} \tag{5b}$$

$$\bar{s} = \frac{\bar{v}_s}{v} \tag{5c}$$

[1]In the following, when the word "braking" is used in the context of longitudinal tire force generation, this will actually mean "braking or driving" unless stated otherwise.

Note that the slips are collinear with the slip velocity $\bar{v}_s$. It is the custom to describe tire-forces as functions of the slip rather than the slip velocity. This convention is followed also in this work. Implicitly, this assumes that the forces do not depend on the magnitude of the slip velocity, v_s. In general, this is not true since at least the sliding friction normally depends on the velocity.

There are several conventions on how to define the tire slips, e.g. the ISO and SAE standards [17, 27] use $-100\kappa_x$ to represent longitudinal slip, and α for lateral slip. In this report the slips are defined such that signs are consistent for the different slip definitions, and such that a generated tire force has opposite sign to the slip. This means that braking or left cornering will result in positive slip and negative force. For convenience λ will be used to denote longitudinal slip as

$$\lambda = \kappa_x \tag{6}$$

The slip definitions of (5) have the drawbacks of singularities at wheel lock ($v_c = 0$), zero longitudinal speed ($v_x = 0$), and zero wheel travel speed ($v = 0$), respectively. Usually $\bar{\sigma}$ is used at driving and $\bar{\kappa}$ at braking conditions, since they are then upper bounded in magnitude by unity. The slip $\bar{s}$ may be convenient to use since it behaves properly for all nonzero vehicle speeds. It is straightforward to translate between the different slip representations

$$\bar{\sigma} = (\,\lambda, \tan(\alpha)\,)\,/(1-\lambda) = \frac{\bar{\kappa}}{1-\kappa_x} = \frac{\bar{s}}{\sqrt{1-s_y^2}-s_x} \tag{7a}$$

$$\bar{\kappa} = (\,\lambda, \tan(\alpha)\,) = \frac{\bar{\sigma}}{1+\sigma_x} = \frac{\bar{s}}{\sqrt{1-s_y^2}} \tag{7b}$$

$$\bar{s} = (\,\lambda\cos(\alpha), \sin(\alpha)\,) = \frac{\bar{\sigma}}{\sqrt{(1+\sigma_x)^2+\sigma_y^2}} = \frac{\bar{\kappa}}{\sqrt{1+\kappa_y^2}} \tag{7c}$$

1.3 Behaviour at Pure Braking or Cornering

At pure braking the lateral translational velocity is zero, $v_y = 0$, and therefore also the lateral slip is zero, $\alpha = 0$. Hence, the resulting tire-force is determined solely by the longitudinal slip λ. Normally the longitudinal force F_{0x} is parameterized in λ. In Figure 4 (left) the normalized longitudinal tire force F_{0x}/F_z at different slips λ in pure braking is shown for a typical truck tire on a steel surface. As can

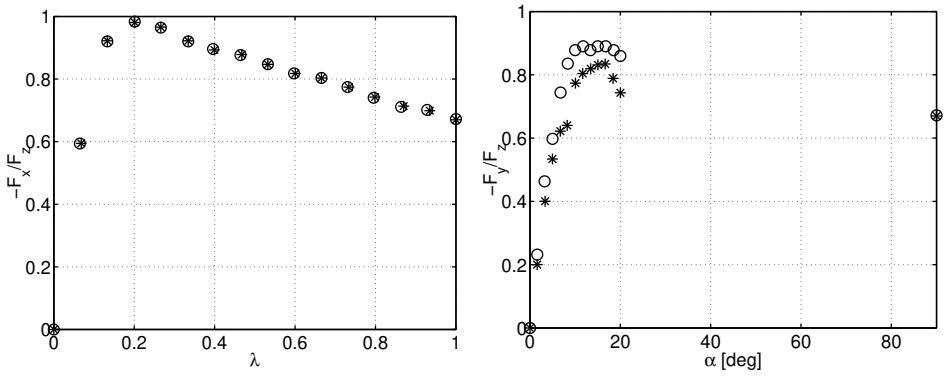

Figure 4 Normalized measured tire forces of a standard truck tire on steel surface at F_z = 20 (“o”), and 40 (“∗”) kN.[3] Left: Normalized longitudinal force at pure braking/traction. Right: Normalized lateral force at pure cornering. (Data from [10].)

be seen, the characteristics are highly non-linear. For small λ the longitudinal force appears to be approximately linear to the slip. Then a peak appears around

[3]Deficiencies in measured data have eliminated the dependence of the longitudinal-force F_x on the normal load F_z.

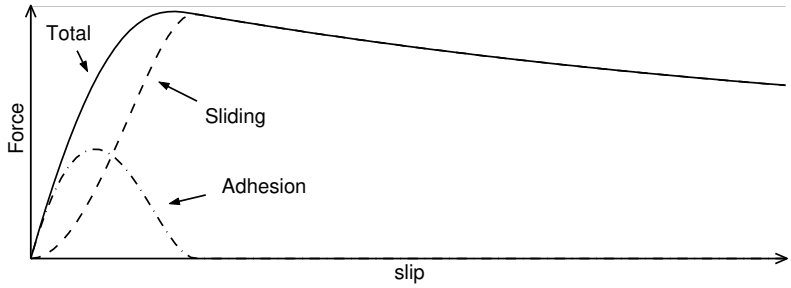

Figure 5 As the tire is partly gripping and partly sliding on the road surface the total tire force is composed of adhesive and sliding forces.

$\lambda = 0.2$. After the peak the force level out and decreases with increasing slips. The shape of the curve is due to the adhesive region of the contact patch getting smaller with increasing slips. At a certain slip there is no adhesion at all, and the force is generated entirely by sliding friction. The transition to full sliding occurs in the neighborhood of the peak value.

In pure cornering the circumferential velocity equals the longitudinal translational velocity, $v_x = v_c$, and therefore the longitudinal slip is zero, $\lambda = 0$. Hence, the resulting tire-force F_{0y} depends only on the lateral slip and is therefore normally parameterized in α. Figure 4 (right) shows the normalized lateral tire force F_{0y}/F_z for different slip angles at pure cornering. The shape is qualitatively the same as for the longitudinal force and reflects the transition from adhesion to sliding in the contact patch. The force peak is found around $\alpha = 15$ deg. The lateral friction is normally only measured for slip angles up to about 25 deg. Note that the force depends nonlinearly on the normal force F_z. This dependence is, e.g., due to changes in the pressure distribution of the normal force in the contact patch and changes of friction characteristics. In general the initial slope and peak value of F_{0y}/F_z decrease with increased load.

In Figure 5 is it illustrated how the total tire force has components resulting from the adhesive and sliding parts of the contact region.

The behavior described so far concerns steady-state conditions. For varying slips there are transient effects resulting from carcass deformation. Simply put, the tire act as a complex rolling spring when attached to a vehicle. The main observed effect of transient behavior is that it takes a specific rolling distance, the *relaxation length* σ_C, for the lateral slip to build up, and hence, the lateral force.

1.4 Behaviour at Combined Braking and Cornering

At combined braking and cornering the magnitude and direction of the resulting tire force depends on the magnitude and direction of the total slip vector. Figure 6 shows the resulting tire forces for two sets of total slips where the lateral slip is held fixed and the longitudinal slip is varied from free rolling ($\lambda = 0$) to locked wheel ($\lambda = 1$). The resulting lateral force decreases, compared to the pure cornering case, as the applied longitudinal slip increases. This effect may be explained by the decreasing size of the adhesive contact region as the total slip magnitude increases, and the projection of the friction force generated by the sliding region in both the longitudinal and lateral directions. The maximum available tire forces F_{0x}^* and F_{0y}^* at pure braking or cornering reflects the maximum available tire/road adhesion. Since the road adhesion provide a bound also on combined forces, the envelope of all possible curves as in the figure describes an ellipse-like shape, with corresponding major and minor axes defined by F_{0x}^* and F_{0y}^*. This envelope is commonly denoted as the *friction ellipse*.

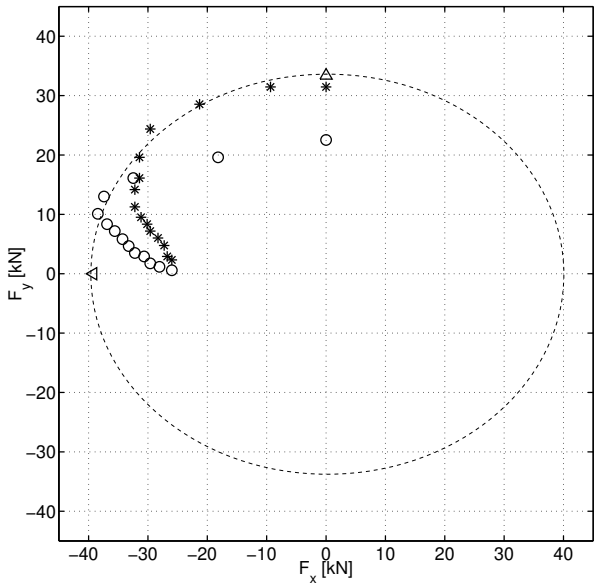

Figure 6 Measured combined tire forces of a standard truck tire on steel surface at $F_z = 40$ kN and $\lambda \in [0, 1]$ for $\alpha = -4.7°$ ("o"), and $\alpha = -9.8°$ ("∗"). The triangles denote the maximum achievable pure longitudinal and lateral forces (F_x^*, F_y^*) and defines the friction ellipse (dashed). (Data from [10].)

1.5 Tire Measurements

Measurements of tire characteristics are performed with test facilities where parameters such as the tire slips, normal load, and wheel travel velocity are controlled precisely while forces and moments are recorded. A common setup is to apply the loaded tire on a large rolling drum [16]. Another configuration is to translate a flat steel bar under the loaded tire [22]. Testing under real road-surface conditions may be performed with a test rig attached to a vehicle [25]. Some test facilities are limited to pure-slip or steady-state conditions, while others may be used to measure combined-slip conditions and transient behavior. Tests are normally performed by holding one slip constant, while sweeping the other. In general, the applied side-slip angles are smaller than around 15 degrees, and empirical tire-force data is normally only available up to this limit. Resulting data are of the type shown in Figures 4 and 6.

Generation of driving data requires more advanced test equipment than generation of braking data, since a motor for developing the traction torque then is necessary.

1.6 Practical Tire Models

The basic demand of a practical tire model is the ability to reproduce tire forces from compact and comprehensible mathematical expressions, using parameters that are easily obtainable and inputs that are measurable. Since the physical processes occuring in the contact region are difficult to model theoretically, practical tire models often describe resulting forces and moments in terms of empirical data, tire slips, and total normal forces. The empirical data inherently include the complex effects of friction, roughness, lubrication, deformation, etc.

Pure-slip models The *braking stiffness* C_λ and *cornering stiffness* C_α are defined as the linearization of the friction curves in Figure 4 at $\lambda = 0$ and $\alpha = 0$

[30]

$$C_\lambda = -\left.\frac{dF_{0x}}{d\lambda}\right|_{\lambda=0} \tag{8a}$$

$$C_\alpha = -\left.\frac{dF_{0y}}{d\alpha}\right|_{\alpha=0} \tag{8b}$$

The negative signs in (8b) is due to the fact that according to conventions the cornering and braking stiffnesses are defined to be positive. The stiffnesses may be used to model tire forces at pure braking or pure cornering for small tire slips as:

$$F_{0x}(\lambda) = -C_\lambda \lambda \tag{9a}$$

$$F_{0y}(\alpha) = -C_\alpha \alpha \tag{9b}$$

In some cases it is convenient to use the normalized *stiffness coefficients*:

$$C_{N,\lambda} = \frac{1}{F_z} C_\lambda \tag{10a}$$

$$C_{N,\alpha} = \frac{1}{F_z} C_\alpha \tag{10b}$$

A common way to include the transient effects resulting from the flexible carcass is to replace Equation (9b) with the linear time-variant differential equation

$$\frac{\sigma_C}{v_c}\frac{dF_{0y}}{dt} + F_{0y} = C_\alpha \alpha \tag{11}$$

where the time constant depend on the circumferential velocity v_c [23].

For larger slips the nonlinear characteristics of the friction curves need to be modeled. The now predominating model is the "Magic Formula" [1], which is a functional approximation of the lateral and longitudinal tire forces, as well as aligning torque, on the form

$$y(x) = D\sin(C\arctan((1-E)x + (E/B)\arctan(Bx))) \tag{12}$$

where (x, y) is (λ, F_{0x}), (α, F_{0y}), or (α, M_{0z}). The four coefficients have interpretations as stiffness factor (B), shape factor (C), peak factor (D), and curvature factor (E), and are unique for each of F_x, F_y, and M_z. Approximate normal load dependence may be introduced as $D = a_1 F_z^2 + a_2 F_z$, $BCD = (a_3 F_z^2 + a_4 F_z)/e^{a_5 F_z}$, and $E = a_6 F_z^2 + a_7 F_z + a_8$, or with the slightly modified expressions of [2]. Fit to experimental data is performed by parameter optimization of B,C,D,E (for a fixed normal load), or $a_{1\ldots8}$ (for varying normal load). Another related model is the Burckhardt approach [18], in which another functional approximation is used.

Combined-slip models Based on the mechanics of the tire and the available empirical data, a number of criteria for combined models may be stated (in the spirit of [7]):

1. The combined force $\bar{F}(\lambda, \alpha)$ should preferably be constructed from pure slip models $F_{0x}(\lambda)$ and $F_{0y}(\alpha)$, with few additional parameters.

2. The computations involved in the model must be numerically feasible and efficient.

3. The formulas should preferably be physically motivated.

4. The combined force $\bar{F}(\lambda, \alpha)$ should reduce to $F_{0x}(\lambda)$ and $F_{0y}(\alpha)$ at pure braking or cornering:

$$\bar{F}(\lambda, 0) = [\, F_{0x}(\lambda), 0\,]$$
$$\bar{F}(0, \alpha) = [\, 0, F_{0y}(\alpha)\,]$$

5. Sliding must occur simultaneously in longitudinal and lateral directions.
6. The resulting force magnitudes should stay within the friction ellipse.
7. The combined force should be $\bar{F} = -F_z \mu \bar{v}_s / v_s$ for locked-wheel skid for tires with isotropic friction characteristics.

The most simplistic model of combined forces is based on the friction ellipse concept [30, 11, 21]. While the friction ellipse is the envelope of the maximum achievable forces, the ellipse is here used also for modeling intermediate forces. It is used to compute a combined lateral force $F_y(\alpha, \lambda)$ at a given longitudinal force F_x, and is based on the assumption

$$\left(\frac{F_x}{F_{0x}^*}\right)^2 + \left(\frac{F_y(\alpha, \lambda)}{F_{0y}(\alpha)}\right)^2 = 1 \tag{13}$$

where F_{0x}^* is the maximum achievable longitudinal force, and $F_{0y}(\alpha)$ the corresponding lateral force at pure slip

$$F_y(\alpha, \lambda) = F_{0y}(\alpha)\sqrt{1 - \left(\frac{F_x}{F_{0x}^*}\right)^2} \tag{14}$$

An objection to this model is the assumption (13), which is not true, since adhesion limits are not necessarily fully reached for combined forces in the interior of the friction ellipse.

Another simple model is the Kamm Circle [18], where the resultant force magnitude is described as a function of the total slip magnitude. The force and slip vectors are then assumed to be collinear, possibly with a corrective factor k_s:

$$F_x = F(s)\frac{s_x}{s} \qquad \text{and} \qquad F_y = k_s F(s)\frac{s_y}{s} \tag{15}$$

A drawback with this model is that longitudinal and lateral characteristics are assumed to be the same, modulo the corrective factor.

Some early efforts to model tire forces under combined-slip conditions are described and compared in [19]. One of the most well-known models is first presented in [20]:

$$F_x(\lambda, \alpha) = \frac{F_x(\lambda) F_y(\alpha) \lambda}{\sqrt{\lambda^2 F_y^2(\alpha) + \tan^2(\alpha) F_x^2(\lambda)}} \tag{16a}$$

$$F_y(\lambda, \alpha) = \frac{F_x(\lambda) F_y(\alpha) \tan(\alpha)}{\sqrt{\lambda^2 F_y^2(\alpha) + \tan^2(\alpha) F_x^2(\lambda)}} \tag{16b}$$

In [7] this model is shown to give incorrect result for small slips and a modified version is presented.

In [1], a procedure for computing combined forces for the Magic Formula is presented. It is essentially a refinement of the Kamm Circle for non-isotropic tire characteristics and a normalization of the slips to guarantee simultaneous sliding. The normalized slip

$$\sigma_N = \sqrt{\left(\frac{\sigma_x}{\sigma_x^*}\right)^2 + \left(\frac{\sigma_y}{\sigma_y^*}\right)^2} \tag{17}$$

is an entity that is less then one for non-sliding conditions. It is based on an elliptic assumption where σ_x^* and σ_y^* are the longitudinal and lateral slips that corresponds to full sliding for pure slips, normally taken as the slips at the peak values F_{0x}^*, and F_{0y}^*. Now the combined forces are computed as

$$F_x = -\cos(\beta^*) F_{0x}(\sigma_x^* \sigma_N) \qquad \text{and} \qquad F_y = -\varepsilon_d(\sigma_N) \sin(\beta^*) F_{0y}(\sigma_y^* \sigma_N) \tag{18}$$

with $\tan(\beta^*) \triangleq \frac{\sigma_y/\sigma_y^*}{\sigma_x/\sigma_x^*}$. For large slip conditions the factor $\varepsilon_d(\sigma_N)$ must be included to give correct direction of the resulting forces. The reason is the fact that for small slips real tire-forces are essentially produced by elastic deformation, and for large slips by sliding friction. Therefore slip vectors of the same orientation but different magnitudes may result in forces with different orientation. It is not clear how to determine $\varepsilon_d(\sigma_N)$, and in [2] a modified procedure was presented:

$$F_x = \cos\left((1-\vartheta)\beta^* + \vartheta\beta\right) F'_{0x} \qquad \text{and} \qquad F_y = \sin\left((1-\vartheta)\beta^* + \vartheta\beta\right) F'_{0y} \tag{19}$$

with $\vartheta \triangleq \frac{2}{\pi} \arctan(q_1 \sigma_N^2)$ and

$$F'_{0x} \triangleq F_{0x}(\sigma_N) - \text{sat}(\sigma_N) \left(F_{0x}(\sigma_N) - F_{0y}(\sigma_N)\right) \sin^2(\beta^*) \tag{20a}$$

$$F'_{0y} \triangleq F_{0y}(\sigma_N) + \text{sat}(\sigma_N) \left(F_{0x}(\sigma_N) - F_{0y}(\sigma_N)\right) \cos^2(\beta^*) \tag{20b}$$

The variables ϑ, F'_{0x}, and F'_{0y} describe the gradual change of orientation of the resulting force from adhesion to sliding. At large slip-magnitudes the force is collinear with the slip vector. In this new model only one parameter, q_1, is used.

In [4] a model for combined braking and cornering is presented, which is based on functional representation. The model is much inspired by the Magic Formula and uses functions based on arc tangents to describe forces under combined-slip conditions.

The recent COMBINATOR model [28, 26] is still a variation on the Kamm Circle. Here the tire force magnitude is described by

$$F = F_{0x}(s) \cos^2(\beta) + F_{0y}(s) \sin^2(\beta) \tag{21a}$$

and the combined forces as

$$F_x = F \cos(\beta) \qquad \text{and} \qquad F_y = F \sin(\beta) \tag{21b}$$

The model assumes collinearity between resulting force and the slip vector.

In [4] a model is presented that is based on functional representation much inspired by the Magic Formula. Functions based on arc tangents are used to describe forces under combined-slip conditions. In principle, these represent purely empirical weighting functions that are multiplied with pure-slip forces obtained with the Magic Formula. The latest formulation may be found in [24] and is also commercially available in the “DelftTyre” product series of TNO Automotive, Netherlands. The model needs to be calibrated with combined-slip data.

There are also less empirical models based on brush-type mechanics like e.g. [12, 13, 14]. They are derived from first principles under simplifying assumptions and rely on basic entities such as tire stiffness, normal load, slips, and road friction coefficients. The potential main advantage with first-principles models are their applicability on different road surface conditions. In practice, this is difficult since the physical processes are different on e.g. gravel, dry or wet asphalt, ice, etc. Also, the assumptions made will remove effects of unmodeled properties.

Another class of models that have gained much attention recently are those that include also transient behavior. The Magic Formula, and other similar models, are approximations of experimental steady-state tire characteristics. Dynamic

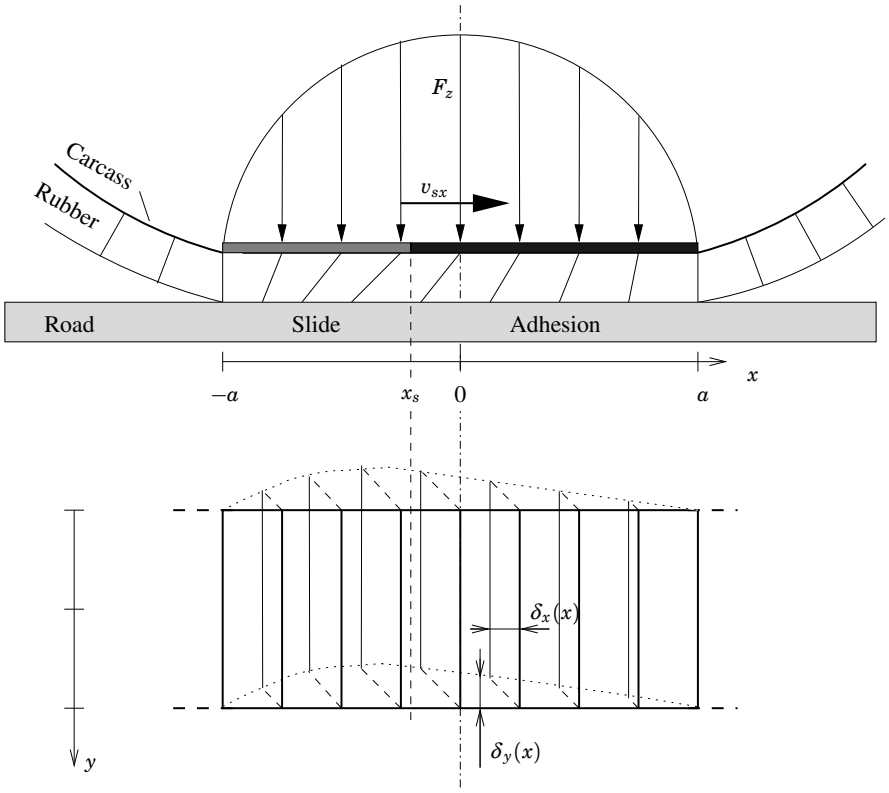

Figure 7 The deformation of the rubber layer between the tire carcass and the road according to the brush model. The carcass moves with the velocity v_{sx} relative the road. The contact zone moves with the vehicle velocity v_x. (Top: side view; Bottom: top view)

transients were investigated in [29] and some recent tire models aim at including dynamic behavior [5, 8, 9]. The main dynamic effect is due to the flexible carcass, which may be modeled by (11).

Much research has been devoted to tire modeling and the brief survey above does by no means cover the area. Further references may be found in e.g. [6] and [24].

2. The Brush Model

The brush-model is a well-known approach to model tire forces, see e.g. [23], [24] or [30]. In this section the brush-model concept is applied to combined slips, much like the approach of [13]. The brush model describes the generation of tire forces based on partitioning of the contact patch into an adhesion and a slide region. Forces in the adhesive region are assumed to be caused by elastic deformation in the rubber volume that is between the tire carcass and the ground. The carcass is assumed to be stiff, which means that effects of carcass deformation are neglected. In the sliding region forces are caused by sliding friction.

The model is obtained by dividing the rubber volume in the contact region into infinitesimal elements. Each element stretches laterally over the entire contact region. The elements are regarded as elastic rectangular blades, or bristles, see Figure 7. Even though rubber in general is not linearly elastic, this assumption is made in the brush model. Positions in the contact region are expressed in a reference system attached to the carcass, with the origin located in the center of the contact region. The length of the contact region is $2a$. Each bristle is assumed to deform independently in the longitudinal and lateral directions. In the adhesive

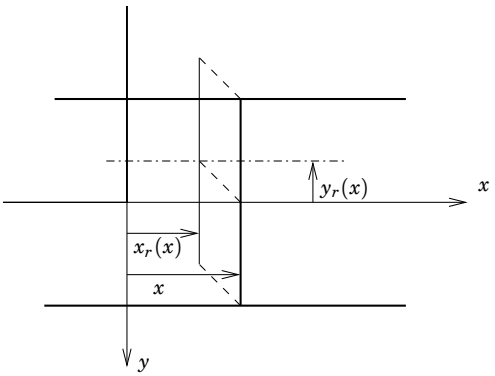

Figure 8 The deformation of a bristle element in the contact patch. Compare with Figure 7.

region the bristles adhere to the road surface and the deformation force is carried by static friction. In the the sliding region the bristles slide on the road surface under influence of sliding friction. Hence, in the sliding region the resulting force is independent of the bristle deformations.

2.1 Combined-Slip Adhesion Forces

Bristle forces Regard the specific infinitesimal bristle which is attached to the carcass at position x relative an origo in the center of the contact patch. Assume that this bristle belongs to the adhesive region. The bristle is in contact with the road surface at position $x_r(x)$, $y_r(x)$, see Figure 8. Since there is no sliding in the adhesive region the contact-point position may be described by

$$x_r(x) = a - \int_0^{t_c(x)} v_x \, dt \tag{22a}$$

$$y_r(x) = -\int_0^{t_c(x)} v_y \, dt \tag{22b}$$

where $t_c(x)$ is the time elapsed since the bristle entered the contact region. The velocities v_c, v_x and v_y are assumed to be constant as a bristle travels through the adhesive region of the contact patch, i.e., during the integration interval $[0, t_c(x)]$. Hence, the bristle position is $x = a - v_c t_c(x)$, and $t_c(x) = (a - x)/v_c$. The deformation of the bristle is

$$\delta_x(x) = x_r(x) - x \tag{23a}$$

$$\delta_y(x) = y_r(x) \tag{23b}$$

Insertion of (22) and the expressions for $t_c(x)$ yields

$$\delta_x(x) = -\frac{v_x - v_c}{v_c}(a - x) = -\sigma_x (a - x) \tag{24a}$$

$$\delta_y(x) = -\frac{v_y}{v_c}(a - x) = -\sigma_y (a - x) \tag{24b}$$

where the slip definition (5a) is used in the last equality. With the assumption of linear elasticity, the deformation force corresponding to (23) is

$$dF_{ax}(x) = c_{px} \, dx \, \delta_x(x) \tag{25a}$$

$$dF_{ay}(x) = c_{py} \, dx \, \delta_y(x) \tag{25b}$$

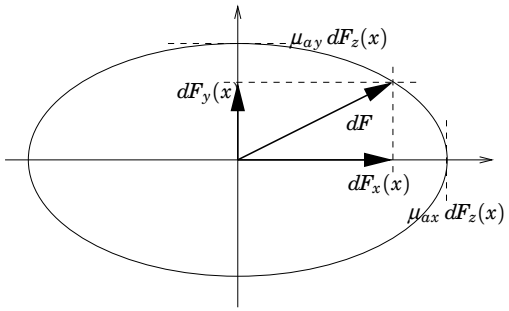

Figure 9 Illustration of the elliptic static friction constraint at anisotropic friction and rubber characteristics. Note that the direction of $d\bar{F}(x)$ and $\bar{\sigma}$ is equal only if $c_{px}/c_{py} = \mu_{ax}/\mu_{ay}$.

where c_{px} and c_{py} are the longitudinal and lateral bristle stiffnesses per unit length. The assumption of constant v_c, v_x, v_y in the interval $[0, t_c(x)]$ is relaxed to the assumption of slow variations in σ_x and σ_y with respect to the duration $2a/v_c$, which is the time for a bristle to travel through the adhesion region. The total adhesive tire force is computed by integration of (25) over the adhesive region. With (24) this gives

$$F_{ax} = \int_{x_s}^{a} dF_{ax}(x) = -c_{px}\sigma_x \int_{x_s}^{a} (a - x)\, dx \tag{26a}$$

$$F_{ay} = \int_{x_s}^{a} dF_{ay}(x) = -c_{py}\sigma_y \int_{x_s}^{a} (a - x)\, dx \tag{26b}$$

where x_s is the position in the contact patch which divides the adhesive and sliding regions. To compute total adhesive force it is necessary to know x_s.

The Size of the Adhesion Region The size of the adhesive region is determined by the available static friction. The deformation will be limited by the largest force that can be carried by the static friction between the tire and the road. The static friction is assumed to be anisotropic with the friction coefficients μ_{ax} and μ_{ay}, respectively. With a normal force $dF_z(x)$ acting on the infinitesimal bristle at position x, the available static friction force is described by the elliptic constraint

$$\left(\frac{dF_{ax}(x)}{dF_z(x)\mu_{ax}}\right)^2 + \left(\frac{dF_{ay}(x)}{dF_z(x)\mu_{ay}}\right)^2 \leq 1 \tag{27}$$

As a result, the magnitude of the available static friction force is dependent of the direction of the deformation force $d\bar{F}_a(x)$, defined by (25). The static friction constraint is illustrated in Figure 9. When $d\bar{F}_a(x)$ exceeds the static friction constraint the bristle will leave the adhesive region and start to slide. Introduce the pressure distribution $q_z(x)$, with $dF_z(x) = q_z(x)\, dx$. By combining (24) and (25) with (27) the static friction constraint may be written as

$$\sqrt{\left(\frac{c_{px}\sigma_x}{\mu_{ax}}\right)^2 + \left(\frac{c_{py}\sigma_y}{\mu_{ay}}\right)^2}\,(a - x) \leq q_z(x) \tag{28}$$

The position x_s in the contact area is the break-away point where the static friction limit is reached and the bristles starts to slide. If the pressure distribution $q_z(x)$ is known then x_s can be calculated by setting equality in (28) with $x = x_s$.

A common assumption is to describe the pressure distribution in the contact patch as a parabolic function:

$$q_z(x) = \frac{3F_z}{4a}\left(1 - \left(\frac{x}{a}\right)^2\right) \tag{29}$$

This is proposed, for example, in [23] and has shown to give a good agreement with experimental longitudinal force-slip curves for real tires. Inserting (29) in (28) with equality gives

$$\sqrt{\left(\frac{c_{px}\sigma_x}{\mu_{ax}}\right)^2+\left(\frac{c_{py}\sigma_y}{\mu_{ay}}\right)^2}(a-x_s)=\frac{3F_z}{4a^3}(a-x_s)(a+x_s) \tag{30}$$

The solution for the break-away point x_s is then

$$x_s(\sigma_x,\sigma_y)=\frac{4a^3}{3F_z}\sqrt{\left(\frac{c_{px}\sigma_x}{\mu_{ax}}\right)^2+\left(\frac{c_{py}\sigma_y}{\mu_{ay}}\right)^2}-a \tag{31}$$

Since x_s is a point in the contact patch it must belong to the interval $[-a,a]$. If $x_s=a$ the entire contact patch is sliding. In the case of pure slip, i.e. either σ_x or σ_y is zero, this will occur at the slips $\sigma_x=\sigma_x^\circ$ or $\sigma_y=\sigma_y^\circ$ with σ_x° and σ_y° given by the following definition.

Definition 1 (Limit slips). Define the limit slips as

$$\sigma_x^\circ \triangleq \frac{3F_z\mu_{ax}}{2a^2c_{px}} \tag{32a}$$

$$\sigma_y^\circ \triangleq \frac{3F_z\mu_{ay}}{2a^2c_{py}} \tag{32b}$$

Introduction of normalized slips with respect to the limit slips will simplify the notation in the following.

Definition 2 (Normalized slip). Define the normalized slip as

$$\psi(\sigma_x,\sigma_y) \triangleq \sqrt{\left(\frac{\sigma_x}{\sigma_x^\circ}\right)^2+\left(\frac{\sigma_x}{\sigma_x^\circ}\right)^2} \tag{33}$$

and the normalized-slip angle as

$$\tan(\beta^\circ) \triangleq \frac{\psi(0,\sigma_y)}{\psi(\sigma_x,0)} \tag{34}$$

Equation (31) may now be rewritten as

$$x_s(\sigma_x,\sigma_y)=(2\psi(\sigma_x,\sigma_y)-1)a \tag{35}$$

It is clear that partial sliding occurs when $\psi(\sigma_x,\sigma_y)<1$. At full sliding then $(\psi(\sigma_x,\sigma_y)\geq 1)$ and $F_{ax}(\sigma_x,\sigma_y)=F_{ay}(\sigma_x,\sigma_y)=0$. In the following the construction of adhesive and sliding forces at partial sliding will be determined.

Total Adhesion Force With the size of the adhesive region, $x_s(\sigma_x,\sigma_y)$, given by (35), the adhesive forces are obtained by solving the integrals (26) yielding:

Property 1 (Adhesion forces). *At partial sliding ($\psi(\sigma_x,\sigma_y)<1$) the adhesive forces are*

$$F_{ax}(\sigma_x,\sigma_y)=-2a^2c_{px}\sigma_x\left(1-\psi(\sigma_x,\sigma_y)\right)^2 \tag{36a}$$

$$F_{ay}(\sigma_x,\sigma_y)=-2a^2c_{py}\sigma_y\left(1-\psi(\sigma_x,\sigma_y)\right)^2 \tag{36b}$$

and at full sliding ($\psi(\sigma_x,\sigma_y)\geq 1$) then $F_{ax}(\sigma_x,\sigma_y)=F_{ay}(\sigma_x,\sigma_y)=0$.

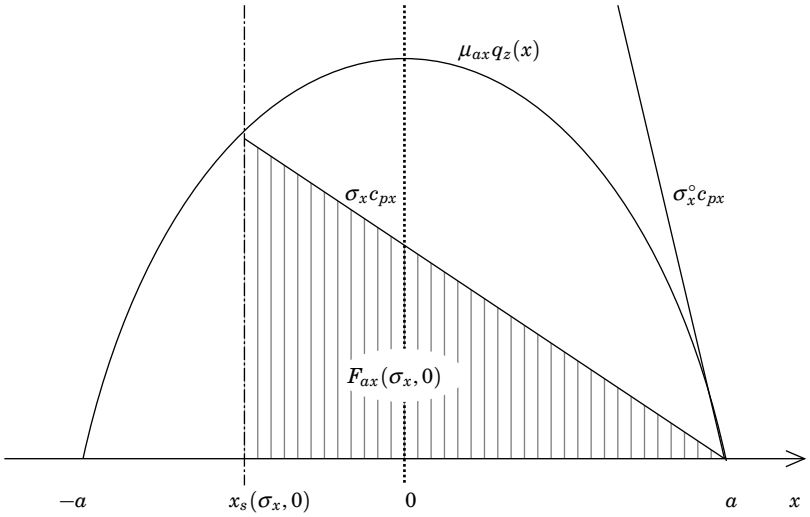

Figure 10 Illustration of the adhesive tire-force for pure longitudinal slip. The elastic deformation force for an element at x in the adhesive region depends linearly on x as $c_{px}\sigma_x(x-a)$, where the slope is proportional to the slip σ_x. The transition from adhesion to slide occurs at the cut of the lines at the break-away point x_s. For slips $\sigma_x > \sigma_x^\circ$ full sliding occur in the contact area since there is then no intersection.

Special notations for the forces at pure slip are introduced as

$$F_{0ax}(\sigma_x) \triangleq F_{ax}(\sigma_x, 0) \tag{37a}$$

$$F_{0ay}(\sigma_y) \triangleq F_{ay}(0, \sigma_y) \tag{37b}$$

Remark 1. Note that it follows from (25) and (24) that the produced adhesive force per unit length in the adhesion region is not affected by combined slips:

$$\frac{dF_{ax}(\sigma_x, x)}{dx} = -c_{px}\sigma_x\,(a - x) \tag{38a}$$

$$\frac{dF_{ay}(\sigma_y, x)}{dx} = -c_{py}\sigma_y\,(a - x) \tag{38b}$$

The adhesive forces thus grow linearly with slopes $c_{px}\sigma_x$ and $c_{py}\sigma_y$ as the contact element moves into the adhesion region.

To illustrate the generation of the adhesive force the case of pure longitudinal slip is regarded, i.e. $\sigma_y = 0$. From (28) the size of the contact region is determined by the point where $c_{px}\sigma_x\,(a - x) = \mu_{ax} q_z(x)$. That is, where the straight line describing the produced force per unit length cuts $\mu_{ax} q_z(x)$, as is shown in Figure 10. The striped area under the line corresponds to the total adhesion force. The slope corresponding to full sliding, i.e. $\sigma_x = \sigma_x^\circ$ is also shown. The case of pure lateral slip is analogous.

2.2 Combined-Slip Slide Forces

The normal force acting on the sliding region at partial sliding may be computed from (29) and (35) as

$$F_{sz}(\sigma_x, \sigma_y) = \int_{-a}^{x_s(\sigma_x, \sigma_y)} q_z(x)\,dx = F_z \psi^2(\sigma_x, \sigma_y)\,(3 - 2\psi(\sigma_x, \sigma_y)) \tag{39}$$

In case of isotopic sliding friction with the friction coefficient μ_s, the friction force is collinear with the slip velocity with the magnitude $F_{sz}(\sigma_x, \sigma_y)\mu_s$ and its

components are given by

$$F_{sx}(\sigma_x, \sigma_y) = -\cos(\beta)\mu_s F_{sz}(\sigma_x, \sigma_y) \tag{40a}$$
$$F_{sy}(\sigma_x, \sigma_y) = -\sin(\beta)\mu_s F_{sz}(\sigma_x, \sigma_y) \tag{40b}$$

where β is defined by (4). Assumptions on isotropic sliding friction are common in tire modeling, see e.g. [28].

If the sliding-friction is anisotropic with the different friction coefficients μ_{sx} and μ_{sy}, there are several ways to calculate the magnitude and the direction of the resulting force. Three different methods are presented in the following and which one to choose depends on the assumptions made on the friction behavior for the actual case.

Collinear Slide Forces This method should be used if the friction between two surfaces is supposed to be isotropic, but the values of μ_{sx} and μ_{sy} are unequal. A reason for that could for example be measurement errors. The friction forces given by

$$F_{sx}(\sigma_x, \sigma_y) = -\cos(\beta^-)\mu_{sx} F_{sx}(\sigma_x, \sigma_y) \tag{41a}$$
$$F_{sy}(\sigma_x, \sigma_y) = -\sin(\beta^-)\mu_{sy} F_{sy}(\sigma_x, \sigma_y) \tag{41b}$$

where β^- is defined as

$$\tan(\beta^-) \triangleq \left(\frac{\mu_{sy}}{\mu_{sx}}\right)^{-1} \frac{v_{sy}}{v_{sx}}. \tag{42}$$

will act in the opposite direction to the sliding motion, with a friction cofficient that is somewhere in the interval $[\mu_{sx}, \mu_{sy}]$ depending on the sliding angle β.

Maximum Dissipation Rate The correct way to treat anisotropic friction according to the literature is to apply the Maximum Dissipation-Rate (MDR) principle. This theory which is further presented in [15] says that the resulting sliding-friction force $\bar{F}_s''$ is the one which maximizes the mechanical work $W = -\bar{v}_s \cdot \bar{F}_s''$ under the constraint

$$\left(\frac{F_{sx}''}{F_{sz}\mu_{sx}}\right)^2 + \left(\frac{F_{sy}''}{F_{sz}\mu_{sy}}\right)^2 \leq 1. \tag{43}$$

This results in the sliding forces

$$F_{sx}''(\sigma_x, \sigma_y) = -\frac{\mu_{sx}^2 v_{sx}}{\sqrt{(\mu_{sx}v_{sx})^2 + (\mu_{sy}v_{sy})^2}} F_{sz}(\sigma_x, \sigma_y) = -\mu_{sx}\cos(\beta')F_{sz} \tag{44a}$$
$$F_{sy}''(\sigma_x, \sigma_y) = -\frac{\mu_{sy}^2 v_{sy}}{\sqrt{(\mu_{sx}v_{sx})^2 + (\mu_{sy}v_{sy})^2}} F_{sz}(\sigma_x, \sigma_y) = -\mu_{sy}\sin(\beta')F_{sz} \tag{44b}$$

where β' is defined as

$$\tan(\beta') \triangleq \frac{\mu_{sy}}{\mu_{sx}} \frac{v_{sy}}{v_{sx}} \tag{45}$$

The angle of the resulting force $\bar{F}_s''$ is denoted by β'' and is given by

$$\tan(\beta'') = \left(\frac{\mu_{sy}}{\mu_{sx}}\right)^2 \frac{v_{sy}}{v_{sx}} \tag{46}$$

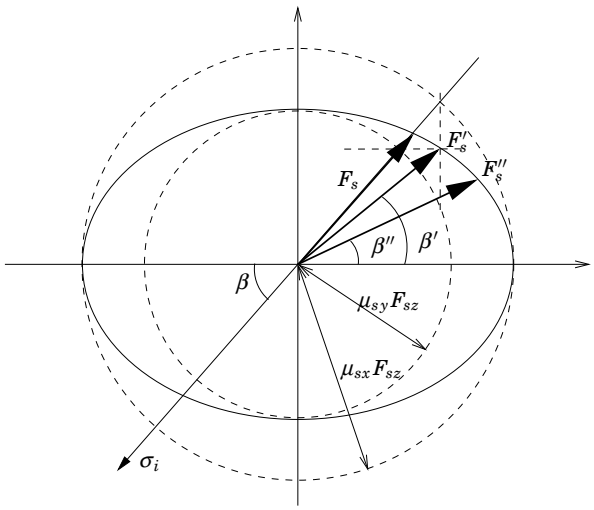

Figure 11 Illustration of methods to describe kinetic friction in case of different longitudial and lateral friction coefficients.

Slip-projection Method An intermediate approach to model anisotropic sliding friction is to simply replace μ_s in (40) with μ_{sx} and μ_{sy} in the corresponding directions:

$$F'_{sx}(\sigma_x, \sigma_y) = -\cos(\beta)\mu_{sx}F_{sz}(\sigma_x, \sigma_y) \tag{47a}$$
$$F'_{sy}(\sigma_x, \sigma_y) = -\sin(\beta)\mu_{sy}F_{sz}(\sigma_x, \sigma_y) \tag{47b}$$

This means a projection of the pure-slip sliding-forces on the slip vector. The angle of the resulting force is then equal to β'. From the definitions of β (4), β' (45) and β'' (46), it is clear that the direction of $\bar{F}'_s$ will lie between the directions of $\bar{F}_s$ and $\bar{F}''_s$, see Figure 11. In the following $\bar{F}_s$ will denote the sliding force of (48).

To summarize:

Property 2 (Slide forces). *The sliding forces are described by*

$$F_{sx}(\sigma_x, \sigma_y) = -\cos(\beta_{\mathrm{f}})\mu_{sx}F_{sz}(\sigma_x, \sigma_y) \tag{48a}$$
$$F_{sy}(\sigma_x, \sigma_y) = -\sin(\beta_{\mathrm{f}})\mu_{sy}F_{sz}(\sigma_x, \sigma_y) \tag{48b}$$

with

$$F_{sz}(\sigma_x, \sigma_y) = F_z\psi^2(\sigma_x, \sigma_y)\,(3 - 2\psi(\sigma_x, \sigma_y)) \tag{49}$$

and β_{f} is any of β^- (collinear), β (slip-projection) or β' (MDR) depending on choice of friction model:

$$\tan(\beta^-) \triangleq (\frac{\mu_{sy}}{\mu_{sx}})^{-1}\frac{v_{sy}}{v_{sx}} \quad \tan(\beta) \triangleq (\frac{v_{sy}}{v_{sx}}) \quad \tan(\beta') \triangleq (\frac{\mu_{sy}}{\mu_{sx}})\frac{v_{sy}}{v_{sx}} \tag{50}$$

Remark 2. In the special case of pure-slip the sliding-forces are

$$F_{0sx}(\sigma_x) = -\mu_{sx}F_{sz}(\sigma_x, 0)\,\mathrm{sgn}(\sigma_x) \tag{51a}$$
$$F_{0sy}(\sigma_y) = -\mu_{sy}F_{sz}(0, \sigma_y)\,\mathrm{sgn}(\sigma_y) \tag{51b}$$

In Figure 12 the case of pure longitudinal slip is again regarded, now with also the sliding force introduced. Since $q_z(x)$ is the normal force per unit length, the sliding force per unit length is simply $\mu_{sx}q_z(x)$, as marked in the figure. The horizontally striped area corresponds to the total sliding force.

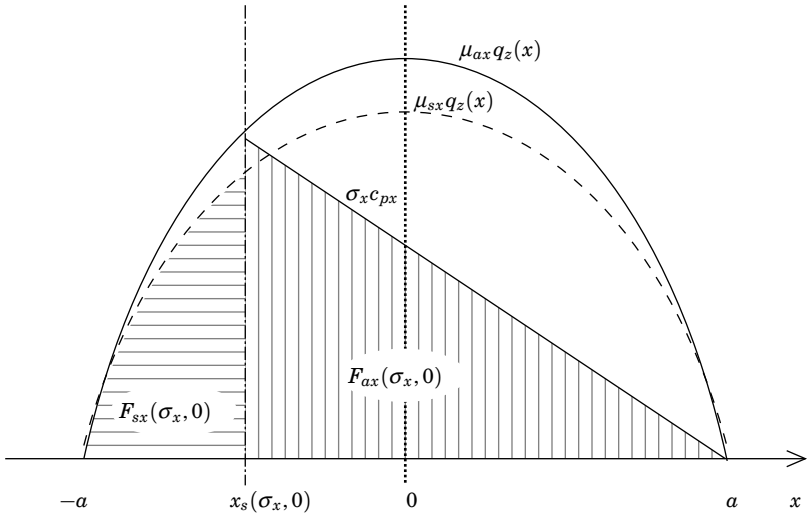

Figure 12 Illustration of partition of the contact area into a sliding and an adhesive region for the case of pure longitudinal slip. The slide force for an element at x is determined by the pressure distribution $\mu_{sx} q_z(x)\, dx$. The horizontally striped area is the total slide force.

2.3 Effects of Combined Slips

The total tire force is given by adding the adhesive forces of (36) and the sliding forces of (48):

$$F_x(\sigma_x, \sigma_y) = F_{ax}(\sigma_x, \sigma_y) + F_{sx}(\sigma_x, \sigma_y) \tag{52a}$$

$$F_y(\sigma_x, \sigma_y) = F_{ay}(\sigma_x, \sigma_y) + F_{sy}(\sigma_x, \sigma_y) \tag{52b}$$

To illustrate the effect of combined slips Figure 13 shows the production of longitudinal force in the case of combined longitudinal and lateral slip (σ_x, σ_y) with $\sigma_x \neq 0$, $\sigma_y \neq 0$. From (35) it is clear that the adhering region shrinks compared to the case with pure slip $(\sigma_x, 0)$. The sliding region grows accordingly. From (38) it is clear that the adhesive force per unit length is the same for the combined slip (σ_x, σ_y) as for the pure-slip $(\sigma_x, 0)$. Hence, the slope is the same, but the area corresponding to the force is smaller since the adhering region is smaller. The corresponding adhesive-force slope derived from (38) is $c_{px} \sigma_x^{\circ} \psi(\sigma_x, \sigma_y)$. The corresponding expression applies for the lateral force. It is therefore clear that sliding will occur simultaneously in both directions as $\psi(\sigma_x, \sigma_y)$ approaches unity. It is important to note that the indicated area under the pressure distribution no longer corresponds to the resulting sliding force. Instead it describes $\mu_{sx} F_{sz}(\sigma_x, \sigma_y)$, which is the force that would result for pure longitudinal sliding with the sliding region $x_s(\sigma_x, \sigma_y)$. This force must be limited by a friction constraint according to Section 2.2.

The braking and cornering stiffnesses are the linearizations of the pure-slip friction curves at small slips and may be computed by derivation of (52):

$$C_x = -\left.\frac{\partial F_x(\sigma_x, 0)}{\partial \sigma_x}\right|_{\sigma_x = 0} = 2 c_{px} a^2 \tag{53a}$$

$$C_y = -\left.\frac{\partial F_y(0, \sigma_y)}{\partial \sigma_y}\right|_{\sigma_y = 0} = 2 c_{py} a^2 \tag{53b}$$

Note that the stiffnesses C_λ and C_α defined in Section 1.6 are described in λ and α. Therefore $C_x = C_\lambda$ while $C_y = C_\alpha \cdot \pi/180$ since α is normally expressed in

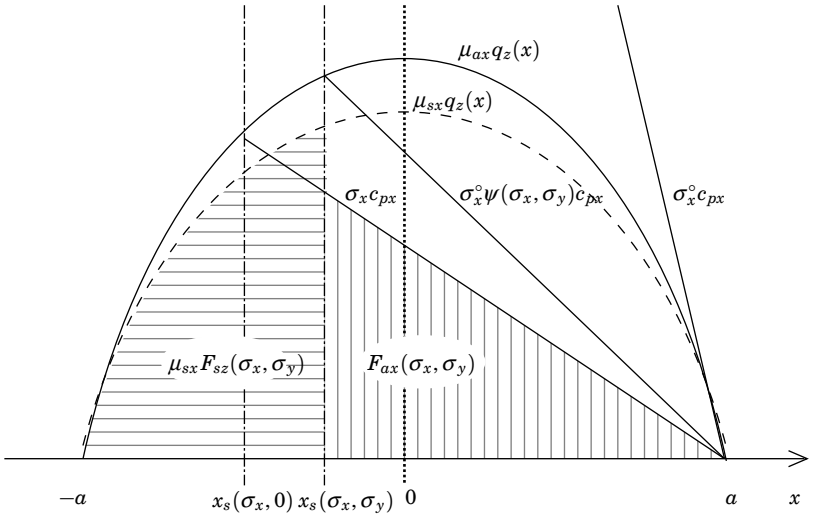

Figure 13 Illustration of the effect of combined slip. The combined-slip has the effect of decreasing the size of the adhesive region, compare with Figure 12.

degrees. The effect of combined slips on the stiffnesses are likewise computed as

$$\left.\frac{\partial F_x(\sigma_x, \sigma_y)}{\partial \sigma_x}\right|_{\sigma_x = 0} = \begin{cases} -2c_{px}a^2(1-\psi(0,\sigma_y))^2 - \mu_{sx}F_z(3-2\psi(0,\sigma_y))\dfrac{\psi(0,\sigma_y)}{\sigma_y^\circ} & \text{if } \psi(0,\sigma_y) \le 1 \\ \dfrac{\mu_{sx}F_z}{\sigma_y} & \text{otherwise} \end{cases} \tag{54}$$

$$\left.\frac{\partial F_y(\sigma_x, \sigma_y)}{\partial \sigma_y}\right|_{\sigma_y = 0} = \begin{cases} -2c_{py}a^2(1-\psi(\sigma_x,0))^2 - \mu_{sy}F_z(3-2\psi(\sigma_x,0))\dfrac{\psi(\sigma_x,0)}{\sigma_x^\circ} & \text{if } \psi(\sigma_x,0) \le 1 \\ \dfrac{\mu_{sy}F_z}{\sigma_x} & \text{otherwise} \end{cases} \tag{55}$$

Note that these expressions are valid when the sliding friction is described by the slip-projection method (47).

2.4 Self-Aligning Torque

The self-aligning torque consists of two parts. The main part is M_z', which is the torque developed by the non-symmetric distribution of the lateral force F_y. An additional part M_z'' comes up because of the deformation of the tire.

The torque dM_z' developed at position x in the contact region is

$$dM_z'(x) = dF_y(x)\, x \tag{56}$$

In the adhesive part of the contact region the expression for $dF_y(x)$ is given by (25) together with (24). In the sliding zone it is instead given by differentiating (48)

using $dF_z(x) = q(x)\,dx$. Integration over the adhesive and sliding area separately gives

$$M'_{az}(\sigma_x,\sigma_y) = -c_{py}\sigma_y \int_{x_s(\sigma_x,\sigma_y)}^{a} x\,(a-x)\,dx$$
$$= -c_{py}a^3\sigma_y\frac{2}{3}(1-\psi(\sigma_x,\sigma_y))^2(4\psi(\sigma_x,\sigma_y)-1) \quad (57)$$

$$M'_{sz}(\sigma_x,\sigma_y) = -\mu_{sy}\sin(\beta)\int_{-a}^{x_s(\sigma_x,\sigma_y)} x\,q_z(x)\,dx$$
$$= -3\mu_{sx}\sin(\beta)aF_z\psi^2(\sigma_x,\sigma_y)(1-\psi(\sigma_x,\sigma_y))^2 \quad (58)$$

$$M'_z(\sigma_x,\sigma_y) = M'_{az}(\sigma_x,\sigma_y) + M'_{sz}(\sigma_x,\sigma_y) \quad (59)$$

When there is a lateral slip the tire deflects laterally and the point of action for the longitudinal force will have an offset from the central plane of the wheel. This produces an additional deformation torque in the z-direction. A longitudinal deflection together with a lateral force has the same effect. Since it is assumed that the carcass is stiff the deformation is here described by bristle deflections. The deformation torque developed at position x in the contact region is then described by

$$dM''_z(x) = dF_y(x)\delta_x(x) - dF_x(x)\delta_y(x) \quad (60)$$

In the same way as above, integration over the adhesive and the sliding regions is performed separately. The deformation $\delta_x(x)$ is computed from (24) in the adhesive region and from (25) using the infinitesimal sliding force in the sliding region. Hence

$$M''_{az}(\sigma_x,\sigma_y) = \int_{x_s(\sigma_x,\sigma_y)}^{a} c_{py}\sigma_y(a-x)\sigma_x(a-x)\,dx - \int_{x_s(\sigma_x,\sigma_y)}^{a} c_{px}\sigma_x(a-x)\sigma_y(a-x)\,dx$$
$$= \frac{4}{3}(C_y-C_x)a\sigma_x\sigma_y(1-\psi(\sigma_x,\sigma_y))^3$$
$$= \frac{4}{3}\left(\frac{1}{C_x}-\frac{1}{C_y}\right)\frac{a}{(1-\psi(\sigma_x,\sigma_y))}F_{ax}(\sigma_x,\sigma_y)F_{ay}(\sigma_x,\sigma_y) \quad (61)$$

$$M''_{sz}(\sigma_x,\sigma_y) = \int_{-a}^{x_s(\sigma_x,\sigma_y)} \mu_{sy}\sin(\beta_f)q_z(x)\mu_{sx}^2\cos(\beta_f)\frac{1}{c_{px}}q_z(x)\,dx$$
$$- \int_{-a}^{x_s(\sigma_x,\sigma_y)} \mu_{sx}\cos(\beta_f)q_z(x)\mu_{sy}\sin(\beta_f)\frac{1}{c_{py}}q_z(x)\,dx$$
$$= \frac{6}{5}\left(\frac{1}{C_x}-\frac{1}{C_y}\right)\mu_{sx}\mu_{sy}a\sin(\beta_f)\cos(\beta_f)F_z^2$$
$$\cdot\,\psi^3(\sigma_x,\sigma_y)(10-15\psi(\sigma_x,\sigma_y)+6\psi^2(\sigma_x,\sigma_y))$$
$$= \frac{6}{5}\left(\frac{1}{C_x}-\frac{1}{C_y}\right)\frac{a(10-15\psi(\sigma_x,\sigma_y)+6\psi^2(\sigma_x,\sigma_y))}{\psi(\sigma_x,\sigma_y)(3-2\psi(\sigma_x,\sigma_y))^2}$$
$$\cdot\,F_{sx}(\sigma_x,\sigma_y)F_{sy}(\sigma_x,\sigma_y) \quad (62)$$

where (36) and (48) have been used in the last step.

$$M''_z(\sigma_x,\sigma_y) = M''_{az}(\sigma_x,\sigma_y) + M''_{sz}(\sigma_x,\sigma_y) \quad (63)$$

Finally,

$$M_z(\sigma_x,\sigma_y) = M'_z(\sigma_x,\sigma_y) + M''_z(\sigma_x,\sigma_y) \quad (64)$$

A commonly used parameter is the pneumatic trail, which denotes the distance between the center of the tire and point of action for the lateral force. It is defined as $t(\sigma_x, \sigma_y) = M_z(\sigma_x, \sigma_y)/F_y(\sigma_x, \sigma_y)$. The coordinate for the point of action for the adhesive force is denoted by $t_a(\sigma_x, \sigma_y)$ and for the sliding force by $t_s(\sigma_x, \sigma_y)$. By using (57) and (36) respective (58) and (48) the contributions from $M_z'(\sigma_x, \sigma_y)$ to the pneumatic trail, $t_a'(\sigma_x, \sigma_y)$ and $t_s'(\sigma_x, \sigma_y)$, are given by

$$t_a'(\sigma_x, \sigma_y) = \frac{M_{az}'(\sigma_x, \sigma_y)}{F_{ay}(\sigma_x, \sigma_y)} = \frac{a}{3}(4\psi(\sigma_x, \sigma_y) - 1) \tag{65a}$$

$$t_s'(\sigma_x, \sigma_y) = \frac{M_{sz}'(\sigma_x, \sigma_y)}{F_{sy}(\sigma_x, \sigma_y)} = -3a\frac{(1 - \psi(\sigma_x, \sigma_y))^2}{(3 - 2\psi(\sigma_x, \sigma_y))} \tag{65b}$$

The contributions from $M_z''(\sigma_x, \sigma_y)$ can be read directly from (61) and (62).

In the same way as for the braking and cornering stiffness, the aligning stiffness is defined as

$$C_z = -\left.\frac{\partial M_z}{\partial \sigma_y}\right|_{\sigma_x, \sigma_y = 0} = c_{py}a^3\frac{2}{3} = C_y\frac{a}{3} \tag{66}$$

2.5 Analysis of the Brush-Model

In Figures 14 and 15 the brush model is compared with the Magic Formula fitted to a truck tire. For the brush model also combined-slip behavior is shown. The parameters are choosen so that the pure-slip curves have the same braking and cornering stiffnesses and the same peak force as of the Magic Formula. For the pure longitudinal slip the coherence between the brush model and the reference curve is good. For the pure lateral slip there are descrepancies in the lateral force and the self-aligning torque. The main reason for this is the assumption of a stiff carcass. This is realistic in the longitudinal direction, but for the lateral case where the carcass is weaker the effects of this simplification is noticable. There exists more accurate models which include carcass flexibility based on assumptions on stretched string or beam behavior [23]. These, however, result in quite complicated expressions.

A deficiency with the brush model is the assumption on velocity-independent sliding friction resulting in constant tire-forces at full sliding, which is obviously not correct as seen in e.g. Figure 14. At partial sliding the approximation normally has small effects.

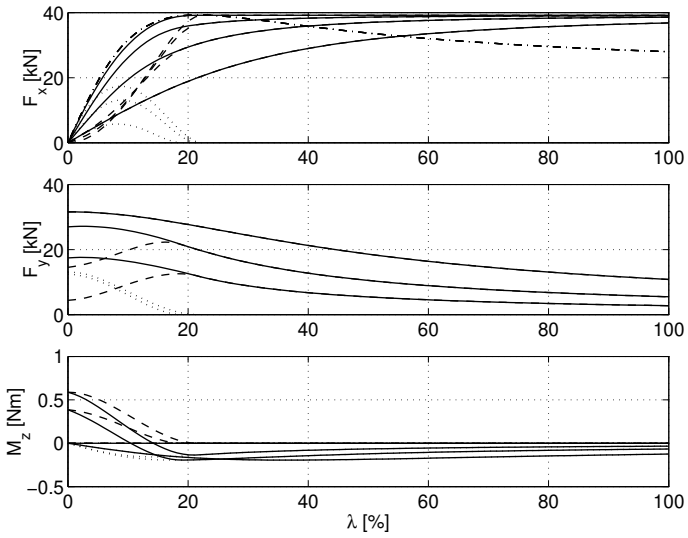

Figure 14 Tire forces as function of λ with $\alpha = [0, 5, 10, 20]$ deg. The dotted line shows the force from the adhesive region, the dashed line shows it from the sliding region. The solid line is the total force and the dashed dotted line is the reference curve created from the magic formula. For the self aligning torque the dotted line denotes the deformation torque M_z'' and the dashed line M'.

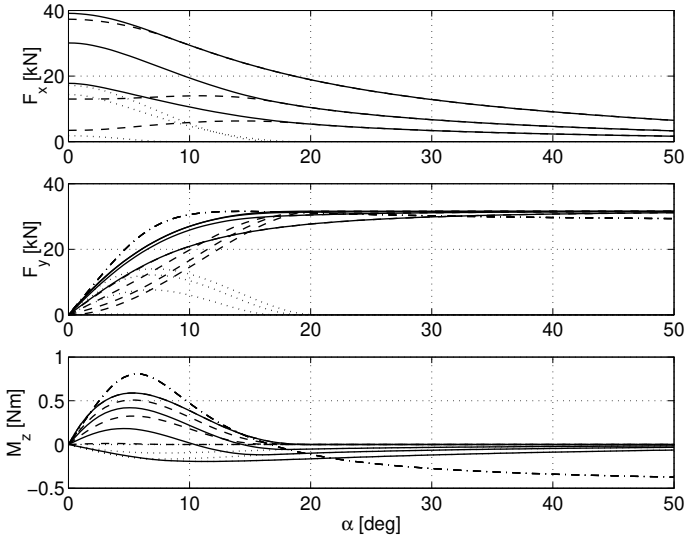

Figure 15 Tire forces as function of α with $\lambda = [0, 5, 10, 20]$ deg. The dotted line shows the force from the adhesive region, the dashed line shows it from the sliding region. The solid line is the total force and the dashed dotted line is the reference curve created from the magic formula. For the self aligning torque the dotted line denotes the deformation torque M_z'' and the dashed line M'.

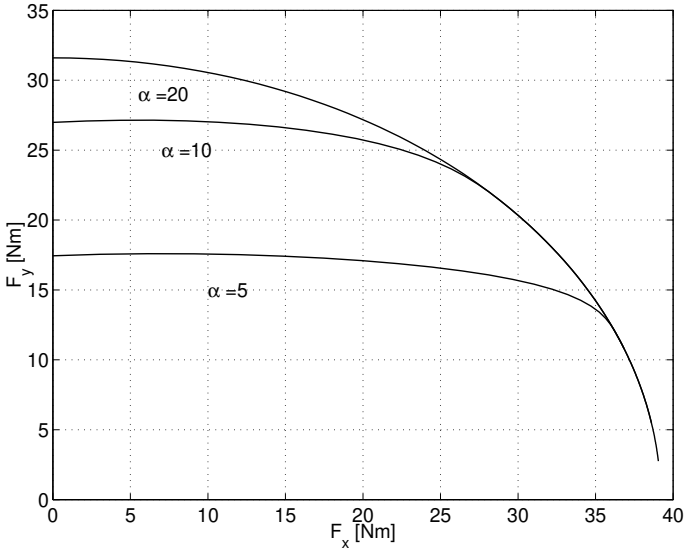

Figure 16 Plot of the lateral force as a function of the longitudinal force. The curves are derived with the brush model for $\lambda \in [0, 1]\%$ and $\alpha = 5$, 10 and 20 deg.

3. Brush-Model Relations Between Pure- and Combined-Slip Conditions

In this section a number of properties are stated which describe relations between pure-slip and combined-slip forces for the brush model. In Section 4 they are combined with empirical data to form semi-empirical tire-force models for combined slips. The basic idea is to treat sliding and adhesive forces separately. Since empirical pure-slip data normally only regard total tire-forces it is therefore necessary to have a procedure to separate the sliding and adhesive forces.

3.1 Separation of Adhesion and Slide Forces

Definition 3 (Pure-slip adhesive and sliding fractions). Define $\theta_x(\sigma_x)$ and $\theta_y(\sigma_y)$ as the relative amount of the tire force that is generated by sliding friction at partial sliding ($\psi(\sigma_x, 0) < 1$ and $\psi(0, \sigma_y) < 1$)

$$\theta_x(\sigma_x) \triangleq \frac{F_{0sx}(\sigma_x)}{F_{0ax}(\sigma_x) + F_{0sx}(\sigma_x)} \tag{67a}$$

$$\theta_y(\sigma_y) \triangleq \frac{F_{0sy}(\sigma_y)}{F_{0ay}(\sigma_y) + F_{0sy}(\sigma_y)} \tag{67b}$$

Then the sliding components of $F_{0x}(\sigma_x)$ and $F_{0y}(\sigma_y)$ at partial sliding are

$$F_{0sx}(\sigma_x) = \theta_x(\sigma_x) F_{0x}(\sigma_x) \tag{68a}$$

$$F_{0sy}(\sigma_y) = \theta_y(\sigma_y) F_{0y}(\sigma_y) \tag{68b}$$

and the adhesive components are

$$F_{0ax}(\sigma_x) = (1 - \theta_x(\sigma_x))\, F_{0x}(\sigma_x) \tag{69a}$$

$$F_{0ay}(\sigma_y) = (1 - \theta_y(\sigma_y))\, F_{0y}(\sigma_y) \tag{69b}$$

For the brush-model the following property then holds:

Property 3 (Pure-slip adhesive and sliding fractions). *At pure-slip partial sliding ($\psi(\sigma_x, 0) < 1$ or $\psi(0, \sigma_y) < 1$) then*

$$\theta_x(\sigma_x) = \frac{\psi(\sigma_x, 0)\,(3 - 2\psi(\sigma_x, 0))}{3\rho_x\,(1 - \psi(\sigma_x, 0))^2 + \psi(\sigma_x, 0)\,(3 - 2\psi(\sigma_x, 0))} \tag{70a}$$

$$\theta_y(\sigma_y) = \frac{\psi(0, \sigma_y)\,(3 - 2\psi(0, \sigma_y))}{3\rho_y(\sigma_y)\,(1 - \psi(0, \sigma_y))^2 + \psi(0, \sigma_y)\,(3 - 2\psi(0, \sigma_y))} \tag{70b}$$

and

$$1 - \theta_x(\sigma_x) = \frac{3\rho_x\,(1 - \psi(\sigma_x, 0))^2}{3\rho_x\,(1 - \psi(\sigma_x, 0))^2 + \psi(\sigma_x, 0)\,(3 - 2\psi(\sigma_x, 0))} \tag{71a}$$

$$1 - \theta_y(\sigma_y) = \frac{3\rho_y\,(1 - \psi(0, \sigma_y))^2}{3\rho_y\,(1 - \psi(0, \sigma_y))^2 + \psi(0, \sigma_y)\,(3 - 2\psi(0, \sigma_y))} \tag{71b}$$

where the parameters $\rho_x \triangleq \mu_{ax}/\mu_{sx} > 0$ and $\rho_y \triangleq \mu_{ay}/\mu_{sy} > 0$ describe the ratio between the adheseive and sliding-friction coefficients. At full sliding ($\psi(\sigma_x, 0) \geq 1$ or $\psi(0, \sigma_y) \geq 1$) then $\theta_x(\sigma_x) = 1$ or $\theta_y(\sigma_y) = 1$ since then $F_{0ax}(\sigma_x) = F_{0ay}(\sigma_y) = 0$.

Proof. See Appendix A.1. □

Remark 3. Note that (70) and (71) are non-singular for all $0 \leq \psi_x \leq 1$ and $0 \leq \psi_y \leq 1$, since the polynomial $p(x) = 3\rho(1 - x)^2 + x(3 - 2x)$ not has any real roots in the interval $[0, 1]$ for $\rho > 0$.

3.2 Combined-Slip Forces as a Scaling of Pure-Slip Forces

With expressions for the adhesion and slide forces the combined forces may be written as

$$F_{ax}(\sigma_x, \sigma_y) = F_{0ax}(\sigma_{0x}) \frac{F_{ax}(\sigma_x, \sigma_y)}{F_{0ax}(\sigma_{0x})} \tag{72a}$$

$$F_{ay}(\sigma_x, \sigma_y) = F_{0ay}(\sigma_{0y}) \frac{F_{ay}(\sigma_x, \sigma_y)}{F_{0ay}(\sigma_{0y})} \tag{72b}$$

and

$$F_{sx}(\sigma_x, \sigma_y) = F_{0sx}(\sigma_{0x}) \frac{F_{sx}(\sigma_x, \sigma_y)}{F_{0sx}(\sigma_{0x})} \tag{72c}$$

$$F_{sy}(\sigma_x, \sigma_y) = F_{0sy}(\sigma_{0y}) \frac{F_{sy}(\sigma_x, \sigma_y)}{F_{0sy}(\sigma_{0y})} \tag{72d}$$

The last factors in these expressions may be regarded as scaling factors relating forces at the combined slip σ_x and σ_y with forces at arbitrarily chosen pure slips σ_{0x}, and σ_{0y}. On the basis of the brush model the factors may be expressed as functions of σ_x, σ_y, σ_{0x}, and σ_{0y}. Four different choices of σ_{0x} and σ_{0y} are regarded in the following, each having different interpretations and emphasizing on different properties:

- The *deformation invariant pure-slips* $\sigma_{0x} = \sigma_{0x}^{\text{def}}$ and $\sigma_{0y} = \sigma_{y}^{\text{def}}$ preserve the combined-slip bristle-deformation.
- The *region invariant pure-slips* $\sigma_{0x} = \sigma_{0x}^{\text{reg}}$ and $\sigma_{0y} = \sigma_{0y}^{\text{reg}}$ preserve the sizes of the combined-slip adhesive and sliding regions.
- The *slip-velocity invariant pure-slips* $\sigma_{0x} = \sigma_{x}^{\text{vel}}$ and $\sigma_{0y} = \sigma_{y}^{\text{vel}}$ preserve the magnitude of the slip-velocity of the combined-slip.
- The *slip-velocity component invariant pure-slips* $\sigma_{0x} = \sigma_{x}^{\text{velc}}$ and $\sigma_{0y} = \sigma_{y}^{\text{velc}}$ preserve the respective components of the slip-velocity of the combined-slip.

Property 4 (Deformation invariant pure-slips). *The deformation invariant pure-slips* σ_{0x}^{def} *and* σ_{0y}^{def} *simply are*

$$\sigma_{0x}^{\text{def}} \triangleq \sigma_x \tag{73a}$$

$$\sigma_{0y}^{\text{def}} \triangleq \sigma_y \tag{73b}$$

and the pure-slips $(\sigma_{0x}^{\text{def}}, 0)$ *and* $(0, \sigma_{0y}^{\text{def}})$ *result in the same bristle deformation as the combined slip* (σ_x, σ_y).

Proof. See Appendix A.2. □

Property 5 (Deformation invariant adhesion-forces). *The combined-slip adhesion forces at partial sliding* ($\psi(\sigma_x, \sigma_y) < 1$) *are related to the deformation-invariant pure-slip adhesion forces as*

$$F_{ax}(\sigma_x, \sigma_y) = \frac{3\rho_x \left(1 - \psi(\sigma_x, \sigma_y)\right)^2}{3\rho_x \left(1 - \psi(\sigma_x, 0)\right)^2 + \psi(\sigma_x, 0)\left(3 - 2\psi(\sigma_x, 0)\right)} F_{0x}(\sigma_x) \tag{74a}$$

$$F_{ay}(\sigma_y, \sigma_y) = \frac{3\rho_y \left(1 - \psi(\sigma_x, \sigma_y)\right)^2}{3\rho_y \left(1 - \psi(0, \sigma_y)\right)^2 + \psi(0, \sigma_y)\left(3 - 2\psi(0, \sigma_y)\right)} F_{0y}(\sigma_y) \tag{74b}$$

Proof. See Appendix A.3. □

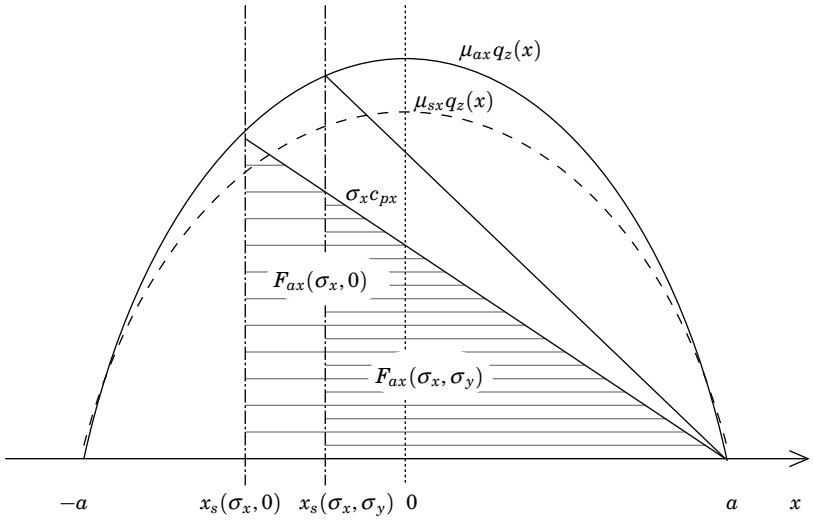

Figure 17 Deformation-invariant scaling of the adhesion force. The line with the slope $\sigma_x c_{px}$ describes $dF_a(x)$ and the indicated areas the pure-slip (sparsely striped) and combined-slip (densely striped) total adhesion forces. The break-away point for the deformation-invariant pure-slip lies where $dF_a(x)$ cuts $\mu_{ax}q_z(x)$.

Remark 4. The produced adhesion force per unit length in the contact region is equal for pure and combined slips. The difference in total adhesion force is due to the decreasing contact region for combined slips. This is illustrated in Figure 17, where it can be seen that Property 5 reflects a scaling of the pure-slip adhesion force (sparsely striped area) to agree with the combined-slip adhesion force (densely striped area).

Property 6 (Deformation invariant slide-forces). *The combined-slip slide forces are related to the deformation-invariant pure-slip slide forces as*

$$F_{sx}(\sigma_x, \sigma_y) = F_{0x}(\sigma_x) \cdot \Gamma_x \tag{75a}$$
$$F_{sy}(\sigma_x, \sigma_y) = F_{0y}(\sigma_y) \cdot \Gamma_y \tag{75b}$$

with

$$\Gamma_x \triangleq \begin{cases} \dfrac{\psi(\sigma_x,\sigma_y)\,(3-2\psi(\sigma_x,\sigma_y))}{3\rho_x\,(1-\psi(\sigma_x,0))^2+\psi(\sigma_x,0)\,(3-2\psi(\sigma_x,0))} \\ \qquad \cdot\sigma_x^\circ\left(\dfrac{1}{\sigma_x^\circ}|\cos(\beta)|\cos(\beta^\circ)+\dfrac{1}{\sigma_y^\circ}|\sin(\beta)|\sin(\beta^\circ)\right), & \text{if } \psi(\sigma_x,\sigma_y)<1 \\ \dfrac{1}{3\rho_x\,(1-\psi(\sigma_x,0))^2+\psi(\sigma_x,0)\,(3-2\psi(\sigma_x,0))}\dfrac{\sigma_x^\circ}{\sqrt{\sigma_x^2+\sigma_y^2}}, \\ \qquad\qquad \text{if } \psi(\sigma_x,\sigma_y)\geq 1 \text{ and } \psi(\sigma_x,0)<1 \\ \cos(\beta), \qquad\qquad \text{if } \psi(\sigma_x,\sigma_y)\geq 1 \text{ and } \psi(\sigma_x,0)\geq 1 \end{cases} \tag{76a}$$

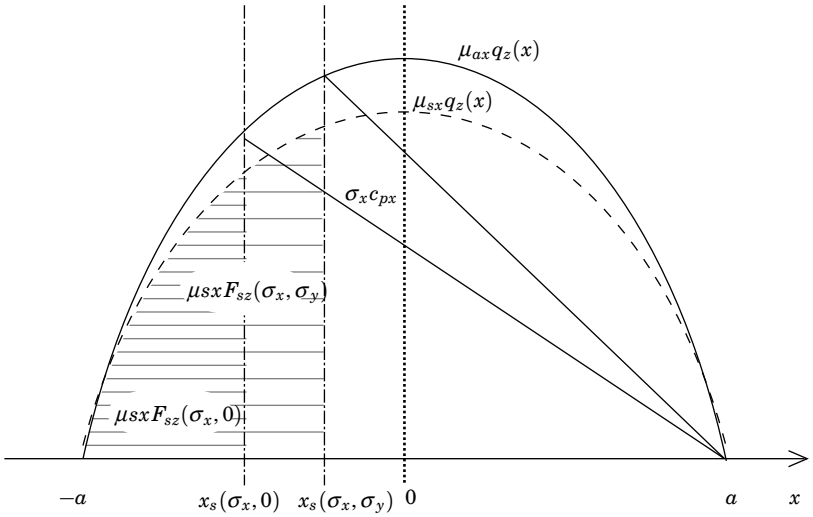

Figure 18 Deformation-invariant scaling of the slide force. The line with the slope $\sigma_x c_{px}$ describes $dF_a(x)$. The break-away point for the deformation-invariant pure-slip lies where $dF_a(x)$ cuts $\mu_{ax}q_z(x)$. The indicated areas show the pure-slip (sparsely striped) and combined-slip (densely striped) total slide forces, since $dF_{sx}(x) = \mu_{sx}q_z(x)\,dx$. Note that $F_{sx}(\sigma_x, \sigma_y)$ is obtained by multiplying $\mu_{sx}F_{sz}(\sigma_x, \sigma_y)$ by $cos(\beta)$.

and

$$\Gamma_y \triangleq \begin{cases} \dfrac{\psi(\sigma_x,\sigma_y)\,(3-2\psi(\sigma_x,\sigma_y))}{3\rho_y\,(1-\psi(0,\sigma_y))^2+\psi(0,\sigma_y)\,(3-2\psi(0,\sigma_y))} & \\ \quad \cdot\sigma_y^\circ\left(\dfrac{1}{\sigma_x^\circ}|\cos(\beta)|\cos(\beta^\circ)+\dfrac{1}{\sigma_y^\circ}|\sin(\beta)|\sin(\beta^\circ)\right), & \text{if } \psi(\sigma_x,\sigma_y)<1 \\ \dfrac{1}{3\rho_y\,(1-\psi(0,\sigma_y))^2+\psi(0,\sigma_y)\,(3-2\psi(0,\sigma_y))}\,\dfrac{\sigma_y^\circ}{\sqrt{\sigma_x^2+\sigma_y^2}}, & \\ \qquad\qquad \text{if } \psi(\sigma_x,\sigma_y)\geq 1 \text{ and } \psi(0,\sigma_y)<1 & \\ \cos(\beta), \qquad \text{if } \psi(\sigma_x,\sigma_y)\geq 1 \text{ and } \psi(0,\sigma_y)\geq 1 & \end{cases} \tag{76b}$$

Proof. See Appendix A.4. □

Remark 5. In Figure 18 it can be seen that Property 6 reflects a scaling of the pure-slip slide-force (sparsely striped area) to agree with the combined-slip slide-force (densely striped area). The deformation invariant scaling is restricted to slip-projection sliding friction.

Property 7 (Region invariant pure-slips). *Define the region invariant slips* σ_{0x}^{reg} *and* σ_{0y}^{reg} *as*

$$\sigma_{0x}^{\text{reg}} \triangleq \sigma_x^\circ \psi(\sigma_x,\sigma_y)\,\text{sgn}(\sigma_x) \tag{77a}$$

$$\sigma_{0y}^{\text{reg}} \triangleq \sigma_y^\circ \psi(\sigma_x,\sigma_y)\,\text{sgn}(\sigma_y) \tag{77b}$$

The pure-slips $(\sigma_{0x}^{\text{reg}}, 0)$ *and* $(0, \sigma_{0y}^{\text{reg}})$ *then results in an adhesive and sliding regions of the size size as the combined slip* (σ_x, σ_y)*.*

Proof. See Appendix A.5. □

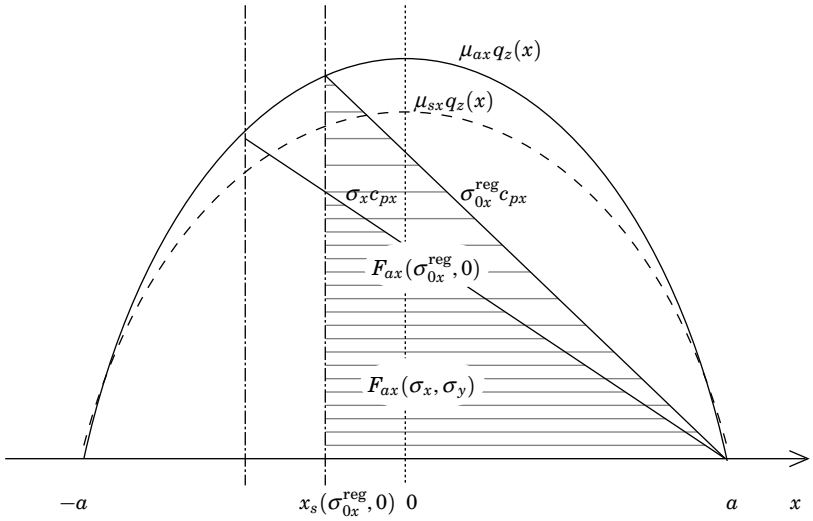

Figure 19 Region-invariant scaling of the adhesion force. The line with the slope $\sigma_{0x}^{\mathrm{reg}} c_{px}$ describes $dF_{0a}(x)$ for the region-invariant pure-slip and the indicated areas the pure-slip (sparsely striped) and combined-slip (densely striped) total adhesion forces. Note that the break-away point is identical for the combined slip and the region-invariant pure-slip $x_s(\sigma_x, \sigma_y) = x_s(\sigma_{0x}^{\mathrm{reg}}, 0)$.

Property 8 (Region invariant adhesion-forces). *The combined-slip adhesion forces at partial sliding ($\psi(\sigma_x, \sigma_y) < 1$) are related to the region invariant pure-slip adhesion forces as*

$$F_{ax}(\sigma_x, \sigma_y) = (1 - \theta_x(\sigma_{0x}^{\mathrm{reg}})) F_{0x}(\sigma_{0x}^{\mathrm{reg}}) \cos(\beta^\circ) \tag{78a}$$
$$F_{ay}(\sigma_y, \sigma_y) = (1 - \theta_y(\sigma_{0y}^{\mathrm{reg}})) F_{0y}(\sigma_{0y}^{\mathrm{reg}}) \sin(\beta^\circ) \tag{78b}$$

with β° given by (34).

Proof. See Appendix A.6. □

Remark 6. The region invariant pure-slip result in an adhesive region of the same size as the combined slip, as illustrated in Figure 19. However, the produced adhesive force per unit length is larger. Property 8 thus reflects a scaling of the region-invariant pure-slip adhesion force (sparsely striped area) to agree with the combined-slip adhesion force (densely striped area).

Property 9 (Region invariant slide-forces). *The combined-slip slide forces are related to the region-invariant pure-slip slide forces as*

$$F_{sx}(\sigma_x, \sigma_y) = \theta_x(\sigma_{0x}^{\mathrm{reg}}) F_{0x}(\sigma_{0x}^{\mathrm{reg}}) |\cos(\beta_f)| \tag{79a}$$
$$F_{sy}(\sigma_x, \sigma_y) = \theta_y(\sigma_{0y}^{\mathrm{reg}}) F_{0y}(\sigma_{0y}^{\mathrm{reg}}) |\sin(\beta_f)| \tag{79b}$$

Proof. See Appendix A.7. □

Remark 7. The sliding region at the combined slip (σ_x, σ_y) is equal to the sliding region at the region-invariant pure-slips $\sigma_{0x}^{\mathrm{reg}}$ and $\sigma_{0y}^{\mathrm{reg}}$. This is illustrated in Figure 20.

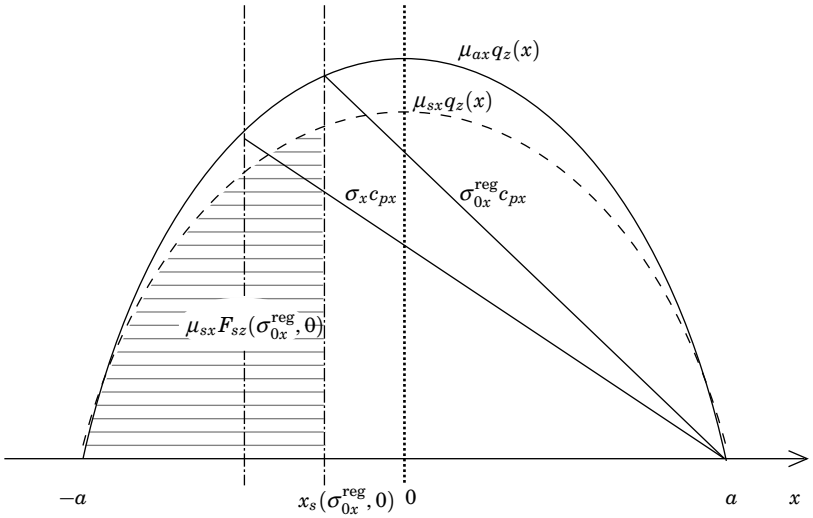

Figure 20 Region-invariant scaling of the slide-force. Since the sliding regions are equal for the combined slip and the region-ivariant pure-slip then $F_{sz}(\sigma_x, \sigma_y) = F_{sz}(\sigma_{0x}^{\text{reg}}, 0)$. The combined slide-force $F_{sx}(\sigma_x, \sigma_y)$ is obtained by multiplying $\mu_{sx}F_{sz}(\sigma_x, \sigma_y)$ by $cos(\beta_f)$.

Property 10 (Slip-velocity invariant pure-slips). *Define the slip-velocity invariant pure-slips as*

$$\sigma_{0x}^{\text{vel}} \triangleq \frac{\sqrt{\sigma_x^2 + \sigma_y^2}\,\text{sgn}(\sigma_x)}{\frac{v_0}{v}\sqrt{(1+\sigma_x)^2 + \sigma_y^2} - \sqrt{\sigma_x^2 + \sigma_y^2}\,\text{sgn}\,(\sigma_x)} \tag{80a}$$

$$\sigma_{0y}^{\text{vel}} \triangleq \frac{\sqrt{\sigma_x^2 + \sigma_y^2}\,\text{sgn}(\sigma_y)}{\sqrt{\left(\frac{v_0}{v}\right)^2 \left((1+\sigma_x)^2 + \sigma_y^2\right) - (\sigma_x^2 + \sigma_y^2)}} \tag{80b}$$

Then the pure slips $(\sigma_{0x}^{\text{vel}}, 0)$ *and* $(0, \sigma_{0y}^{\text{vel}})$ *at the velocity* v_0 *give the same slip velocity,* v_s*, as the combined slip* (σ_x, σ_y) *at velocity* v*.*

Proof. See Appendix A.8. □

Property 11 (Slip-velocity invariant slide forces).
The combined-slip slide forces are related to the slip-velocity invariant pure-slip slide forces as

$$F_{sx}(\sigma_x, \sigma_y) = F_{0x}(\sigma_{0x}^{\text{vel}})\theta_x(\sigma_{0x}^{\text{vel}})|\cos\,(\beta_f)| \cdot \Gamma_x^{\text{vel}} \tag{81a}$$

$$F_{sy}(\sigma_x, \sigma_y) = F_{0y}(\sigma_{0y}^{\text{vel}})\theta_y(\sigma_{0y}^{\text{vel}})|\sin\,(\beta_f)| \cdot \Gamma_y^{\text{vel}} \tag{81b}$$

with

$$\Gamma_x^{\text{vel}} \triangleq \begin{cases} \dfrac{(3-2\psi(\sigma_x,\sigma_y))}{(3-2\psi(\sigma_{0x}^{\text{vel}},0))}\left(\sigma_x^\circ\left(\dfrac{1}{\sigma_x^\circ}|\cos(\beta)|\cos(\beta^\circ)+\dfrac{1}{\sigma_y^\circ}|\sin(\beta)|\sin(\beta^\circ)\right)\right)^2 \\ \cdot\left(\dfrac{v_0}{v}\sqrt{(1+\sigma_x)^2+\sigma_y^2}-\sqrt{\sigma_x^2+\sigma_y^2}\,\text{sgn}(\sigma_x)\right)^2, \\ \qquad\qquad\qquad\qquad\qquad\qquad \textit{if } \psi(\sigma_x,\sigma_y)<1 \textit{ and } \psi(\sigma_{0x}^{\text{vel}},0)<1 \\ \dfrac{1}{\psi^2(\sigma_{0x}^{\text{vel}},0)(3-2\psi(\sigma_{0x}^{\text{vel}},0))}, \qquad \textit{if } \psi(\sigma_x,\sigma_y)\geq 1 \textit{ and } \psi(\sigma_{0x}^{\text{vel}},0)<1 \\ \psi^2(\sigma_x,\sigma_y)(3-2\psi(\sigma_x,\sigma_y)), \qquad \textit{if } \psi(\sigma_x,\sigma_y)<1 \textit{ and } \psi(\sigma_{0x}^{\text{vel}},0)\geq 1 \\ 1, \qquad\qquad\qquad\qquad \textit{if } \psi(\sigma_x,\sigma_y)\geq 1 \textit{ and } \psi(\sigma_{0x}^{\text{vel}},0)\geq 1 \end{cases} \tag{82a}$$

and

$$\Gamma_y^{\text{vel}} \triangleq \begin{cases} \dfrac{(3-2\psi(\sigma_x,\sigma_y))}{(3-2\psi(0,\sigma_{0y}^{\text{vel}}))}\left(\sigma_y^\circ\left(\dfrac{1}{\sigma_x^\circ}|\cos(\beta)|\cos(\beta^\circ)+\dfrac{1}{\sigma_y^\circ}|\sin(\beta)|\sin(\beta^\circ)\right)\right)^2 \\ \cdot\left(\left(\dfrac{v_0}{v}\right)^2\left((1+\sigma_x)^2+\sigma_y^2\right)-(\sigma_x^2+\sigma_y^2)\right), \\ \qquad\qquad\qquad\qquad\qquad\qquad \textit{if } \psi(\sigma_x,\sigma_y)<1 \textit{ and } \psi(0,\sigma_{0y}^{\text{vel}})<1 \\ \dfrac{1}{\psi^2(0,\sigma_{0y}^{\text{vel}})(3-2\psi(0,\sigma_{0y}^{\text{vel}}))}, \qquad \textit{if } \psi(\sigma_x,\sigma_y)\geq 1 \textit{ and } \psi(0,\sigma_{0y}^{\text{vel}})<1 \\ \psi^2(\sigma_x,\sigma_y)(3-2\psi(\sigma_x,\sigma_y)), \qquad \textit{if } \psi(\sigma_x,\sigma_y)<1 \textit{ and } \psi(0,\sigma_{0y}^{\text{vel}})\geq 1 \\ 1, \qquad\qquad\qquad\qquad \textit{if } \psi(\sigma_x,\sigma_y)\geq 1 \textit{ and } \psi(0,\sigma_{0y}^{\text{vel}})\geq 1 \end{cases} \tag{82b}$$

Proof. See Appendix A.9. □

Remark 8. There is no clear graphical interpretation of the slip-velocity invariant pure-slips. Note that to obtain the same slip-velocity for combined and pure slips it is necessary to take into account the corresponding wheel-center velocities, v and v_0, which may be different.

Property 12 (Slip-velocity component invariant pure-slips).
Define the slip-velocity component invariant pure-slips as

$$\sigma_{0x}^{\text{velc}} \triangleq \frac{\sigma_x}{\dfrac{v_0}{v}\sqrt{(1+\sigma_x)^2+\sigma_y^2}-\sigma_x} \tag{83a}$$

$$\sigma_{0y}^{\text{velc}} \triangleq \frac{\sigma_y}{\sqrt{\left(\dfrac{v_0}{v}\right)^2\left((1+\sigma_x)^2+\sigma_y^2\right)-\sigma_y^2}} \tag{83b}$$

Then the pure slips $(\sigma_{0x}^{\text{velc}},0)$ *and* $(0,\sigma_{0y}^{\text{velc}})$ *at the velocity* v_0 *gives the same slip velocity components* (v_{sx},v_{sy}) *as the combined slip* (σ_x,σ_y) *at velocity* v.

Proof. See Appendix A.10. □

Property 13 (Slip-velocity component invariant slide forces).
The combined-slip slide forces are related to the pure-slip slide forces as

$$F_{sx}(\sigma_x,\sigma_y) = F_{0x}(\sigma_{0x}^{\text{velc}}) \cdot \Gamma_x^{\text{velc}} \tag{84a}$$

$$F_{sy}(\sigma_x,\sigma_y) = F_{0y}(\sigma_{0y}^{\text{velc}}) \cdot \Gamma_y^{\text{velc}} \tag{84b}$$

with

$$\Gamma_x^{\text{velc}} \triangleq \begin{cases} \dfrac{\psi(\sigma_x,\sigma_y)(3-2\psi(\sigma_x,\sigma_y))}{3\rho_x\left(1-\psi(\sigma_{0x}^{\text{velc}},0)\right)^2+\psi(\sigma_{0x}^{\text{velc}},0)\left(3-2\psi(\sigma_{0x}^{\text{velc}},0)\right)} \\ \cdot\sigma_x^\circ\left(\dfrac{1}{\sigma_x^\circ}|\cos(\beta)|\cos(\beta^\circ)+\dfrac{1}{\sigma_y^\circ}|\sin(\beta)|\sin(\beta^\circ)\right) \\ \cdot\left(\dfrac{v_0}{v}\sqrt{(1+\sigma_x)^2+\sigma_y^2}-\sigma_x\right) & \text{if } \psi(\sigma_x,\sigma_y)<1 \text{ and } \psi(\sigma_{0x}^{\text{velc}},0)<1 \\ \dfrac{\left(\dfrac{v_0}{v}\sqrt{(1+\sigma_x)^2+\sigma_y^2}-\sigma_x\right)}{3\rho_x\left(1-\psi(\sigma_{0x}^{\text{velc}},0)\right)^2+\psi(\sigma_{0x}^{\text{velc}},0)\left(3-2\psi(\sigma_{0x}^{\text{velc}},0)\right)}\dfrac{\sigma_x^\circ}{\sqrt{\sigma_x^2+\sigma_y^2}}, & \text{if } \psi(\sigma_x,\sigma_y)\geq 1 \text{ and } \psi(\sigma_{0x}^{\text{velc}},0)<1 \\ \psi^2(\sigma_x,\sigma_y)(3-2\psi(\sigma_x,\sigma_y))|\cos(\beta)|, & \text{if } \psi(\sigma_x,\sigma_y)<1 \text{ and } \psi(\sigma_{0x}^{\text{velc}},0)\geq 1 \\ |\cos(\beta)|, & \text{if } \psi(\sigma_x,\sigma_y)\geq 1 \text{ and } \psi(\sigma_{0x}^{\text{velc}},0)\geq 1 \end{cases} \tag{85a}$$

and

$$\Gamma_y^{\text{velc}} \triangleq \begin{cases} \dfrac{\psi(\sigma_x,\sigma_y)(3-2\psi(\sigma_x,\sigma_y))}{3\rho_y\left(1-\psi(0,\sigma_{0y}^{\text{velc}})\right)^2+\psi(\sigma_{0y}^{\text{velc}},0)\left(3-2\psi(0,\sigma_{0y}^{\text{velc}})\right)} \\ \cdot\sigma_y^\circ\left(\dfrac{1}{\sigma_x^\circ}|\cos(\beta)|\cos(\beta^\circ)+\dfrac{1}{\sigma_y^\circ}|\sin(\beta)|\sin(\beta^\circ)\right) \\ \cdot\sqrt{\left(\dfrac{v_0}{v}\right)^2\left((1+\sigma_x)^2+\sigma_y^2\right)-\sigma_y^2}, & \text{if } \psi(\sigma_x,\sigma_y)<1 \text{ and } \psi(0,\sigma_{0y}^{\text{velc}})<1 \\ \dfrac{\sqrt{\left(\frac{v_0}{v}\right)^2\left((1+\sigma_x)^2+\sigma_y^2\right)-\sigma_y^2}}{3\rho_y\left(1-\psi(0,\sigma_{0y}^{\text{velc}})\right)^2+\psi(0,\sigma_{0y}^{\text{velc}})\left(3-2\psi(0,\sigma_{0y}^{\text{velc}})\right)}\dfrac{\sigma_y^\circ}{\sqrt{\sigma_x^2+\sigma_y^2}}, & \text{if } \psi(\sigma_x,\sigma_y)\geq 1 \text{ and } \psi(0,\sigma_{0y}^{\text{velc}})<1 \\ \psi^2(\sigma_x,\sigma_y)(3-2\psi(\sigma_x,\sigma_y))|\sin(\beta)|, & \text{if } \psi(\sigma_x,\sigma_y)<1 \text{ and } \psi(0,\sigma_{0y}^{\text{velc}})\geq 1 \\ |\sin(\beta)|, & \text{if } \psi(\sigma_x,\sigma_y)\geq 1 \text{ and } \psi(0,\sigma_{0y}^{\text{velc}})\geq 1 \end{cases} \tag{85b}$$

Proof. See Appendix A.11. □

Remark 9. There is no clear graphical interpretation of the slip-velocity component invariant pure-slips. Note that to obtain the same slip-velocity components for combined and pure slips it is necessary to take into account the corresponding wheel-center velocities, v and v_0, which may be different. The slip-velocity component invariant scaling is restricted to slip-projection sliding friction.

Property 14 (Region-invariant aligning torque). *The combined-slip self-aligning torque is related to the region-invariant pure-slip lateral force and aligning moment as*

$$\begin{aligned} &M'_z(\sigma_x,\sigma_y) \\ &= M_{0z}(\sigma_{0y}^{\mathrm{reg}})|\sin(\beta)| + (1-\theta_y(\sigma_{0y}^{\mathrm{reg}}))t_{0a}(\sigma_{0y}^{\mathrm{reg}})F_{0y}(\sigma_{0y}^{\mathrm{reg}})(\sin(\beta^\circ)-|\sin(\beta)|) \end{aligned} \tag{86}$$

where

$$t_{0a}(\sigma_{0y}^{\mathrm{reg}}) \triangleq t_a(0,\sigma_{0y}^{\mathrm{reg}}) = \frac{C_z}{C_y}(4\psi(\sigma_x,\sigma_y)-1) \tag{87}$$

Proof. See Appendix A.12. □

Property 15 (Region-invariant additional aligning torque). *The combined-slip deformation torque is related to the region-invariant pure-slip lateral force and aligning moment as*

$$M''_{az}(\sigma_x,\sigma_y) = \frac{12\,a\rho_x\rho_y\,(1-\psi(\sigma_x,\sigma_y))^3}{\Gamma_{zx}\Gamma_{zy}}\left(\frac{1}{C_x}-\frac{1}{C_y}\right)F_{0x}(\sigma_{0x}^{\mathrm{reg}})F_{0y}(\sigma_{0y}^{\mathrm{reg}}) \tag{88a}$$

at partial sliding $(\psi(\sigma_x,\sigma_y)<1)$*, otherwise* $M''_{az}(\sigma_x,\sigma_y)=0$*, and*

$$M''_{sz}(\sigma_x,\sigma_y) = \frac{6\Gamma_z}{5\Gamma_{zx}\Gamma_{zy}}a\left(\frac{1}{C_x}-\frac{1}{C_y}\right)F_{0x}(\sigma_{0x}^{\mathrm{reg}})F_{0y}(\sigma_{0y}^{\mathrm{reg}})|\cos(\beta_f)||\sin(\beta_f)| \tag{88b}$$

where

$$\Gamma_{zx} \triangleq 3\rho_x\,(1-\psi(\sigma_x,\sigma_y))^2 + \psi(\sigma_x,\sigma_y)\,(3-2\psi(\sigma_x,\sigma_y)) \tag{89a}$$

$$\Gamma_{zy} \triangleq 3\rho_y\,(1-\psi(\sigma_x,\sigma_y))^2 + \psi(\sigma_x,\sigma_y)\,(3-2\psi(\sigma_x,\sigma_y)) \tag{89b}$$

$$\Gamma_z \triangleq \left(10-15\psi(\sigma_x,\sigma_y)+6\psi^2(\sigma_x,\sigma_y)\right)\psi(\sigma_x,\sigma_y) \tag{89c}$$

at partial sliding $(\psi(\sigma_x,\sigma_y)<1)$*, otherwise* $\Gamma_{zx}=\Gamma_{zy}=\Gamma_z=1$*.*

Proof. See Appendix A.13. □

Property 16 (Slip-velocity invariant additional aligning-torque). *The combined-slip deformation torque is related to the slip-velocity invariant pure-slip lateral force and aligning moment as*

$$M''_{az}(\sigma_x,\sigma_y) = 12\,a\rho_x\rho_y\,(1-\psi(\sigma_x,\sigma_y))^3\left(\frac{1}{C_x}-\frac{1}{C_y}\right)\frac{F_{0x}(\sigma_x)F_{0y}(\sigma_y)}{\Gamma_{zx}\Gamma_{zy}} \tag{90a}$$

at partial sliding $(\psi(\sigma_x,\sigma_y)<1)$*, otherwise* $M''_{az}(\sigma_x,\sigma_y)=0$*, and*

$$M''_{sz}(\sigma_x,\sigma_y) = \Gamma''_z\frac{6}{5}a\left(\frac{1}{C_x}-\frac{1}{C_y}\right)F_{0x}(\sigma_{0x}^{\mathrm{vel}})\Gamma_x^{\mathrm{vel}}F_{0y}(\sigma_{0y}^{\mathrm{vel}})\Gamma_y^{\mathrm{vel}}|\cos(\beta)| \tag{90b}$$

where

$$\Gamma_{zx} \triangleq \begin{cases} 3\rho_x\,(1-\psi(\sigma_x,0))^2 + \psi(\sigma_x,0)\,(3-2\psi(\sigma_x,0))\,, & \text{if } \psi(\sigma_x,0)<1 \\ 1, & \text{otherwise} \end{cases} \tag{91a}$$

$$\Gamma_{zy} \triangleq \begin{cases} 3\rho_y \left(1-\psi(0,\sigma_y)\right)^2 + \psi(0,\sigma_y)\left(3-2\psi(0,\sigma_y)\right), & \text{if } \psi(0,\sigma_y) < 1 \\ 1, & \text{otherwise} \end{cases} \tag{92a}$$

and

$$\Gamma''_z \triangleq \begin{cases} \dfrac{\left(10-15\psi(\sigma_x,\sigma_y)+6\psi^2(\sigma_x,\sigma_y)\right)\theta_x(\sigma_{0x}^{\text{vel}})(3-2\psi(0,\sigma_{0y}^{\text{vel}}))}{(3-2\psi(\sigma_x,\sigma_y))^2\left(3\rho_y\left(1-\psi(0,\sigma_{0y}^{\text{vel}})\right)^2+\psi(0,\sigma_{0y}^{\text{vel}})\left(3-2\psi(0,\sigma_{0y}^{\text{vel}})\right)\right)} \cdot \dfrac{\sin(\beta^\circ)}{\sqrt{\left(\dfrac{v_0}{v}\right)^2((1+\sigma_x)^2+\sigma_y^2)-(\sigma_x^2+\sigma_y^2)}}, & \\ & \text{if } \psi(\sigma_x,\sigma_y) < 1 \text{ and } \psi(0,\sigma_{0y}^{\text{vel}}) < 1 \\ \theta_x(\sigma_{0x}^{\text{vel}})\theta_y(\sigma_{0y}^{\text{vel}})|\sin(\beta)|, & \text{if } \psi(\sigma_x,\sigma_y) \geq 1 \text{ and } \psi(0,\sigma_{0y}^{\text{vel}}) < 1 \\ \dfrac{10-15\psi(\sigma_x,\sigma_y)+6\psi^2(\sigma_x,\sigma_y)}{(3-2\psi(\sigma_x,\sigma_y))^2\psi(\sigma_x,\sigma_y)}\theta_x(\sigma_{0x}^{\text{vel}})|\sin(\beta)|, & \\ & \text{if } \psi(\sigma_x,\sigma_y) < 1 \text{ and } \psi(0,\sigma_{0y}^{\text{vel}}) \geq 1 \\ |\sin(\beta)|, & \text{if } \psi(\sigma_x,\sigma_y) \geq 1 \text{ and } \psi(0,\sigma_{0y}^{\text{vel}}) \geq 1 \end{cases} \tag{93a}$$

with Γ_x^{vel}, Γ_y^{vel}, σ_x^{vel} *and* σ_y^{vel} *from Property 11 and* θ_x *and* θ_y *from Property 3.*

Proof. See Appendix A.14. □

4. Semi-Empirical Combined Slip Model

The idea of the proposed model is to use the properties of Section 3 with $F_{0x}(\sigma_x)$, $F_{0y}(\sigma_y)$, and $M_{0z}(\sigma_y)$ described by empirical data $\hat{F}_{0x}$, $\hat{F}_{0y}$, and $\hat{M}_{0z}$. In essence, this means that (70) and (71) are used to estimate sliding and adhesive force components from the empirical pure-slip data. Thereafter, combined forces are constructed using scaling factors based on the brush model.

Model for combined-slip tire-forces. *A semi-empirical combined-slip model based on pure-slip scaling is obtained by using empirical pure-slip models* $\hat{F}_{0x}$, $\hat{F}_{0y}$, *and* $\hat{M}_{0z}$ *in combination with:*

- *Property 5 or 8 to compute the semi-empirical adhesion force* $\hat{F}_{ax}$,
- *Property 6, 9, 11, or 13 to compute the semi-empirical slide force* $\hat{F}_{sx}$,
- *Property 14 together with 15 or 16 to compute the semi-empirical aligning-moments* $\hat{M}'_z$ *and* $\hat{M}''_z$.

The total semi-empirical combined forces are then $\hat{F}_x = \hat{F}_{ax} + \hat{F}_{sx}$, $\hat{F}_y = \hat{F}_{ay} + \hat{F}_{sy}$ *and the total semi-empirical aligning-moment is* $\hat{M}_z = \hat{M}'_z + \hat{M}''_z$.

The empirical pure-slip data include several effects which are not present in the theoretical brush-model. The most prominent are the mismatch of the lateral stiffness at partial sliding due to carcass flexibility and the apparent velocity dependence of the sliding friction. Still, the effects will be included in the proposed combined-slip models as they essentially are scalings of the empirical data. In the special case of pure-slip, these effects will be correctly reproduced. Otherwise, the different choices of invariant pure-slips σ_{0x} and σ_{0y} of Properties 4, 7, 10, and 12 aim at reproducing particular effects correctly in combined-slip.

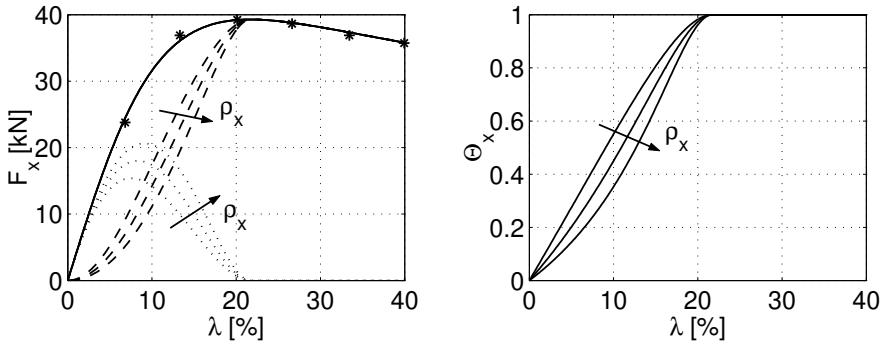

Figure 21 Separation of pure-slip longitudinal adhesion and slide forces using Property 3 for $\rho_x = \mu_{ax}/\mu_{sx} \in \{0.5, 1.0, 1.5\}$. Left: pure-slip empirical data ('*'), corresponding Magic Formula model (solid line), adhesion force-fraction (dotted line), slide force-fraction (dashed line). Right: θ_x. The curves are located lower with increasing value of the ratio.

It is clear that adhesive forces originate in deformation of the tire, and are therefore best described as a function of $\bar{\sigma}$ which translates directly to deformation. The sliding forces, on the other hand, are better decribed as a function of the slip-velocity $\bar{v}_s$. When translating empirical pure-slip data to combined-slip forces using the properties of Section 3 it therefore makes sense to use different pure-slips for adhesive and sliding forces. For the adhesive force the pure-slips that preserve deformation or adhesive-region size seem appropriate, while the pure-slips that preserve slip-velocity seems more natural for the sliding force.

4.1 Parameters

Only four parameters are involved in the models: σ_x°, σ_y°, ρ_x, and ρ_y, all with clear physical interpretations. The parameters σ_x° and σ_y° describe the pure slips where transition from partial to full sliding occur and are needed to compute $\psi(\sigma_x, \sigma_y)$. A common assumption is that these transitions occur at the friction peak. Hence, they may simply be set to the slip value corresponding to the force peaks in $F_{0x}(\sigma_x)$ and $F_{0y}(\sigma_y)$. The remaining parameters ρ_x, and ρ_y reflects the ratio between the adhesive and sliding friction coefficients. It is not uncommon to assume equal adhesive and sliding friction, i.e. $\rho_x = \rho_y = 1$, and this will normally result in satisfactory results. On friction curves with very pronounced force peaks then $\rho_x > 1$ and $\rho_y > 1$ may give more accurate results. In general, the adhesive-friction coefficient is larger than the sliding-friction coefficient, and $\rho_x > 1$, $\rho_y > 1$.

If only pure-slip empirical data is available then the nominal values given above are natural choices. If combined-slip empirical data is available, then the parameters may be optimized for best fit.

Figure 21 illustrates the effect of the parameter $\rho_x = \mu_{ax}/\mu_{sx}$ on the estimation of adhesive and sliding forces from empirical data using (70). With larger ρ the estimated adhesive fraction of the total force becomes larger, as expected.

4.2 Slip Parameterization

The brush-model and, consequently, the proposed model are based on the slip $\bar{\sigma}$ defined by (5a). This slip has the disadvantage of growing to infinity at wheel-lock. When implementing the proposed model $\bar{\sigma}$ needs to be translated to a more practical slip. It is assumed that the empirical pure-slip models are parameterized in λ and α as $\hat{F}_{0x}(\lambda)$, $\hat{F}_{0y}(\alpha)$ and $\hat{M}_{0z}(\alpha)$, which is common, and also that λ and α are used as inputs to the combined-slip model. Translations of the model expressions to λ and α are given in Appendix B.

4.3 Magic Formula

The proposed model is convenient to use with Magic Formula pure-slip models.

In this case $\hat{F}_{0x}(\lambda)$, $\hat{F}_{0y}(\alpha)$ and $\hat{M}_{0z}(\alpha)$ are described by the Magic Formula equations (12) with the corresponding parameters $(B, C, D, E)_{x,y,z}$. Since the force-peak values are given by Magic-Formula parameters as $\hat{F}^*_{0x} = (D)_x$, $\hat{F}^*_{0y} = (D)_y$ and the cornering and braking stiffnesses as $\hat{C}_\lambda = (BCD)_x$, $\hat{C}_\alpha = (BCD)_y$ then the parameters σ°_x and σ°_y may be conveniently estimated as

$$\hat{\sigma}^\circ_x = \frac{3}{(BC)_x} \tag{94a}$$

$$\hat{\sigma}^\circ_y = \frac{3 \cdot 180}{(BC)_y \pi} \tag{94b}$$

This follows from (32) using (53) under the assumption that $\rho_x = \rho_y = 1$. Then the peak forces are $F^*_{0x} = F_z\mu_{ax} = F_z\mu_{sx}$ and $F^*_{0y} = F_z\mu_{ay} = F_z\mu_{sy}$. The factor $180/\pi$ is due to α being expressed in degrees.

Compensation for flexible carcass As mentioned previously the brush model described in Section 2 is based on the assumption of a stiff carcass. In reality the carcass is flexible and exhibits significant deformation laterally. One effect of the flexible carcass is that Equation (32), and therefore also (94b), no longer hold. It is, however, possible to adjust (94b) to compensate for the carcass flexibility.

Let $F'_y(\sigma_y)$ denote the lateral tire-force for a tire with flexible carcass. Regard again how the deformation of an infinitesimal bristle element at position x in the adhesive region, $\delta_y(x)$, is described by (24). This is a purely kinematic relation which holds also in the case of flexible carcass. However, in the case of flexible carcass then $\delta_y(x)$ is the sum of the bristle and carcass deflections $\delta_{yb}(x)$ and $\delta_{yc}(x)$

$$\delta_y(x) = \delta_{yb}(x) + \delta_{yc}(x) \tag{95}$$

There are several theories on how to describe the carcass deformation and here the simplest one is used

$$\delta_{yc}(x) = -\frac{F'_y(\sigma_y)}{C_c}(a - x) \tag{96}$$

where C_c is the carcass stiffness. From (95), (96) and (24) it holds that

$$\delta_{yb}(x) = -(\sigma_y - \frac{F'_y(\sigma_y)}{C_c})(a - x) \tag{97}$$

The force acting on the bristle element at x will then be

$$dF'_y(x) = c_{py}\delta_{yb}(x)\,dx = -c_{py}(\sigma_y - \frac{F'_y(\sigma_y)}{C_c})(a - x)\,dx \tag{98}$$

Equation (27) at pure lateral slip together with the expression (29) for the pressure distribution is used to calculate the break-away point

$$c_{py}\,(\sigma_y - \frac{F'_y(\sigma_y)}{C_c}) = \frac{3\mu_{ay}F_z}{4a^3}\,(a + x_s) \tag{99}$$

When the entire contact patch slides then $x_s = a$, $\sigma_y = \sigma^{\circ\prime}_y$, and $F'_y(\sigma^{\circ\prime}_y) = \mu_{sy}F_z$. Solving (99) for $\sigma^{\circ\prime}_y$ under these conditions gives

$$\sigma^{\circ\prime}_y = \frac{3F_z\mu_{ay}}{2a^2c_{py}} + \frac{\mu_{sy}F_z}{C_c} = F_z\left(\frac{3\mu_{ay}}{2a^2c_{py}} + \frac{\mu_{sy}}{C_c}\right) \tag{100}$$

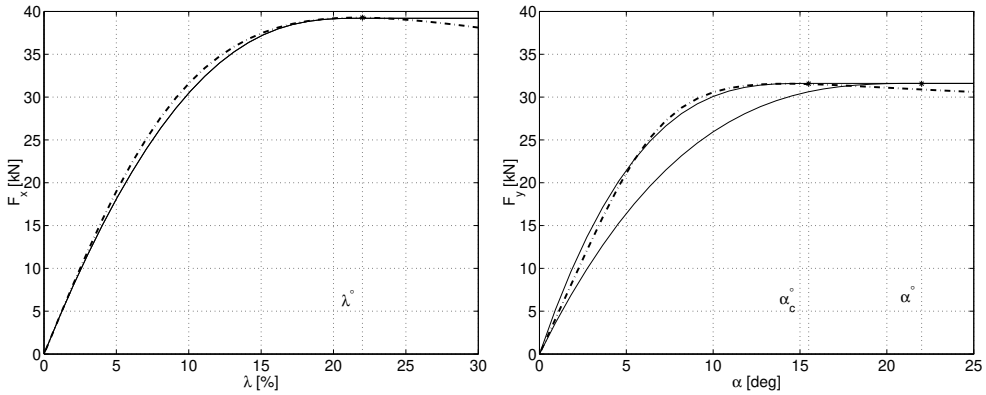

Figure 22 Brush-model forces (solid) and magic-formula empirical data (dash-dotted). Left: Longitudinal force with α° corresponding to σ_x° given by (94a). Right: Lateral force with σ_y° given by (94b) (lower solid line) or (105) (upper solid line). Note that the adjustment for flexible carcass results in significantly better fit.

Next step is to derive an expression for the relation between C_c and the cornering stiffness C_y. At very small slips $\sigma_y \approx 0$ there is no sliding in the contact patch and the tire force only consists of adhesive force. Therefore,

$$C_y' = \left.\frac{dF_y'(\sigma_y)}{d\sigma_y}\right|_{\sigma_y=0} = -\left.\frac{d}{d\sigma_y}\left(\int_{-a}^{a} c_{py}\delta_b(x)\,dx\right)\right|_{\sigma_y=0}$$
$$= 2a^2 c_{py}\left(1 - \frac{1}{C_c}\left.\frac{dF_y'(\sigma_y)}{d\sigma_y}\right|_{\sigma_y=0}\right) = C_y\left(1 - \frac{C_y'}{C_c}\right) \quad (101)$$

where $2a^2 c_{py} = C_y$ according to (53). Hence,

$$C_y' = \frac{C_y}{1 + \dfrac{C_y}{C_c}} \quad (102)$$

Further, the rubber will be assumed to behave isotropicly, $C_y = C_x$, which is a realistic assumption. (In Section 2 the carcass deformation was included in the lateral rubber stiffness.) Then the carcass stiffness can be calculated from (102) as

$$C_c = \frac{C_x C_y'}{C_x - C_y'} \quad (103)$$

Using (103) then the limit-slip adjusted for carcass deformation of (100), $\sigma_y^{\circ\prime}$, can be written as

$$\sigma_y^{\circ\prime} = F_z \mu_{ay}\left(\frac{2}{C_x} + \frac{1}{C_y'}\right) \quad (104)$$

Using $F_y^* = F_z\mu_{ay}$ and $\hat{F}_y^* = D_y$, $\hat{C}_x = (BCD)_x$, and $\hat{C}_y' = (BCD)_y \cdot 180/\pi$ then

$$\sigma_y^{\circ\prime} = D_y\left(\frac{2}{(BCD)_x} + \frac{\pi}{180\cdot(BCD)_y}\right) \quad (105)$$

In Figure 22 the effect of adjusting the lateral limit-slip to compensate for flexible carcass is illustrated. Note that the original expression for σ_y°, (94b), overestimates the limit-slip, resulting in poor fit with the brush-model. With the modified expression, (105), the fit is equally good as in the longitudinal direction.

4.4 Utilizing Braking Data to Generate Driving Data

In the proposed model it is assumed that the given empirical pure-slip model $\hat{F}_{0x}(\lambda)$ is valid both at braking ($\lambda > 0$) and driving ($\lambda < 0$). The Magic Formula is an odd function and therefore $\hat{F}_{0x}(\lambda) = -\hat{F}_{0x}(-\lambda)$. In general, this is not in accordance with empirical observations. If the pure-slip model is assumed to be valid for braking, then the following procedure suggests how to modify the argument to the pure-slip model at driving so that a more accurate force is obtained.

The pure-slip longitudinal force consists of one adhesive part and one sliding part. For the adhesive part the generated force is dependent on the deformation. The brush model states that the force developed at driving with slip $\sigma_x < 0$ will have the same size and the opposite sign as the force as generated at braking with slip $-\sigma_x$, i.e.

$$F_{0ax}(\sigma_x) = -F_{0ax}(-\sigma_x) \tag{106}$$

With $\sigma_x = \lambda_{\text{driving}}/(1-\lambda_{\text{driving}})$ and $-\sigma_x = \lambda_{\text{braking}}/(1-\lambda_{\text{braking}})$ this means that

$$\lambda_{\text{braking}} = -\frac{\lambda_{\text{driving}}}{1-2\lambda_{\text{driving}}} \tag{107}$$

Hence, when computing adhesive forces using an empirical model for braking then the pure-slip forces

$$\begin{cases} -\hat{F}_{0x}(\frac{-\lambda}{1-2\lambda}), & \lambda < 0 \\ \hat{F}_{0x}(\lambda), & \lambda \geq 0 \end{cases} \tag{108}$$

are best used for driving and braking respectively.

For the sliding case it is more natural to let the force depend on the relative velocity $v_s = \lambda v_x$. Then $-v_s$ will simply correspond to $-\lambda$. Therefore, when computing slide forces using an empirical model for braking then the pure-slip forces

$$\begin{cases} -\hat{F}_{0x}(-\lambda), & \lambda < 0 \\ \hat{F}_{0x}(\lambda), & \lambda \geq 0 \end{cases} \tag{109}$$

are best used for driving and braking respectively.

In the upper plot of Figure 23 the effect of the described procedure is visible for negative λ.

5. Validation and Discussion

5.1 Validation

Empirical data from a truck-tire is used to exemplify the proposed combined-slip models. The data is provided by Volvo Truck Corporation [10] and consists of pure-slip data with corresponing Magic Formula parameters, and two sets of combined-slip data for fixed slip-angles $\alpha = 4.7$ deg and $\alpha = 9.8$ deg with varying slip-ratios $\lambda \in [0, 1]$. The details on tire brand and model is confidential.

From the two proposed adhesive-force and eight proposed sliding-force combined-slip models a total of sixteen models for total combined-slip forces are obtained. All sixteen models reduce to the empirical model at pure-slip, see Figure 12. In Figures 32, 33, and 31 in Appendix D all sixteen models are compared with the combined-slip empirical data. The resulting tire-forces for constant $\alpha = 4.7$ deg and $\alpha = 9.8$ deg as λ is swept from 0 to 1 are plotted. The combined force accoring to the COMBINATOR-model (21) [28] is also shown for comparison. It can immidately be seen from the figures that all proposed models give similar performance, and that the COMBINATOR model differs especially at $\alpha = 4.7$ deg.

The difference between the models is which pure-slips, σ_{0x}, σ_{0y}, that are used in the empirical pure-slip models when computing the combined-slip force. The

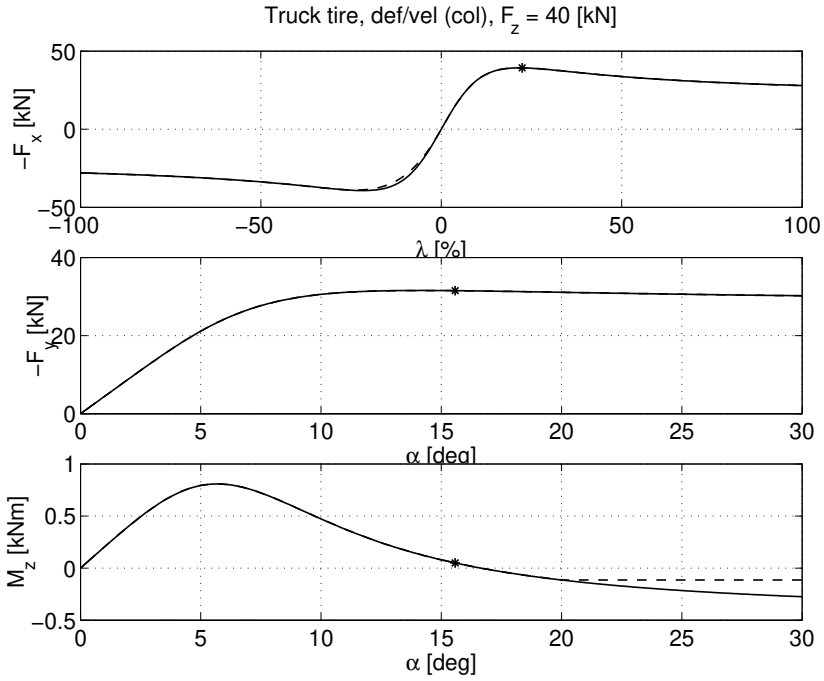

Figure 23 Pure-slip forces and self-aligning moment for the empirical pure-slip model (solid lines) and the proposed semi-empirical models (dashed lines). All proposed semi-empirical models are identical in pure-slip. The limit slips λ° and α° are marked by "*". The deviation at $\lambda < 0$ in the longitudinal direction results from using the procedure of Section 4.4 for driving. Since the Magic Formula is valid for $|\alpha| < 20$ deg the aligning-torque data for $\alpha = \pm 20$ deg are used for larger slip-angles.

pure-slips used are the deformation invariant ("def") and the velocity-component invariant ("velc") pure-slips, which are related to the components of the combined-slip. The region invariant ("reg") and the velocity invariant ("vel") pure-slips, which are related to the magnitude of the combined-slip. The pure-slips which are related to the magnitude of the combined-slip may grow significantly larger than the respective components of the combined slip. E.g., for a combined slip $\bar{\sigma} = (\sigma_x, \sigma_y)$ the pure-slips σ_{0x} and σ_{0y} that are used with the empirical pure-slip data will both be of a size in the order of $|\bar{\sigma}|$. This means that even if $\sigma_x \approx 0$ then $\sigma_{0x} \approx \sigma_y$ when σ_y grows, and vice versa. This requires valid empirical data at large slips in both directions.

It can be seen in the figures that the "def" and "velc" models differ slightly qualitatively from the "reg" and "vel" models. This can be explained by the fact that these models use different parts of the empirical pure-slip data in the construction of the combined forces.

Note that if the empirical data was exactly described by the brush model, the different proposed models would yield identical results. Otherwise, the different models are each designed to emphasize one particular physical source of the produced force.

Adhesion models The effect of choice of adhesion model is only visible at partial sliding, i.e. when $\psi(\sigma_x, \sigma_y) < 1$. The transition to full sliding is marked with an asterisk in the figures.

The deformation-invariant model of Property 5 is based on the empirical pure-slip data which correspond to the same longitudinal and lateral tread deformation as the combined-slip. Since this deformation is assumed to be the source of the adhesive force, this model is strongly physically motivated. The model seems to perform well when compared to the validation data. Differences are best explained by limitations of the empirical data as noted below.

The adhesive-region invariant model of Property 8 is based on the empirical pure-slip data which correspond to the same size of the adhesive region as the combined-slip. This is in analogy with the approach of the combined-slip model (18) proposed in [2]. The performance of this model is not distinguishable from the deformation-invariant model.

Sliding models The effect of choice of adhesion model is visible in the full range of slips, both at partial and full sliding.

A first general observation is that the sliding-force models which are based on collinear or slip-projection sliding-friction seem to show best agreement with validation data at large slips. Since the MDR friction-model shows poor agreement it can be concluded that the friction is not really anisotropic, and that differences in sliding forces in longitudinal and lateral directions at full sliding instead are the result of measurement errors. If the friction characteristics are assumed to be isotropic, the collinear model is the most natural to use.

The deformation-invariant model of Property 6 has a weak physical foundation since the sliding forces do not depend on the deformation explicitly. Since $\bar{\sigma}$ has the interpretation of bristle deformation only at adhesion in partial sliding, it is not even clear what this model means at full sliding. One reason to still examine this model is that in combination with the deformation-invariant model for the adhesive force, the same empirical pure-slip data will be used for adhesive and sliding forces at a particular combined slip. Even if the physical motivation for this model is weak, the validation results are still good. Note that this model can only be formulated without singular expressions when using the slip-projection sliding-friction.

The region-invariant model of Property 9 lacks physical interpretation at full sliding, since there then is no adhesive region. Still, the agreement with validation data is similar to that of the deformation-invariant model. The model can be formulated using any of the collinear, beta-projection, or MDR sliding friction models.

The slip-velocity invariant model of Property 11 is an approach based on the assumption that the sliding force depends primarily on the relative velocity between the tire and the road. Intuitively, this is the most attractive method. A feature with this model is the possibility to take into account the velocity at which the empirical data were measured. The model can be formulated using any of the collinear, beta-projection, or MDR sliding friction models.

The slip-velocity-component invariant model of Property 13 is a modification of the velocity-invariant model to obtain a pure-slip based on the components of the combined-slip. Note that also this model can only be formulated without singular expressions when using the slip-projection sliding-friction.

Self-aligning Moment Model Empirical data for combined-slip self-aligning moment was not available.

5.2 Measurement data

The combined-slip validation data consists of only two measurement sets. A full validation would require more data. The data exhibit a few obvious discrepancies. Firstly, the pure-slip lateral forces in the combined-slip data-sets do not agree with the corresponding forces in the pure-slip data-sets. This may be seen by comparing the data-points for F_y at $F_x = 0$ in Figures 32, 33, and 31 with the corresponding points at $\alpha = 4.7$ deg and $\alpha = 9.8$ deg in Figure 12. Secondly, in the data corresponding to large slips with $\lambda \approx 1$ (wheel-lock) in the combined-slip data-sets there seems to be a discontinuity. Thirdly, the direction of the tire-force at $\lambda = 1$ seems strange. At $\alpha = 4.7$ deg the resulting angular direction of $-\bar{F}$ at $\lambda = 1$ should be 4.7 deg for isotropic sliding friction or 5.0 deg for anisotropic friction according to the Maximum Dissipation-Rate principle. In the data-set it is 1.28 deg. The corresponding figures for 9.8 deg are 10.4 deg for anisotropic friction

and 5.1 deg in the data-set. No obvious explanation has been found to this, and it is assumed that it is the result of measurement errors.

Measurement data for the lateral force and the self-aligning moment is only available for $|\alpha| < 20$ deg and the validity of the fitted Magic Formula model is limited to this range. For $|\alpha| > 20$ deg the data for $\alpha = \pm 20$ deg are used for the self-aligning torque.

5.3 Discussion

Only the MDR sliding-friction model can be disqualified on the basis of the validation data. That leaves 12 candidate models to choose from, which show comparable agreement with measurement data. From these the deformation-invariant adhesion-force model (Property 5) in combination with the collinear slip-velocity invariant sliding-force model (Property 11) is chosen as the most attractive models. This is the physically most motivated combination, and the velocity dependence of the slip-velocity invariant sliding-force model is a valuable feature. This model is further examined below and pseudo-code implementations are given in Appendix E. The region-invariant models (Properties 8 and 9) are the simplest to implement, but the lack of interpretation of the pure-slips at full sliding is a disadvantage. Pseudo-code implementations of the region-invariant models are given in Appendix E.

In Figure 24 the resulting forces and aligning-moment are shown for fixed slip angles α and varying λ ranging from -100% (driving) to 100% (braking with locked wheels). The adhesive and sliding contributions are shown separately for the forces. The adhesive forces is dominating at small slip magnitudes, and vanish at the point of full sliding. For the aligning-moment the contributions from $M'(\sigma_x, \sigma_y)$ and $M''(\sigma_x, \sigma_y)$ are shown separately. It is clear that $M'(\sigma_x, \sigma_y)$ is the dominating part. Note the asymmetrical characteristics with respect to driving ($\lambda < 0$) and braking ($\lambda > 0$). This is essentially an effect of the relation between $\bar{\sigma}$ and $(\lambda, \tan(\alpha))$, see (5). The combined-slip forces and moment agrees qualitatively with observations reported in e.g. [24]. Note that the main contribution to the self-aligning torque is given by M_z', which is the part resulting from the non-symmetric distribution of the lateral force. The additional part M_z'' resulting from tire deformation is smaller. This part is, however, probably underestimated since only the deformation resulting from bristle deflection is accounted for. Figure 25 shows the corresponding case with fixed λ as α is swept from 0 to 30 deg. Negative α are not shown since the characteristics are symmetrical. The comments on Figure 24 apply also for this figure. Figure 26 is similar to Figures 32–31, and shows the combined forces at constant α when λ is swept from -100% to 100%.

For small slips the direction of the tire-force is primarily determined by the stiffness characteristics of the tire. Only at larger slips, when the sliding-friction dominates, the resulting force is collinear with the slip vector. This gradual change in orientation of the resulting tire-force with increasing slips is a main feature of the proposed model. In Figure 27 the effect is illustrated for the three choices of sliding-friction models. In the figures the difference between the slip-vector angle β and the angle of the resulting tire-force β_F is shown. This difference is always zero for pure-slips ($\beta = 0$ deg or $\beta = 90$ deg). For small combined-slips when the tire-stiffness determines the orientation of the resulting tire-force this difference is as largest. For larger slips the difference goes to zero for the collinear model. For the slip-projection model and the MDR model this difference approaches zero more slowly with increasing slips.

The velocity dependence is illustrated in Figures 28 and 29. The pure-slip Magic Formula model is calibrated with data from tire measurements with wheel velocity v_0.[4] Tire-forces are shown for wheel velocities v which are 1–4 times the pure-slip model velocity v_0. The results agree qualitatively well with what is

[4]The exact velocity v_0 is not known for the empiral pure-slip data, but measurements on the used test-bed are normally performed around 10 m/s.

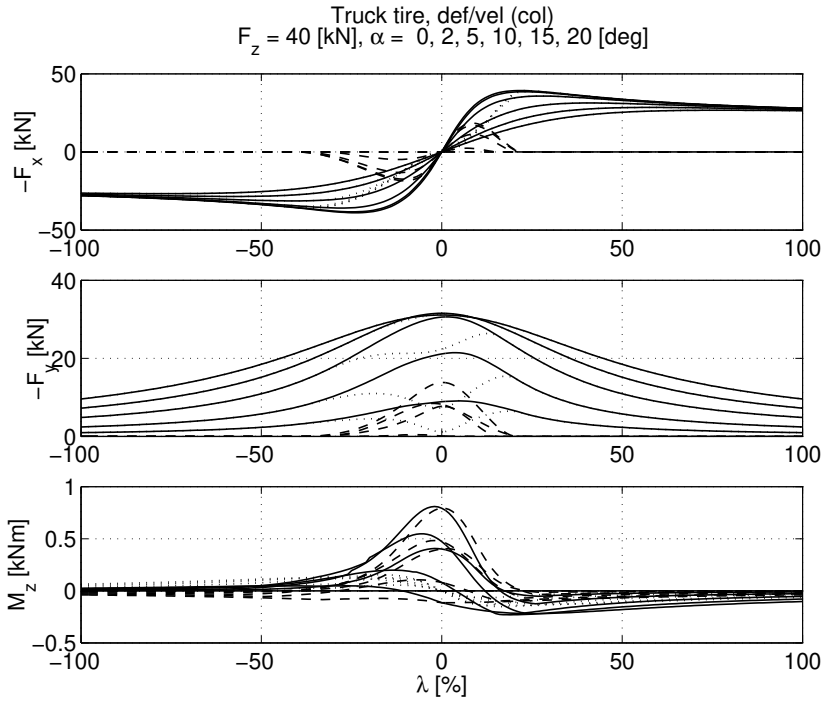

Figure 24 Combined-slip forces with the deformation-invariant adhesion-force model (Property 5) in combination with the collinear slip-velocity invariant sliding-force model (Property 11) for fixed slip angles α and varying λ ranging from -100% (driving) to 100% (braking with locked wheels). Top: F_x (solid), F_{ax} (dotted), F_{sx} (dashed). Middle: F_y (solid), F_{ay} (dotted), F_{sy} (dashed). Bottom: M_z (solid), M_z' (dashed), M_z'' (dotted).

reported in e.g. [24]. The slip-velocity at a certain combined slip (λ, α) is $v_s = v\left((\lambda\cos(\alpha))^2 + \sin^2(\alpha)\right)^{1/2}$. Corresponding pure-slips for the empirical pure-slip model are given by $v_s = \lambda_0^{\text{vel}} v_0$ and $v_s = \sin(\alpha_0^{\text{vel}}) v_0$. From these expressions pure-slips $\lambda_0^{\text{vel}} < 100\%$ and $\alpha_0^{\text{vel}} < 90$ deg can be solved for when $(\lambda\cos(\alpha))^2 + \sin^2(\alpha) \leq (v/v_0)^2$, see Equations (155). If $(\lambda\cos(\alpha))^2 + \sin^2(\alpha) > (v/v_0)^2$ then extrapolations of the pure-slip models are necessary.

Normal-force dependence is straightforwardly included in the proposed models by using normal-force dependent pure-slip models such as the standard Magic Formula.

5.4 Relations to Other Models

In Figure 30 the responses of the proposed model, the Bakker model [2], and the COMBINATOR model [28] are shown for comparison. It is clear that the proposed model performs better than the COMBINATOR model at small slip-angles α. The COMBINATOR model may be written as:

$$F_x = F\cos(\beta) \qquad \text{and} \qquad F_y = F\sin(\beta) \tag{110a}$$

where

$$F = F_{x0}(s)\cos^2(\beta) + F_{y0}(s)\sin^2(\beta) \tag{110b}$$

The resulting force is always collinear with the slip vector. In the COMBINATOR model the lateral force initially increases as a longitudinal slip λ is applied. This is a result of the assumption of a collinear combined-slip tire-force in the full slip-range, in combination with the use of the combined-slip magnitude in the empirical pure-slip models.

It is clear from the figure that the proposed region-invariant model is very similar to the Bakker model. One major reason for this is that also the Bakker

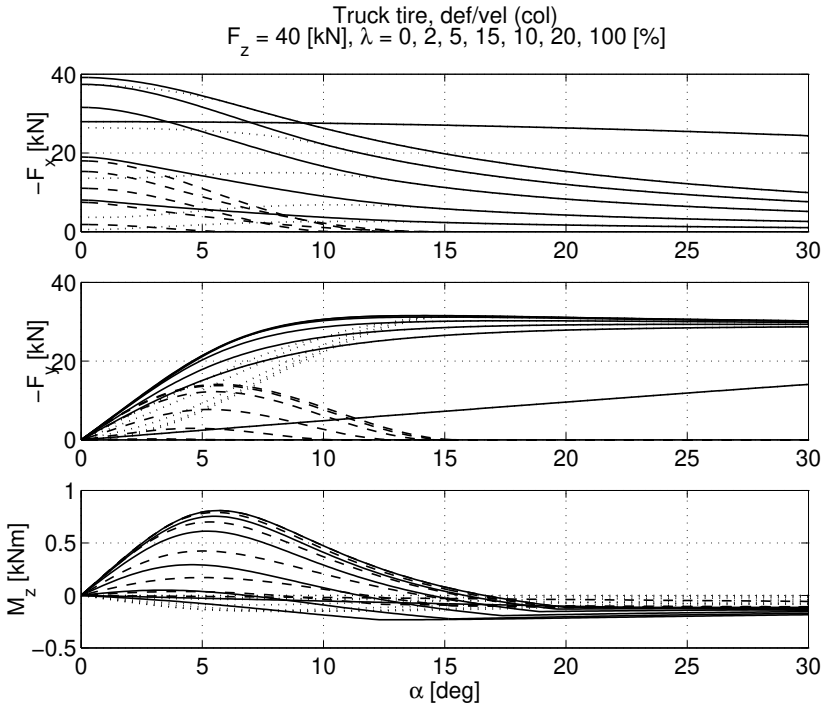

Figure 25 Combined-slip forces with the deformation-invariant adhesion-force model (Property 5) in combination with the collinear slip-velocity invariant sliding-force model (Property 11) for fixed λ as α is swept from 0 to 30 deg. Top: F_x (solid), F_{ax} (dotted), F_{sx} (dashed). Middle: F_y (solid), F_{ay} (dotted), F_{sy} (dashed). Bottom: M_z (solid), M'_z (dashed), M''_z (dotted).

model is based on the pure slips σ_{0x}^{reg}, σ_{0y}^{reg}. The Bakker equations:

$$F_x = \cos\left((1-\vartheta)\beta^\circ + \vartheta\beta\right) F'_{0x} \tag{111a}$$

$$F_y = \sin\left((1-\vartheta)\beta^\circ + \vartheta\beta\right) F'_{0y} \tag{111b}$$

where

$$\vartheta \triangleq \frac{2}{\pi}\arctan(q_1\psi^2(\sigma_x,\sigma_y))), \tag{112}$$

with q_1 as a parameter and

$$F'_{0x} \triangleq F_{0x}(\sigma_{0x}^{\text{reg}}) - \text{sat}(\psi)(F_{0x}(\sigma_{0x}^{\text{reg}}) - F_{0y}(\sigma_{0y}^{\text{reg}}))\sin^2(\beta^\circ) \tag{113a}$$

$$F'_{0y} \triangleq F_{0y}(\sigma_{0y}^{\text{reg}}) + \text{sat}(\psi)(F_{0x}(\sigma_{0x}^{\text{reg}}) - F_{0y}(\sigma_{0y}^{\text{reg}}))\cos^2(\beta^\circ) \tag{113b}$$

are clearly similar to the collinear region-invariant model:

$$F_x = \left((1-\theta_x)\cos(\beta^\circ) + \theta_x\cos(\beta^-)\right) F_{0x} \tag{114a}$$

$$F_y = \left((1-\theta_y)\sin(\beta^\circ) + \theta_y\sin(\beta^-)\right) F_{0y} \tag{114b}$$

with θ given by (70). In the Bakker model the orientation of the resultant force is obtained by a convex combination of angles corresponding to adhesion and sliding respectively. In the region-invariant model the resultant is obtained by a convex combination of adhesive and sliding forces. The resultant friction magnitude for the Bakker model at full sliding is

$$F = F_{0x}\sin^2(\beta^\circ) + F_{0y}\cos^2(\beta^\circ) \tag{115}$$

For the region-invariant model the corresponding magnitude is

$$F_{0x}F_{0y}/\sqrt{F_{0x}\sin^2(\beta^\circ) + F_{0y}\cos^2(\beta^\circ)} \tag{116}$$

Compare with the COMBINATOR magnitude above.

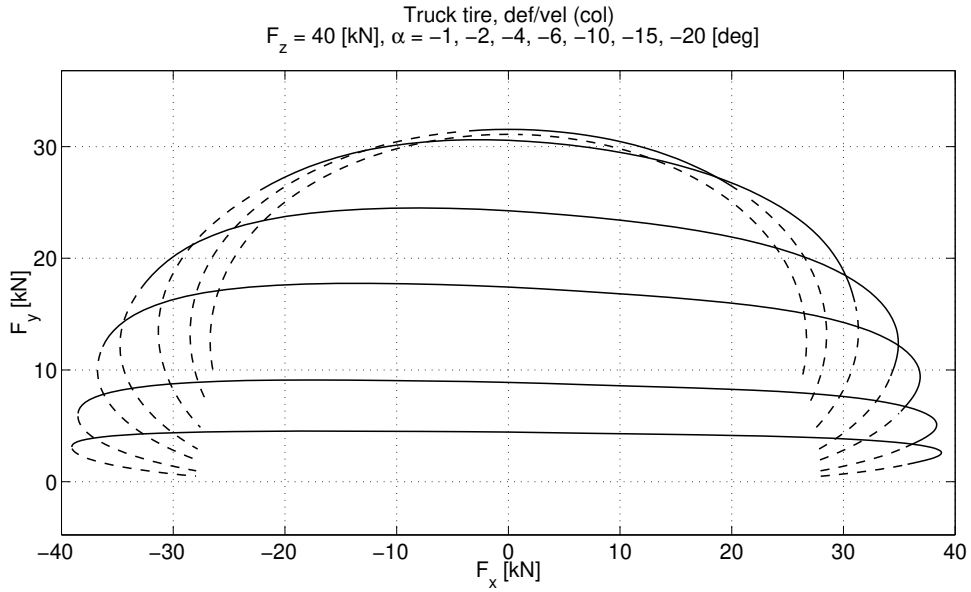

Figure 26 Combined-slip forces with the deformation-invariant adhesion-force model (Property 5) in combination with the collinear slip-velocity invariant sliding-force model (Property 11) for fixed slip angles α and varying λ ranging from -100% (driving) to 100% (braking with locked wheels).

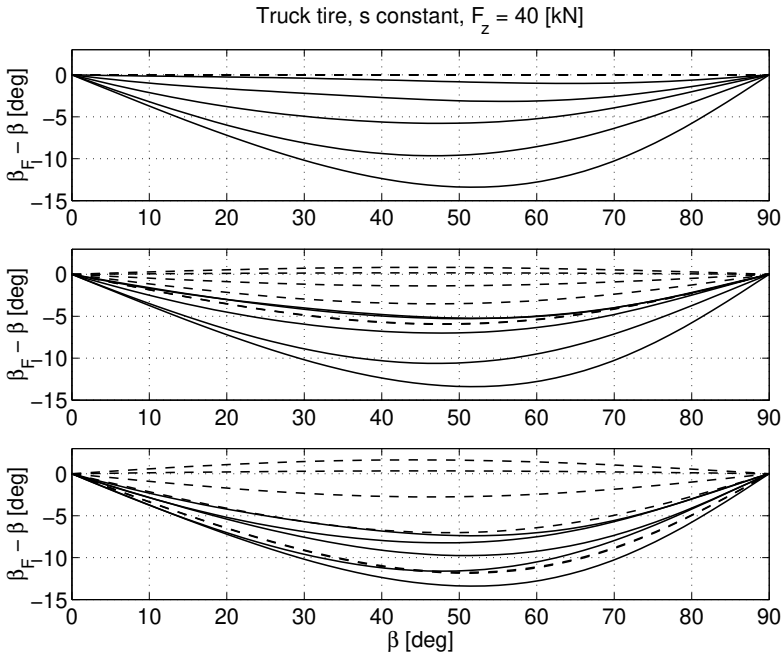

Figure 27 The difference between the slip-vector angle β and the angle of the resulting tire-force β_F for the deformation-invariant adhesion-force model (Property 5) in combination with the collinear (top), slip-projection (middle), and MDR (bottom) slip-velocity invariant sliding-force model (Property 11). (Partial sliding (solid); Full sliding (dashed))

6. Summary

This work proposes two new models for combined-slip tire-forces and self-aligning moment. Prerequisites of the new models are to use available empirical models for pure-slip forces and to not introduce any additional parameters which need calibration with combined-slip data. The proposed models are based on understanding of the physical sources of tire-forces as given by the theoretical rigid-

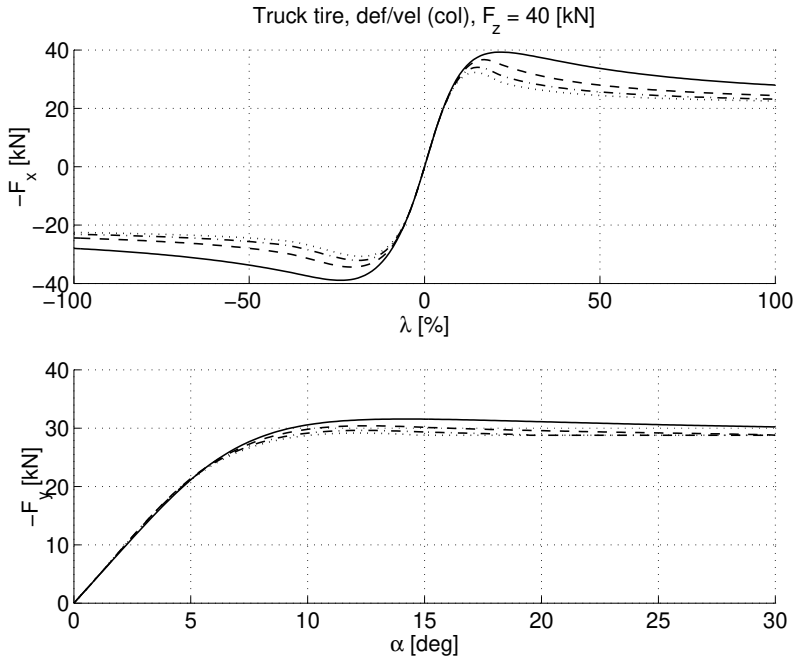

Figure 28 Velocity dependence at pure-slips for the deformation-invariant adhesion-force model (Property 5) in combination with the collinear slip-velocity invariant sliding-force model (Property 11). Velocities: $v = v_0$ (solid), $2v_0$ (dashed), $3v_0$ (dash-dotted), $4v_0$ (dotted).

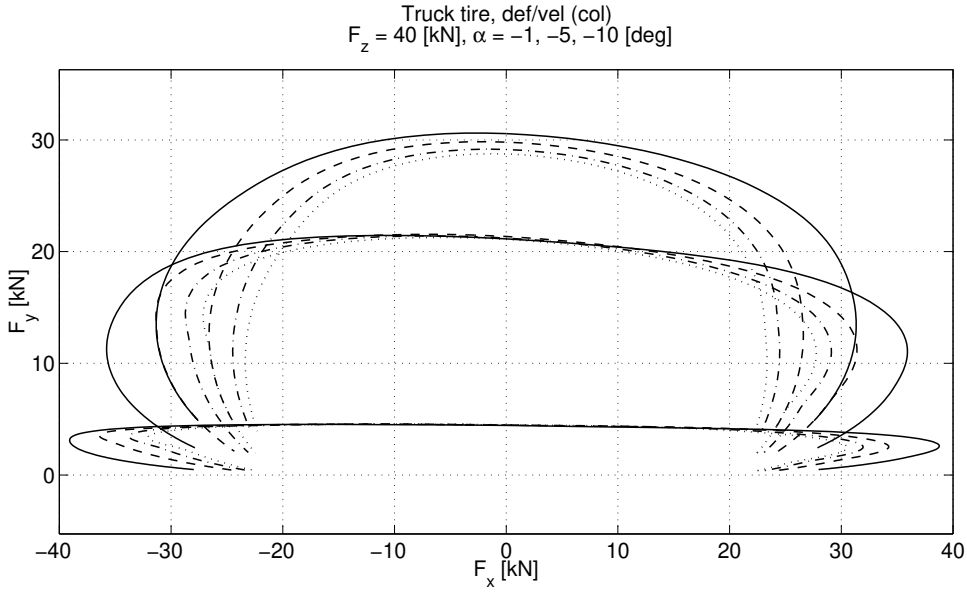

Figure 29 Velocity dependence at pure-slips for the deformation-invariant adhesion-force model (Property 5) in combination with the collinear slip-velocity invariant sliding-force model (Property 11). Velocities: $v = v_0$ (solid), $2v_0$ (dashed), $3v_0$ (dash-dotted), $4v_0$ (dotted).

carcasss brush-model. Based on the brush-model, the combined-slip forces may be described with a scaling of corresponding pure-slip forces. In the combined-slip models the resulting forces are computed by multiplying empirical pure-slip forces with theoretically derived scaling factors. All model expressions are computationally feasible. The proposed models fulfill the criteria listed in the introduction.

The combined-slip models are based on a method to separate the adhesion and slide forces in the empirical pure-slip models. Combined-slip forces for adhesion and sliding are then also constructed separately. This makes sense since

adhesion and slide forces are the result of different physical processes. Therefore, the pure-slips corresponding to a particular combined slip are chosen differently for adhesive and sliding forces. For adhesion forces the pure-slips which describe the same tread-deformation as the combined slip are used. For sliding forces the pure-slips which result in the same slip-velocity as the combined slip are used. Models based on pure-slips which correspond to the same size of adhesive and sliding regions in the contact patch are also suggested. These seem less physically motivated, but result in simpler expressions.

The brush-model includes the major physical processes which are responsible for the build-up of tire-forces. Additional effects resulting from e.g. a flexible carcass are implicitly included in the combined-slip models if they are present in the used pure-slip models. The choice of corresponding pure-slips affects how such additional effects influence the combined-slip forces.

Four parameters with clear physical interpretations are introduced in the proposed models. Two of these parameters are of central significance and can be computed automatically from the pure-slip models. The other two are set to unity as default and describe a freedom to adjust the model-response if desired.

The Magic Formula is a natural choice of pure-slip empirical model, and is used in the examples. Both suggested combined-slip models give good results in validation with empirical data. The relations to similar previous combined-slip models are analyzed. It is concluded that the suggested models are superior to the previously published COMBINATOR model. The combined-slip model presented together with the Magic Formula includes similar effects as the proposed models, but with a different approach.

Preliminary studies on extension of the models to include effects of a flexible carcass are ongoing. The ultimate goal is to include simple models of dynamic effects and transient behaviour resulting from carcass defomation. It is believed that this is possible without introducing overwhelming complexity. Effects of plysteer, conicity, and camber have not been regarded to this point. It is expected that also these may be included in the models.

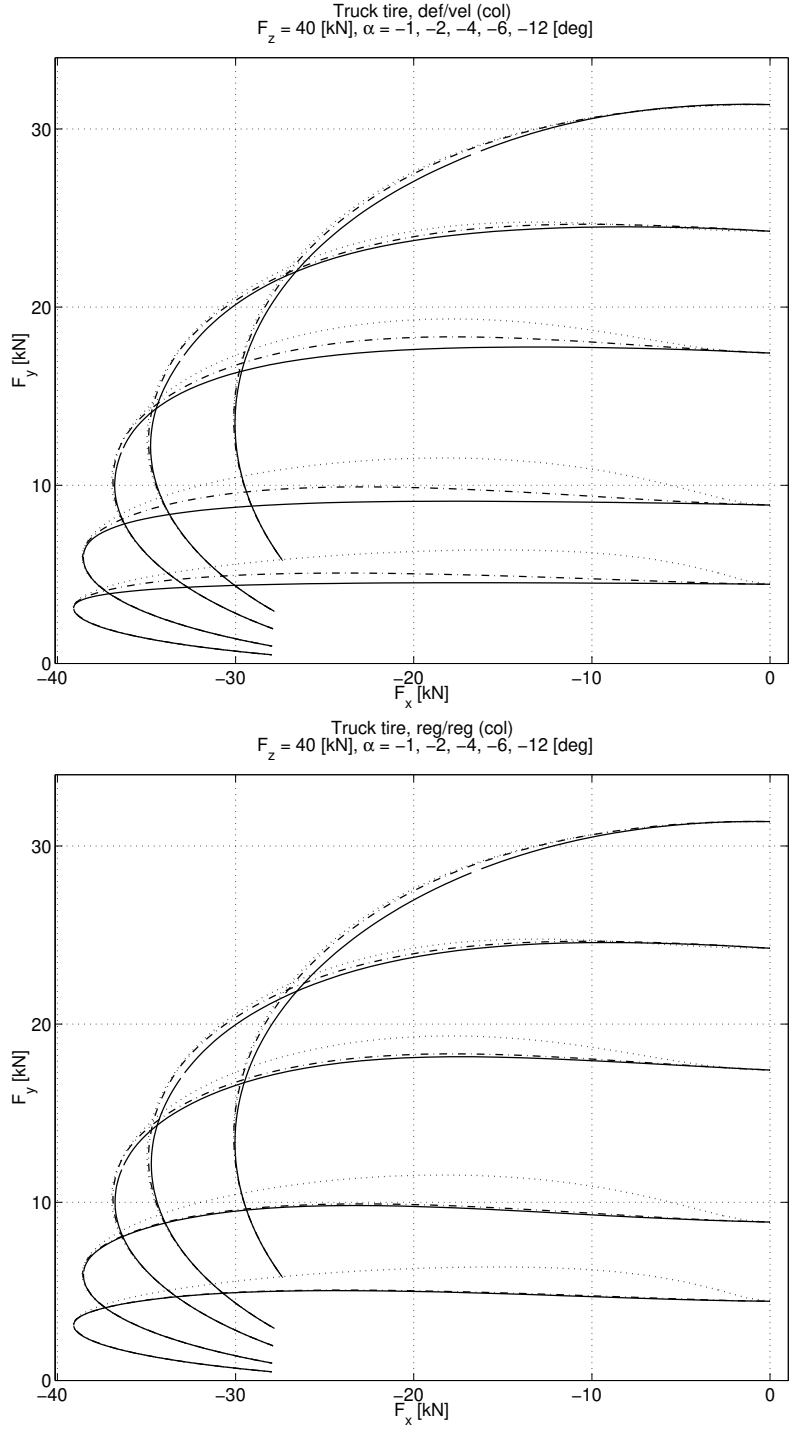

Figure 30 Combined-slip forces with the deformation-invariant adhesion-force model (Property 5) in combination with the collinear slip-velocity invariant sliding-force model (Property 11) (upper plot, solid line) and the region-invariant adhesion-force model (Property 8) in combination with the collinear region-invariant sliding-force model (Property 9) (lower plot, solid line) for fixed slip angles α and varying λ ranging from 0% to 100% (braking with locked wheels). The COMBINATOR model (dotted line) and the Bakker model (dash-dotted line) are shown for comparison.

7. References

[1] E. Bakker, L. Nyborg, and H. B. Pacejka. Tyre modelling for use in vehicle dynamics studies. SAE Techical Paper 870421, 1987.

[2] E. Bakker, H. B. Pacejka, and L. Lidner. A new tire model with an application in vehicle dynamics studies. SAE Technical Paper 890087, 1989.

[3] H. Bauer, editor. *Automotive Handbook*. Robert Bosch GmbH, 1996.

[4] P. Bayle, J. F. Forissier, and S. Lafon. A new tire model for vehicle dynamics simulations. *Automotive Technology International*, pages 193–198, 1993.

[5] P.-A. Bliman, T. Bonald, and M. Sorine. Hysteresis operators and tyre friction models. application to vehicle dynamic simulation. In *Proceedings of ICIAM 95, Hamburg, Germany*, 1995.

[6] F. Böhm and H.-P. Willumeit, editors. *Tyre Models for Vehicle Dynamics Analysis*. Swets & Zeitlinger Publishers, 1996. Supplement to Vehicle System Dynamics Volume 27.

[7] R. M. Brach and R. M. Brach. Modeling combined braking and steering tire forces. SAE Technical Paper 2000-01-0357, 2000.

[8] Carlos Canudas De Wit and Panagiotis Tsiotras. Dynamic tire friction model for vehicle traction control. In *Proceedings of the 1998 American Control Conference*, Philadelphia, 1998.

[9] Joško Deur. A brush-type dynamic tire friction model for non-uniform normal pressure distribution. In *Proceedings of the 15th Triennial IFAC World Congress*, Barcelona, Spain, 2002.

[10] S. Edlund. Tyre models: Subreport -91. Technical report, Volvo Truck Corporation, 1991. Confidential.

[11] J. R. Ellis. *Vehicle Handling Dynamics*. Mechanical Engineering Publications Limited, London, 1994.

[12] G. Gim and P. E. Nikravesh. An analytical model of pneumatic tyres for vehicle dynamics simulations. part 1: Pure slips. *International Journal of Vehicle Design*, 11(6):589–618, 1990.

[13] G. Gim and P. E. Nikravesh. An analytical model of pneumatic tyres for vehicle dynamics simulations. part 2: Comprehensive slips. *International Journal of Vehicle Design*, 12(1):19–39, 1991.

[14] G. Gim and P. E. Nikravesh. An analytical model of pneumatic tyres for vehicle dynamics simulations. part 3: Validation against experimental data. *International Journal of Vehicle Design*, 12(2):217–228, 1991.

[15] S. Goyal. *Planar Sliding Of A Rigid Body With Dry Friction: Limit Surfaces And Dynamics Of Motion*. PhD thesis, Cornell University, Department Of Mechanical Engineering, 1989.

[16] P. Holdmann, P. Köhn, and J. Holtschulze. Dynamic tyre properties under combined slip situations in test and simulation. In *EAEC Barcelona 1999, European Automotive Congress*, pages 817–822, 1999.

[17] ISO 8855. Road vehicles — vehicle dynamics and road-holding ability — vocabulary, 1991.

[18] U. Kiencke and L. Nielsen. *Automotive Control Systems: For Engine, Driveline, and Vehicle*. Springer-Verlag, 2000.

[19] P. K. Nguyen and E. R. Case. Tire friction models and their effect on simulated vehicle dynamics. In *Proceedings of a Symposium on Commercial Vehicle Braking and Handling*, number UM-HSRI-PF-75-6, pages 245–312, 1975.

[20] V. T. Nicholas and T.R Comstock. Predicting directional behavior of tractor semitrailers when wheel anti-skid brake systems are used. In *ASME Winter Annual Meeting*, number Paper No. 72–WA/Aut-16, November 26–30 1972.

[21] L. Nielsen and L. Eriksson. Course material vehicular systems. Linköping Institute of Technology, Vehicular Systems, ISY, 1999.

[22] O. Nordström. The vti flat bed tire test facility - a new tool for testing commercial tire characteristics. SAE Techical Paper 933006, 1993.

[23] H. B. Pacejka. Modelling of the pneumatic tyre and its impact on vehicle dynamic behavior. Technical Report i72B, Technische Universiteit Delft, 1988.

[24] H. B. Pacejka. *Tyre and Vehicle Dynamics*. Butterworth-Heinemann, 2002.

[25] M. G. Pottinger, J. E. McIntyre, A. J. Kempainen, and W. Pelz. Truck tire force and moment in cornering - braking - driving on ice, snow, and dry surface. SAE Techical Paper 933006, 1993.

[26] M. G. Pottinger, W. Pelz, and G. Falciola. Effectiveness of the slip circle: "COMBINATOR", model for combine tire cornering and braking forces when applied to a range of tires. SAE Techical Paper 982747, 1998.

[27] SAE Recommended Practice J670e. Vehicle dynamics terminology, 1976.

[28] Dietrich J. Schuring, Wolfgang Pelz, and Marion G. Pottinger. A model for combined tire cornering and braking forces. In *Investigations and Analysis in Vehicle Dynamics and Simulation*, pages 61–83. SAE International, 1996. SAE Technical Paper 960180.

[29] A. van Zanten, W. D. Ruf, and A. Lutz. Measurement and simulation of transient tire forces. SAE Techical Paper 890640, 1989.

[30] J. Y. Wong. *Theory of Ground Vehicles*. John Wiley & Sons, 3 edition, 2001.

A. Proofs

A.1 Proof of Propery 3

Proof. Direct insertion of (36) and (48) in (67) gives

$$\begin{aligned}\theta_x(\sigma_x) &= \frac{\mu_{sx} F_z \psi^2(\sigma_x,0)\,(3-2\psi(\sigma_x,0))}{2a^2 c_{px(\sigma_x)}\sigma_x\,(1-\psi(\sigma_x,0))^2 + \mu_{sx} F_z \psi^2(\sigma_x,0)\,(3-2\psi(\sigma_x,0))} \\ &= \frac{\psi(\sigma_x,0)\,(3-2\psi(\sigma_x,0))}{3\rho_x\,(1-\psi(\sigma_x,0))^2 + \psi(\sigma_x,0)\,(3-2\psi(\sigma_x,0))} \end{aligned} \quad (117)$$

where (32) is used in the last equality. At full sliding ($\sigma_x \geq \sigma_x^\circ$) then $F_{0ax}(\sigma_x) = 0$, $F_{0sx}(\sigma_x) = F_{0x}(\sigma_x)$ and hence $\theta_x(\sigma_x) = 1$ from the definition. The expressions for $\theta_y(\sigma_y)$, $1-\theta_x(\sigma_x)$, and $1-\theta_y(\sigma_y)$ are derived analogously. □

A.2 Proof of Property 4

Proof. Follows directly from (23), which expresses that the deformations in the longitudinal and lateral directions are independent. □

A.3 Proof of Property 5

Proof. Assume $\sigma_x \neq 0$, then $F_{0ax}(\sigma_x) \neq 0$ since $\psi(\sigma_x,\sigma_y) < 1$, and

$$\begin{aligned} F_{ax}(\sigma_x,\sigma_y) = F_{0ax}(\sigma_x)\frac{F_{ax}(\sigma_x,\sigma_y)}{F_{0ax}(\sigma_x)} &= F_{0ax}(\sigma_x)\left(\frac{1-\psi(\sigma_x,\sigma_y)}{1-\psi(\sigma_x,0)}\right)^2 \\ &= (1-\theta_x(\sigma_x))\,F_{0x}(\sigma_x)\left(\frac{1-\psi(\sigma_x,\sigma_y)}{1-\psi(\sigma_x,0)}\right)^2 \end{aligned} \quad (118)$$

The second equality is due to (36) and (37). Inserting (70) and rearranging yields (74). The scaling factor is non-singular at $\sigma_x = 0$. If $\sigma_x = 0$ then $F_{0ax}(\sigma_x) = F_{ax}(\sigma_x, \sigma_y) = 0$, which is fulfilled by (74). The lateral expression is derived analogously. □

A.4 Proof of Property 6

Proof. Regard the longitudinal force and assume $\sigma_x \neq 0$, $\sigma_y \neq 10$, $\psi(\sigma_x, \sigma_y) < 1$, then from (48), (51) and (49)

$$\begin{aligned} F_{sx}(\sigma_x, \sigma_y) &= F_{0sx}(\sigma_x)\frac{F_{sx}(\sigma_x, \sigma_y)}{F_{0sx}(\sigma_x)} = F_{0sx}(\sigma_x)\frac{F_{sz}(\sigma_x, \sigma_y)}{F_{sz}(\sigma_x, 0)}\cos(\beta) \\ &= \theta_x(\sigma_x)F_{0x}(\sigma_x)\frac{\psi^2(\sigma_x, \sigma_y)\,(3 - 2\psi(\sigma_x, \sigma_y))}{\psi_x^2(\sigma_x)(3 - 2\psi(\sigma_x, 0))}\cos(\beta) \end{aligned} \tag{119}$$

For small slips σ_x then $\psi(\sigma_x, 0)$ approaches zero and computing the expression will result in numerical problems. Rewriting is therefore necessary. Insertion of (70) and using that $\psi(\sigma_x, 0)/\psi(\sigma_x, \sigma_y) = \cos(\beta^\circ)$ yields, after rearrangements

$$F_{sx}(\sigma_x, \sigma_y) = F_{0x}(\sigma_x)\frac{\psi(\sigma_x, \sigma_y)\,(3 - 2\psi(\sigma_x, \sigma_y))}{3\rho_x\,(1 - \psi(\sigma_x, 0))^2 + \psi(\sigma_x, 0)\,(3 - 2\psi(\sigma_x, 0))} \cdot \frac{\cos(\beta)}{\cos(\beta^\circ)} \tag{120}$$

Using the definitions of β and β° it is easily verified, see Appendix C, that

$$\frac{\cos(\beta)}{\cos(\beta^\circ)} = \sigma_x^\circ\left(\frac{1}{\sigma_x^\circ}\cos(\beta)\cos(\beta^\circ) + \frac{1}{\sigma_y^\circ}\sin(\beta)\sin(\beta^\circ)\right) \tag{121}$$

Insertion of this in (120) completes the proof for $\psi(\sigma_x, \sigma_y) < 1$. For $\psi(\sigma_x, \sigma_y) \geq 1$ but $\psi(\sigma_x, 0) < 1$ then

$$\begin{aligned} F_{sx}(\sigma_x, \sigma_y) &= F_{0sx}(\sigma_x)\frac{F_{sx}(\sigma_x, \sigma_y)}{F_{0sx}(\sigma_x)} = F_{0sx}(\sigma_x)\frac{F_z}{F_{sz}(\sigma_x, 0)}\cos(\beta) \\ &= \theta_x(\sigma_x)F_{0x}(\sigma_x)\frac{1}{\psi_x^2(\sigma_x)(3 - 2\psi(\sigma_x, 0))}\cos(\beta) \\ &= F_{0x}(\sigma_x)\frac{1}{3\rho_x\,(1 - \psi(\sigma_x, 0))^2 + \psi(\sigma_x, 0)\,(3 - 2\psi(\sigma_x, 0))} \cdot \frac{\cos(\beta)}{\psi(\sigma_x, 0)} \end{aligned} \tag{122}$$

Observing that $\cos(\beta)/\psi(\sigma_x, 0) = \sigma_x^\circ/\sqrt{\sigma_x^2 + \sigma_y^2}$ completes the proof for this case. For $\psi(\sigma_x, \sigma_y) \geq 1$ and $\psi(\sigma_x, 0) \geq 1$ then

$$F_{sx}(\sigma_x, \sigma_y) = F_{0sx}(\sigma_x)\frac{F_{sx}(\sigma_x, \sigma_y)}{F_{0sx}(\sigma_x)} = \theta_x(\sigma_x)F_{0x}(\sigma_x)\frac{F_z\mu_{sx}\cos(\beta)}{F_z\mu_{sx}} = F_{0x}(\sigma_x)\cos(\beta) \tag{123}$$

The lateral expression is derived analogously. □

A.5 Proof of Property 7

Proof. The pure slips σ_{0x}^{reg} and σ_{0y}^{reg} result in the same normalized slip as the combined slip (σ_x, σ_y)

$$\psi_x(\sigma_{0x}^{\text{reg}}) = \psi(\sigma_{0x}^{\text{reg}}, 0) = \psi(\sigma_x, \sigma_y) \tag{124a}$$

$$\psi_y(\sigma_{0y}^{\text{reg}}) = \psi(0, \sigma_{0y}^{\text{reg}}) = \psi(\sigma_x, \sigma_y) \tag{124b}$$

This follows directly by inserting (77) in (33). From (124) and (35) it then follows that the pure slips σ_{0x}^{reg} and σ_{0y}^{reg} result in adhesive regions of the same size as the combined slip (σ_x, σ_y)

$$x_s(\sigma_{0x}^{\text{reg}}, 0) = x_s(0, \sigma_{0y}^{\text{reg}}) = x_s(\sigma_x, \sigma_y) \tag{125}$$

□

A.6 Proof of Property 8

Proof. Assume $\sigma_x \neq 0$ and $\psi(\sigma_x, \sigma_y) < 1$, then

$$\begin{aligned} F_{ax}(\sigma_x, \sigma_y) &= F_{0ax}(\sigma_{0x}^{\text{reg}}) \frac{F_{ax}(\sigma_x, \sigma_y)}{F_{0ax}(\sigma_{0x}^{\text{reg}})} = F_{0ax}(\sigma_{0x}^{\text{reg}}) \frac{\sigma_x \left(1 - \psi(\sigma_x, \sigma_y)\right)}{\sigma_{0x}^{\text{reg}} \left(1 - \psi(\sigma_{0x}^{\text{reg}}, 0)\right)} \\ &= F_{0ax}(\sigma_{0x}^{\text{reg}}) \frac{\sigma_x \left(1 - \psi(\sigma_x, \sigma_y)\right)}{\sigma_x^{\circ} \psi(\sigma_x, \sigma_y) \left(1 - \psi(\sigma_x, \sigma_y)\right)} = F_{0ax}(\sigma_{0x}^{\text{reg}}) \frac{\psi(\sigma_x, 0)}{\psi(\sigma_x, \sigma_y)} \\ &= (1 - \theta_x(\sigma_{0x}^{\text{reg}})) F_{0x}(\sigma_{0x}^{\text{reg}}) \cos(\beta^{\circ}) \end{aligned} \tag{126}$$

If $\sigma_x = 0$ then $F_{0ax}(\sigma_x) = F_{ax}(\sigma_x, \sigma_y) = 0$ which is fulfilled by (78) since then $\sin(\beta_{\circ}) = 0$. The lateral expression is derived analogously. □

A.7 Proof of Property 9

Proof. Regard the longitudinal force. Then using (51), (49), (77), (48)

$$\begin{aligned} F_{sx}(\sigma_x, \sigma_y) &= -cos(\beta) \mu_{sx} F_{sz}(\sigma_x, \sigma_y) = -cos(\beta) \mu_{sx} F_{sz}(\sigma_{0x}^{\text{reg}}, 0) \\ &= F_{0sx}(\sigma_{0x}^{\text{reg}}) \cos(\beta) = (1 - \theta_x(\sigma_x)) F_{0x}(\sigma_{0x}^{\text{reg}}) \cos(\beta) \end{aligned} \tag{127a}$$

The lateral expression is derived analogously. □

A.8 Proof of Property 10

Proof. The relative velocity v_s at the combined slip (σ_x, σ_y) and the vehicle velocity v is given by

$$v_s = \sqrt{v_{sx}^2 + v_{sy}^2} = \frac{v \sqrt{\sigma_x^2 + \sigma_y^2}}{\sqrt{(1 + \sigma_x)^2 + \sigma_y^2}} \tag{128}$$

For the pure longitudinal slip at $v_{0x} = v_0$ with $v_{0sx} = v_s \operatorname{sgn}(\sigma_x)$ the slip definition gives

$$\sigma_{0x}^{\text{vel}} = \frac{v_{0sx}}{v_{0x} - v_{0sx}} = \frac{v_s \operatorname{sgn}(\sigma_x)}{v_0 - v_s \operatorname{sgn}(\sigma_x)} = \frac{\sqrt{\sigma_x^2 + \sigma_y^2} \operatorname{sgn}(\sigma_x)}{\frac{v_0}{v} \sqrt{(1 + \sigma_x)^2 + \sigma_y^2} - \sqrt{\sigma_x^2 + \sigma_y^2} \operatorname{sgn}(\sigma_x)} \tag{129}$$

and for the lateral case with $v_{0sy} = v_s \operatorname{sgn}(\sigma_y)$, $v_{0x} = \sqrt{v_0^2 - v_{0sy}^2}$ and $v_{0sx} = 0$,

$$\sigma_{0y}^{\text{vel}} = \frac{v_{0sy}}{v_{0x} - v_{0sx}} = \frac{v_s \operatorname{sgn}(\sigma_y)}{\sqrt{v_{0x}^2 - v_{0sy}^2}} = \frac{\sqrt{\sigma_x^2 + \sigma_y^2} \operatorname{sgn}(\sigma_y)}{\sqrt{\left(\frac{v_0}{v}\right)^2 \left((1 + \sigma_x)^2 + \sigma_y^2\right) - \left(\sigma_x^2 + \sigma_y^2\right)}} \tag{130}$$

□

A.9 Proof of Property 11

Proof. Regard the longitudinal force and assume $\sigma_x \neq 0$. Then using (51), (49), and (48)

$$\begin{aligned} F_{sx}(\sigma_x, \sigma_y) &= F_{0sx}(\sigma_{0x}^{\text{vel}}) \frac{F_{sx}(\sigma_x, \sigma_y)}{F_{0sx}(\sigma_{0x}^{\text{vel}})} = -cos(\beta) F_{0sx}(\sigma_{0x}^{\text{vel}}) \frac{F_{sz}(\sigma_x, \sigma_y)}{F_{sz}(\sigma_{0x}^{\text{vel}}, 0)} \operatorname{sgn}(\sigma_x) \\ &= |\cos(\beta)| \theta_x(\sigma_{0x}^{\text{vel}}) F_{0x}(\sigma_{0x}^{\text{vel}}) \frac{F_{sz}(\sigma_x, \sigma_y)}{F_{sz}(\sigma_{0x}^{\text{vel}}, 0)} = |\cos(\beta)| F_{0x}(\sigma_{0x}^{\text{vel}}) \theta_x(\sigma_{0x}^{\text{vel}}) \Gamma_x^{\text{vel}} \end{aligned} \tag{131a}$$

Assume that $\psi(\sigma_x,\sigma_y)<1$ and $\psi(\sigma_{0x}^{\mathrm{vel}},0)<1$. Then Equation (49) gives

$$\Gamma_x^{\mathrm{vel}}=\frac{F_{sz}(\sigma_x,\sigma_y)}{F_{sz}(\sigma_{0x}^{\mathrm{vel}},0)}=\frac{\psi^2(\sigma_x,\sigma_y)(3-2\psi(\sigma_x,\sigma_y))}{\psi^2(\sigma_{0x}^{\mathrm{vel}},0)(3-2\psi(\sigma_{0x}^{\mathrm{vel}},0))} \tag{132}$$

If $\psi(\sigma_x,\sigma_y)\geq 1$ then (132) holds with $\psi(\sigma_x,\sigma_y)$ replaced by unity and if $\psi(\sigma_{0x}^{\mathrm{vel}},0)\geq 1$ then (132) holds with $\psi(\sigma_{0x}^{\mathrm{vel}},0)$ replaced with unity. Rewriting is necessary to avoid singluar numerics at small slips since $\psi^2(\sigma_x^{\mathrm{vel}},0)$ is present in the denominator. When $\psi(\sigma_x,\sigma_y)<1$ and $\psi(\sigma_{0x}^{\mathrm{vel}},0)<1$ then using (33) and (80)

$$\begin{aligned}
\Gamma_x^{\mathrm{vel}} &= \left(\left(\frac{\sigma_x}{\sigma_x^\circ}\right)^2+\left(\frac{\sigma_y}{\sigma_y^0}\right)^2\right)\frac{(\sigma_x^\circ)^2\left(\frac{v_0}{v}\sqrt{(1+\sigma_x)^2+\sigma_y^2}-\operatorname{sgn}\sigma_x\sqrt{\sigma_x^2+\sigma_y^2}\right)^2}{(\sigma_x^2+\sigma_y^2)}\\
&\qquad\cdot\frac{(3-2\psi(\sigma_x,\sigma_y))}{(3-2\psi(\sigma_{0x}^{\mathrm{vel}},0))}\\
&=\frac{(3-2\psi(\sigma_x,\sigma_y))}{(3-2\psi(\sigma_{0x}^{\mathrm{vel}},0))}\left(\frac{\cos(\beta)}{\cos(\beta^\circ)}\right)^2\left(\frac{v_0}{v}\sqrt{(1+\sigma_x)^2+\sigma_y^2}-\operatorname{sgn}(\sigma_x)\sqrt{\sigma_x^2+\sigma_y^2}\right)^2\\
&=\frac{(3-2\psi(\sigma_x,\sigma_y))}{(3-2\psi(\sigma_{0x}^{\mathrm{vel}},0))}\left(\sigma_x^\circ\left(\frac{1}{\sigma_x^\circ}|\cos(\beta)|\cos(\beta^\circ)+\frac{1}{\sigma_y^\circ}|\sin(\beta)|\sin(\beta^\circ)\right)\right)^2\\
&\qquad\cdot\left(\frac{v_0}{v}\sqrt{(1+\sigma_x)^2+\sigma_y^2}-\operatorname{sgn}\sigma_x\sqrt{\sigma_x^2+\sigma_y^2}\right)^2
\end{aligned} \tag{133}$$

This expression will not render any computational problems. The rewriting of $\cos(\beta)/\cos(\beta^\circ)$ is shown in appendix C. The factor $\psi^2(\sigma_x^{\mathrm{vel}},0)$ in the denominator of (132) does not pose any problem when $\psi(\sigma_x,\sigma_y)\geq 1$. From the definition it is easy to see that $\psi(\sigma_x^{\mathrm{vel}},0)$ is not close to zero when $\psi(\sigma_x,\sigma_y)\geq 1$. For $\sigma_x=0$, then $\cos(\beta)=0$ which give $F_{0sx}=0$. The lateral expressions are derived analogously. □

A.10 Proof of Property 12

Proof. The slip velocity $\bar{v}_s$ at the combined slip (σ_x,σ_y) and the vehicle velocity v is given by

$$v_{sx}=v\frac{\sigma_x}{\sqrt{(1+\sigma_x)^2+\sigma_y^2}} \tag{134}$$

$$v_{sy}=v\frac{\sigma_y}{\sqrt{(1+\sigma_x)^2+\sigma_y^2}} \tag{135}$$

For the pure longitudinal slip at the reference vehicle velocity v_0 then $v_{0x}=v_0$ and $v_{0sx}=v_{sx}$, hence

$$\sigma_{0x}^{\mathrm{velc}}=\frac{v_{0sx}}{v_{0x}-v_{0sx}}=\frac{v_{sx}}{v_0-v_{sx}}=\frac{\sigma_x}{\frac{v_0}{v}\sqrt{(1+\sigma_x)^2+\sigma_y^2}-\sigma_x} \tag{136}$$

and for the lateral case, $v_{0sy}=v_{sy}$, $v_{0sx}=0$ and $v_{0x}=\sqrt{v_0^2-v_{sy}^2}$,

$$\sigma_{0y}^{\mathrm{velc}}=\frac{v_{0sy}}{v_{0x}-v_{0sx}}=\frac{v_{sy}}{\sqrt{v_0^2-v_{sy}^2}}=\frac{v\sigma_y}{\sqrt{v_0^2\left((1+\sigma_x)^2+\sigma_y^2\right)-v^2\sigma_y^2}} \tag{137}$$

□

A.11 Proof of Property 13

Proof. Regard the longitudinal force and assume $\sigma_x \neq 0$. Then using (51), (49), (77), (48)

$$\begin{aligned}
F_{sx}(\sigma_x,\sigma_y) &= F_{0sx}(\sigma_{0x}^{\text{velc}})\frac{F_{sx}(\sigma_x,\sigma_y)}{F_{0sx}(\sigma_{0x}^{\text{velc}})} = \cos(\beta)\frac{F_{0sx}(\sigma_{0x}^{\text{velc}})}{F_{sz}(\sigma_{0x}^{\text{velc}},0)}F_{sz}(\sigma_x,\sigma_y)\,\text{sgn}(\sigma_x) \\
&= |\cos(\beta)|\theta_x(\sigma_{0x}^{\text{velc}})F_{0x}(\sigma_{0x}^{\text{velc}})\frac{F_{sz}(\sigma_x,\sigma_y)}{F_{sz}(\sigma_{0x}^{\text{velc}},0)} \\
&= F_{0x}(\sigma_{0x}^{\text{velc}})\frac{\psi_x(\sigma_{0x}^{\text{velc}})\left(3-2\psi_x(\sigma_{0x}^{\text{velc}})\right)}{3\rho_x\left(1-\psi_x(\sigma_{0x}^{\text{velc}})\right)^2+\psi_x(\sigma_{0x}^{\text{velc}})\left(3-2\psi_x(\sigma_{0x}^{\text{velc}})\right)}|\cos(\beta)| \\
&\quad\cdot\frac{\psi^2(\sigma_x,\sigma_y)(3-2\psi(\sigma_x,\sigma_y))}{\psi_x^2(\sigma_{0x}^{\text{velc}})(3-2\psi_x(\sigma_{0x}^{\text{velc}}))} \\
&= F_{0x}(\sigma_{0x}^{\text{velc}})\frac{\psi(\sigma_x,\sigma_y)(3-2\psi(\sigma_x,\sigma_y))}{3\rho_x\left(1-\psi_x(\sigma_{0x}^{\text{velc}})\right)^2+\psi_x(\sigma_{0x}^{\text{velc}})\left(3-2\psi_x(\sigma_{0x}^{\text{velc}})\right)} \\
&\quad\cdot\frac{\psi(\sigma_x,\sigma_y)}{\psi_x(\sigma_{0x}^{\text{velc}})}|\cos(\beta)| \qquad (138)
\end{aligned}$$

The expression above is only valid when $\psi(\sigma_x,\sigma_y)$ and $\psi(\sigma_{0x}^{\text{velc}},0)$ is less than 1. For the case that $\psi(\sigma_x,\sigma_y) \geq 1$, $\psi(\sigma_x,\sigma_y)$ is exchanged for 1 in (A.11) and if $\psi(\sigma_{0x}^{\text{velc}},0) \geq 1$, $\psi(\sigma_{0x}^{\text{velc}},0) = 1$ is used. Since the expression when $\psi(\sigma_{0x}^{\text{velc}},0) < 1$ includes $\psi(\sigma_{0x}^{\text{velc}},0)$ in the denominator, special care must be taken when this factor goes to zero. When $\psi(\sigma_x,\sigma_y) < 1$ we have for the latter part of (A.11)

$$\begin{aligned}
\frac{\psi(\sigma_x,\sigma_y)}{\psi_x(\sigma_{0x}^{\text{velc}})}|\cos(\beta)| &= |\cos(\beta)|\sqrt{\left(\frac{\sigma_x}{\sigma_x^\circ}\right)^2+\left(\frac{\sigma_y}{\sigma_y^0}\right)^2}\frac{\sigma_x^\circ\left(\frac{v_0}{v}\sqrt{(1+\sigma_x)^2+\sigma_y^2}-\sigma_x\right)}{\sigma_x} \\
&= \frac{|\cos(\beta)|}{\cos(\beta^\circ)}\left(\frac{v_0}{v}\sqrt{(1+\sigma_x)^2+\sigma_y^2}-\sigma_x\right) \qquad (139)
\end{aligned}$$

which will not render any computational problems. For the case when $\psi(\sigma_x,\sigma_y) \geq 1$ the following rewriting is done

$$\frac{|\cos(\beta)|}{\psi(\sigma_{0x}^{\text{velc}},0)} = \frac{\sigma_x^\circ\left(\frac{v_0}{v}\sqrt{(1+\sigma_x)^2+\sigma_y^2}-\sigma_x\right)\sigma_x}{\sigma_x\sqrt{\sigma_x^2+\sigma_y^2}} \qquad (140)$$

where σ_x can be cancelled and it is known that $\sqrt{\sigma_x^2+\sigma_y^2}$ is not close to zero when $\psi(\sigma_x,\sigma_Y) \geq 1$. For $\sigma_x = 0$, then $\cos(\beta) = 0$ which give $F_{0sx} = 0$. The derivation for the forces in the lateral direction can be shown in the same way. □

A.12 Proof of Property 14

Proof. From (65a) and 7 it is clear that the adhesive and sliding pneumatic trails for the combined slip (σ_x,σ_y) is equal to the pneumatic trails for the pure slip

σ_{0y}^{reg}: $t'_a(\sigma_x,\sigma_y) = t'_{a0}(\sigma_{0y}^{\text{reg}})$, $t'_s(\sigma_x,\sigma_y) = t'_{s0}(\sigma_{0y}^{\text{reg}})$. By using (59) and (65a)

$$\begin{aligned}
M'_z(\sigma_x,\sigma_y) &= t'_s(\sigma_x,\sigma_y)F_{sy}(\sigma_x,\sigma_y) + t'_a(\sigma_x,\sigma_y)F_{ay}(\sigma_x,\sigma_y) \\
&= t'_{0s}(\sigma_{0y}^{\text{reg}})F_{0sy}(\sigma_{0y}^{\text{reg}})\frac{F_{sy}(\sigma_x,\sigma_y)}{F_{0sy}(\sigma_{0y}^{\text{reg}})} + t'_{0a}(\sigma_{0y}^{\text{reg}})F_{0ay}(\sigma_{0y}^{\text{reg}})\frac{F_{ay}(\sigma_x,\sigma_y)}{F_{0ay}(\sigma_{0y}^{\text{reg}})} \\
&= M_{0sz}(\sigma_{0y}^{\text{reg}})\sin(\beta) + t'_{0a}(\sigma_{0y}^{\text{reg}})F_{0ay}(\sigma_{0y}^{\text{reg}})\sin(\beta^\circ) \\
&= (M_{0z}(\sigma_{0y}^{\text{reg}}) - t'_{0a}(\sigma_{0y}^{\text{reg}})F_{0ay}(\sigma_{0y}^{\text{reg}}))\sin(\beta) + t'_{0a}(\sigma_{0y}^{\text{reg}})F_{0ay}(\sigma_{0y}^{\text{reg}})\sin(\beta^\circ) \\
&= M_{0z}(\sigma_{0y}^{\text{reg}})\sin(\beta) + t'_{0a}(\sigma_{0y}^{\text{reg}})(1-\theta_y(\sigma_{0y}^{\text{reg}}))F_{0y}(\sigma_{0y}^{\text{reg}})(\sin(\beta^\circ) - \sin(\beta)) \quad (141)
\end{aligned}$$

where Properties 8 and 9 have been used in the third equality. The contact length a in (65a) may be computed from (66) as

$$a = \frac{3C_z}{C_y} \tag{142}$$

□

A.13 Proof of Property 15

Proof. For the adhesion part M''_{az} of the deformation torque the expressions for the adhesion forces given by Property 8 are inserted in (61). The factor $(1-\psi(\sigma_x,\sigma_y))$ present in the denominator of (61) and in the numerator of θ_x and θ_y can then be cancelled and no numerical problems arises for small slips in the final formula. The slide part (M''_{sz}) is given by (62) and the slide forces by Property 9. Again, the factor $\psi(\sigma_x,\sigma_y)$ present in the denominator of (62) and in the numerator of $1-\theta_x$ and $1-\theta_y$ can then be cancelled and no numerical problems arises for small slips in the final formula. □

A.14 Proof of Property 16

Proof. For the adhesive part (M''_{az}) of the deformation torque the expressions for the adhesive forces given by Property 5 are inserted in (61). The denominator $(1-\psi(\sigma_x,\sigma_y))$ in (61) will then be cancelled and no numerically problems can arise. The sliding part (M''_{sz}) is given by (62) and the sliding forces are derived by using Property 11. The factor $\psi(\sigma_x,\sigma_y)$ in the denominator of (62) can be cancelled by breaking out $\psi(0,\sigma_{0y}^{\text{reg}})$ from $\theta_y(\sigma_{0y}^{\text{reg}})$. □

B. Slip translations

This appendix deals with details regarding the practical computation of the pure-slips in the models when λ and α are used instead of σ_x and σ_y. Using (7) a combined slip (λ,α) is translated to the combined slip (σ_x,σ_y) as

$$\sigma_x = \frac{\lambda}{1-\lambda} \tag{143a}$$

$$\sigma_y = \frac{\tan(\alpha)}{1-\lambda} \tag{143b}$$

The condition for partial sliding is then expressed in λ and α as

$$\psi(\sigma_x,\sigma_y) < 1 \Longleftrightarrow \left(\frac{\lambda}{\sigma_x^\circ}\cos(\alpha)\right)^2 + \left(\frac{\sin(\alpha)}{\sigma_y^\circ}\right)^2 < (1-\lambda)^2\cos^2(\alpha) \tag{144}$$

The pure slips $(\lambda_0, 0)$ and $(0, \alpha_0)$ are translated to the pure slips $(\sigma_{0x}, 0)$ and $(0, \sigma_{0y})$ as

$$\sigma_{0x} = \frac{\lambda_0}{1-\lambda_0} \tag{145a}$$
$$\sigma_{0y} = \tan(\alpha_0) \tag{145b}$$

Since the limit slips are pure slips they are translated as

$$\sigma_x^\circ = \frac{\lambda^\circ}{1-\lambda^\circ} \tag{146a}$$
$$\sigma_y^\circ = \tan(\alpha^\circ) \tag{146b}$$

Also from (7) it is clear that the combined slip (σ_x, σ_y) corresponds to the combined slip (λ, α) given by

$$\lambda = \frac{\sigma_x}{1+\sigma_x} \tag{147a}$$
$$\tan(\alpha) = \frac{\sigma_y}{1+\sigma_x} \tag{147b}$$

Hence, the pure slips $(\sigma_{0x}, 0)$ and $(0, \sigma_{0y})$ correspond to the combined slips $(\lambda_0, 0)$ and $(0, \alpha_0)$ given by

$$\lambda_0 = \frac{\sigma_{0x}}{1+\sigma_{0x}} \tag{148a}$$
$$\tan(\alpha_0) = \sigma_{0y} \tag{148b}$$

Note that in the following when solving for α_0 using this last expression it will be necessary to use the function $\operatorname{atan2}(y, x)$ which is standard in most computer languages (e.g. C, Matlab) and returns $\arctan(y/x)$ without performing the possibly singular division.

B.1 Deformation-invariant pure slips

$$\sigma_{0x} = \sigma_x = \frac{\lambda}{1-\lambda} \tag{149a}$$
$$\sigma_{0y} = \sigma_y = \frac{\tan(\alpha)}{1-\lambda} \tag{149b}$$

$$\lambda_0 = \frac{\sigma_{0x}}{1+\sigma_{0x}} = \lambda \tag{150a}$$
$$\tan(\alpha_0) = \sigma_{0y} = \frac{\tan(\alpha)}{1-\lambda} = \frac{\sin(\alpha)}{(1-\lambda)\cos(\alpha)} \tag{150b}$$

$$\psi(\sigma_x, 0) < 1 \Longleftrightarrow |\lambda| < \sigma_x^\circ |1-\lambda| \tag{151a}$$
$$\psi(0, \sigma_y) < 1 \Longleftrightarrow |\sin(\alpha)| < \sigma_y^\circ |(1-\lambda)\cos(\alpha)| \tag{151b}$$

B.2 Region-invariant pure slips

$$\sigma_{0x}^{\text{reg}} = \sigma_x^\circ \psi(\sigma_x, \sigma_y) = \sigma_x^\circ \sqrt{\left(\frac{\lambda}{1-\lambda}\frac{1}{\sigma_x^\circ}\right)^2 + \left(\frac{\tan(\alpha)}{1-\lambda}\frac{1}{\sigma_y^\circ}\right)^2}\,\operatorname{sgn}(\lambda) \tag{152a}$$

$$\sigma_{0y}^{\text{reg}} = \sigma_y^\circ \psi(\sigma_x, \sigma_y) = \sigma_y^\circ \sqrt{\left(\frac{\lambda}{1-\lambda}\frac{1}{\sigma_x^\circ}\right)^2 + \left(\frac{\tan(\alpha)}{1-\lambda}\frac{1}{\sigma_y^\circ}\right)^2}\,\operatorname{sgn}(\alpha) \tag{152b}$$

$$\lambda_0^{\text{reg}} = \frac{\sigma_{0x}^{\text{reg}}}{1+\sigma_{0x}^{\text{reg}}} = \frac{\sigma_x^\circ \sqrt{\left(\frac{\lambda\cos(\alpha)}{\sigma_x^\circ}\right)^2 + \left(\frac{\sin(\alpha)}{\sigma_y^\circ}\right)^2}\,\text{sgn}\,(\lambda)}{(1-\lambda)\,|\cos(\alpha)| + \sigma_x^\circ \sqrt{\left(\frac{\lambda\cos(\alpha)}{\sigma_x^\circ}\right)^2 + \left(\frac{\sin(\alpha)}{\sigma_y^\circ}\right)^2}\,\text{sgn}\,(\lambda)} \tag{153a}$$

$$\tan(\alpha_0^{\text{reg}}) = \sigma_{0y}^{\text{reg}} = \frac{\sigma_y^\circ \sqrt{\left(\frac{\lambda\cos(\alpha)}{\sigma_x^\circ}\right)^2 + \left(\frac{\sin(\alpha)}{\sigma_y^\circ}\right)^2}}{(1-\lambda)|\cos(\alpha)|}\text{sgn}\,(\alpha) \tag{153b}$$

Since $\psi(\sigma_{0x}^{\text{reg}}, 0) = \psi(0, \sigma_{0y}^{\text{reg}}) = \psi(\sigma_x, \sigma_y)$ the conditions for partial sliding are equivalent to (144).

B.3 Slip-velocity invariant pure slips

$$\sigma_{0x}^{\text{vel}} = \frac{v\sqrt{(\lambda\cos(\alpha))^2 + \sin^2(\alpha)}\,\text{sgn}\,(\lambda)}{v_0 - v\sqrt{(\lambda\cos(\alpha))^2 + \sin^2(\alpha)}\,\text{sgn}\,(\lambda)} \tag{154a}$$

$$\sigma_{0y}^{\text{vel}} = \frac{v\sqrt{(\lambda\cos(\alpha))^2 + \sin^2(\alpha)}}{\sqrt{v_0^2 - v^2\left((\lambda\cos(\alpha))^2 + \sin^2(\alpha)\right)}}\text{sgn}\,(\alpha) \tag{154b}$$

$$\lambda_0^{\text{vel}} = \frac{v}{v_0}\sqrt{(\lambda\cos(\alpha))^2 + \sin^2(\alpha)}\,\text{sgn}\,(\lambda) \tag{155a}$$

$$\sin(\alpha_0^{\text{vel}}) = \frac{v}{v_0}\sqrt{(\lambda\cos(\alpha))^2 + \sin^2(\alpha)}\,\text{sgn}\,(\alpha) \tag{155b}$$

$$\psi(\sigma_{0x}^{\text{vel}}, 0) < 1 \iff v\sqrt{(\lambda\cos(\alpha))^2 + \sin^2(\alpha)} < \sigma_x^\circ |v_0 - v\sqrt{(\lambda\cos(\alpha))^2 + \sin^2(\alpha)}\,\text{sgn}\,(\lambda)| \tag{156a}$$

$$\psi(0, \sigma_{0y}^{\text{vel}}) < 1 \iff v\sqrt{(\lambda\cos(\alpha))^2 + \sin^2(\alpha)} < \sigma_y^\circ\sqrt{v_0^2 - v^2\left((\lambda\cos(\alpha))^2 + \sin^2(\alpha)\right)} \tag{156b}$$

B.4 Slip-velocity component invariant pure slips

$$\sigma_{0x}^{\text{velc}} = \frac{v\lambda\cos(\alpha)}{v_0 - \lambda v\cos(\alpha)} \tag{157a}$$

$$\sigma_{0y}^{\text{velc}} = \frac{v\sin(\alpha)}{\sqrt{v_0^2 - (v\sin(\alpha))^2}} \tag{157b}$$

$$\lambda_0^{\text{velc}} = \lambda\cos(\alpha)\frac{v}{v_0} \tag{158a}$$

$$\tan(\alpha_0^{\text{velc}}) = \frac{v\sin(\alpha)}{\sqrt{v_0^2 - (v\sin(\alpha))^2}} \tag{158b}$$

$$\psi(\sigma_{0x}^{\text{velc}}, 0) < 1 \iff |v\lambda\cos(\alpha)| < \sigma_x^\circ |v_0 - \lambda v\cos(\alpha)| \tag{159a}$$

$$\psi(0, \sigma_{0y}^{\text{velc}}) < 1 \iff |v\sin(\alpha)| < \sigma_y^\circ\sqrt{v_0^2 - (v\sin(\alpha))^2} \tag{159b}$$

C. Derivation of non-singular expressions

In the proofs of some of the properties in Section 3 the expressions $\cos(\beta)/\cos(\beta^\circ)$ and $\sin(\beta)/\sin\beta^\circ$ appear. Computation of the expressions in this form may be singular, but by rewriting them as follows numerically feasible expressions are obtained. Recall that β is the angle of the slip vector

$$\cos(\beta) = \frac{\sigma_x}{\sqrt{\sigma_x^2+\sigma_y^2}} \tag{160}$$

$$\sin(\beta) = \frac{\sigma_y}{\sqrt{\sigma_x^2+\sigma_y^2}} \tag{161}$$

Also recall that β° is the angle of the normalized slip vector

$$\cos(\beta^\circ) = \frac{|\sigma_x|}{\sigma_x^\circ\sqrt{\left(\frac{\sigma_x}{\sigma_x^\circ}\right)^2+\left(\frac{\sigma_y}{\sigma_y^\circ}\right)^2}} \tag{162}$$

$$\sin(\beta^\circ) = \frac{|\sigma_y|}{\sigma_y^\circ\sqrt{\left(\frac{\sigma_x}{\sigma_x^\circ}\right)^2+\left(\frac{\sigma_y}{\sigma_y^\circ}\right)^2}} \tag{163}$$

Hence,

$$\begin{aligned}
\frac{\cos(\beta)}{\cos\beta^\circ} &= \frac{\sigma_x}{\sqrt{\sigma_x^2+\sigma_y^2}}\frac{\sigma_x^\circ\sqrt{\left(\frac{\sigma_x}{\sigma_x^\circ}\right)^2+\left(\frac{\sigma_y}{\sigma_y^\circ}\right)^2}}{|\sigma_x|} \\
&= \operatorname{sgn}(\sigma_x)\frac{\sigma_x^\circ\left(\left(\frac{\sigma_x}{\sigma_x^\circ}\right)^2+\left(\frac{\sigma_y}{\sigma_y^\circ}\right)^2\right)}{\sqrt{\sigma_x^2+\sigma_y^2}\sqrt{\left(\frac{\sigma_x}{\sigma_x^\circ}\right)^2+\left(\frac{\sigma_y}{\sigma_y^\circ}\right)^2}} \\
&= \operatorname{sgn}(\sigma_x)\left(\frac{|\sigma_x|}{\sqrt{\sigma_x^2+\sigma_y^2}}\frac{|\sigma_x|}{\sigma_x^\circ\sqrt{\left(\frac{\sigma_x}{\sigma_x^\circ}\right)^2+\left(\frac{\sigma_y}{\sigma_y^\circ}\right)^2}}\right. \\
&\quad \left. + \frac{\sigma_x^\circ}{\sigma_y^\circ}\frac{|\sigma_y|}{\sigma_y^\circ\sqrt{\sigma_x^2+\sigma_y^2}}\frac{|\sigma_y|}{\sigma_y^\circ\sqrt{\left(\frac{\sigma_x}{\sigma_x^\circ}\right)^2+\left(\frac{\sigma_y}{\sigma_y^\circ}\right)^2}}\right) \\
&= \operatorname{sgn}(\sigma_x)\sigma_x^\circ\left(\frac{1}{\sigma_x^\circ}|\cos(\beta)|\cos(\beta^\circ)+\frac{1}{\sigma_y^\circ}|\sin(\beta)|\sin(\beta^\circ)\right)
\end{aligned} \tag{164}$$

and likewise

$$\frac{\sin(\beta)}{\sin\beta^\circ} = \operatorname{sgn}(\sigma_y)\sigma_y^\circ\left(\frac{1}{\sigma_x^\circ}|\cos(\beta)|\cos(\beta^\circ)+\frac{1}{\sigma_y^\circ}|\sin(\beta)|\sin(\beta^\circ)\right) \tag{165}$$

D. Validation plots

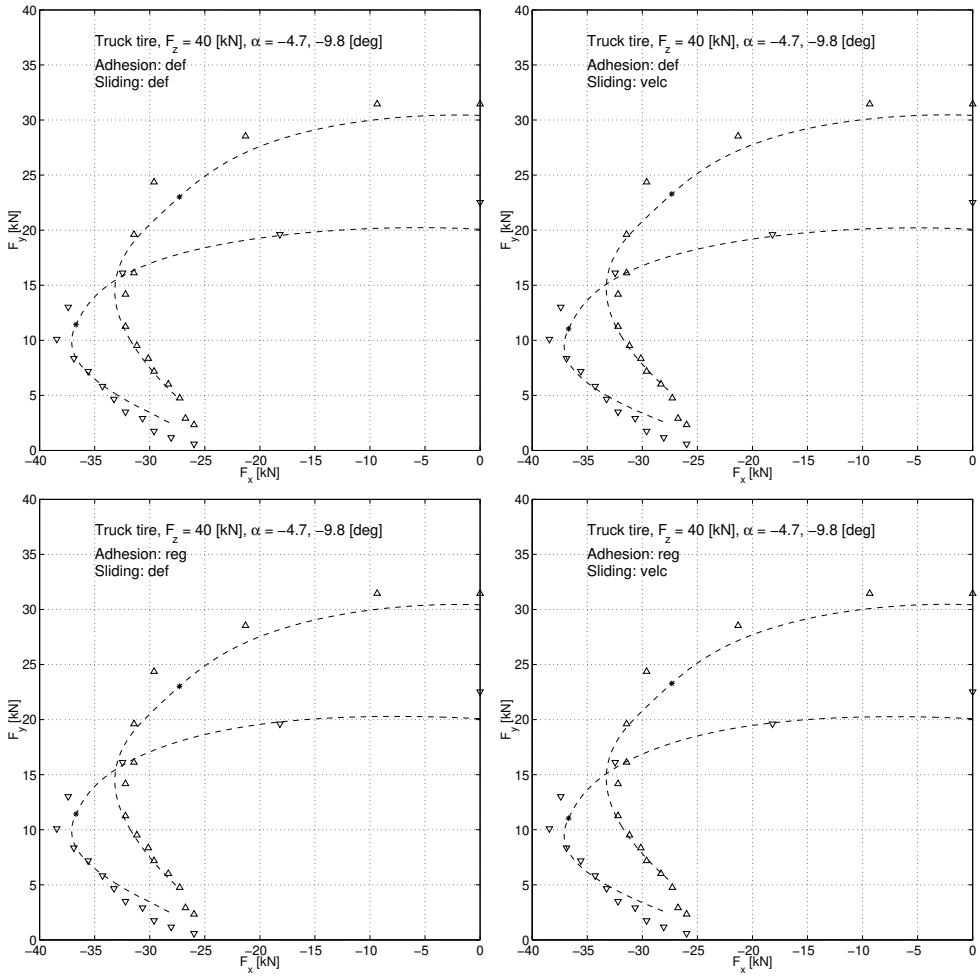

Figure 31 validation

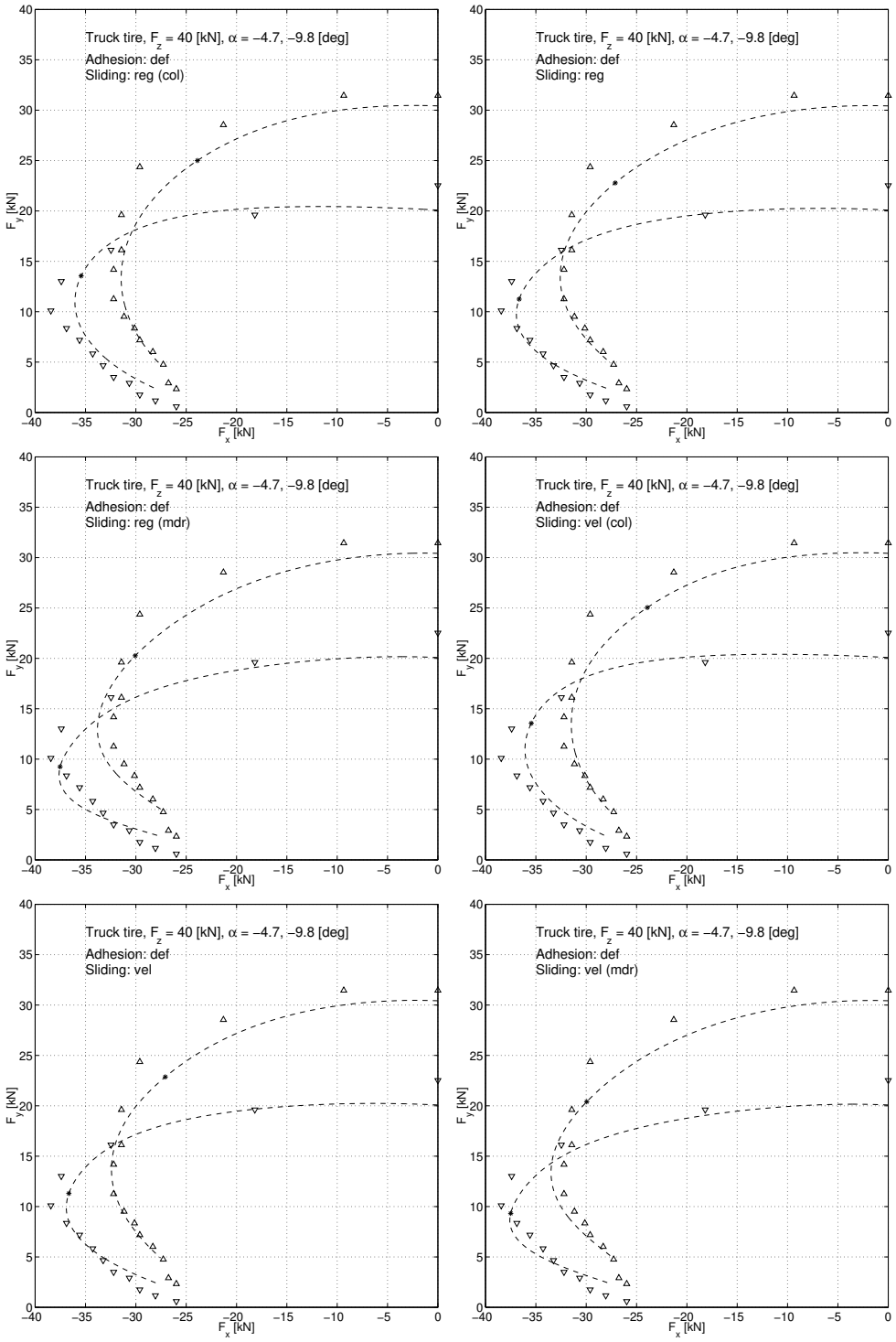

Figure 32 validation

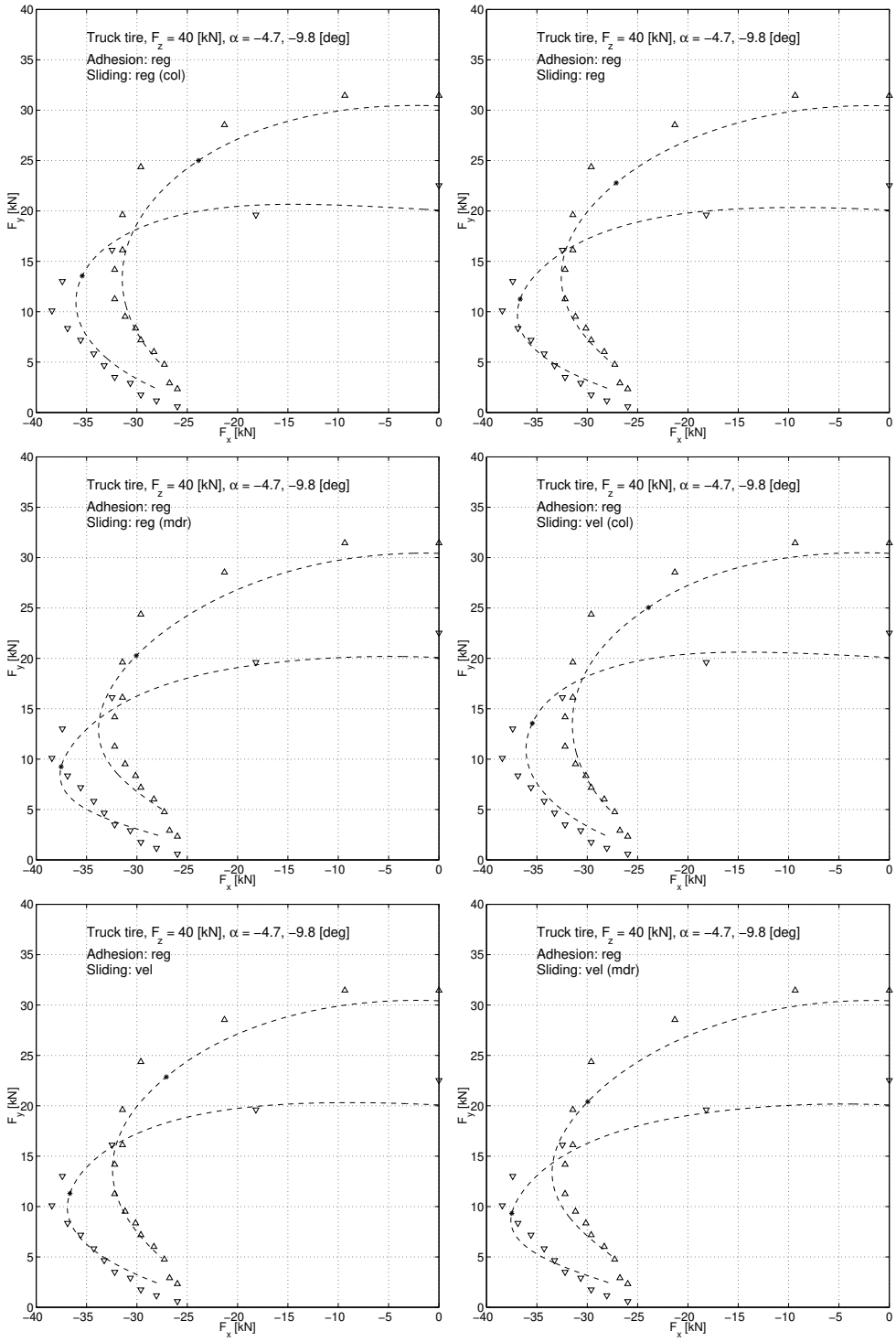

Figure 33 validation

E. Pseudo-Code Implementations

Algorithm 1 Pseudo-code implementation of the semi-empirical deformation-invariant adhesion-force model based on Property 5.

Require: λ, α, $(B, C, D, E)_{x,y}$
Produces: $\hat{F}_{ax}(\lambda, \alpha)$, $\hat{F}_{ay}(\lambda, \alpha)$
  if $\psi(\sigma_x, \sigma_y) < 1$ (144) **then**
    σ_x, $\sigma_y \Leftarrow \lambda$, α, (143)
    σ_x°, $\sigma_y^\circ \Leftarrow (B, C, D)_{x,y}$, (94a), (105)
    $\psi(\sigma_x, \sigma_y) \Leftarrow \sigma_x$, σ_y, σ_x°, σ_y°, (33)
    λ_0, $\alpha_0 \Leftarrow \lambda$, α, (150)
    $\hat{F}_{0x}(\lambda_0)$, $\hat{F}_{0y}(\alpha_0) \Leftarrow \lambda_0$, α_0, $(B, C, D, E)_{x,y}$, (12), (108)
    σ_{0x}, $\sigma_{0y} \Leftarrow \lambda$, α, (149)
    $\psi(\sigma_{0x}, 0)$, $\psi(0, \sigma_{0y}) \Leftarrow \sigma_{0x}$, σ_{0y}, σ_x°, σ_y°, (33)
    $\hat{F}_{ax}(\lambda, \alpha)$, $\hat{F}_{ay}(\lambda, \alpha) \Leftarrow \hat{F}_{0x}(\lambda_0)$, $\hat{F}_{0y}(\alpha_0)$, $\psi(\sigma_x, \sigma_y)$, $\psi(\sigma_{0x}, 0)$, $\psi(0, \sigma_{0y})$, (74)
  else
    $\hat{F}_{ax}(\lambda, \alpha) := 0$ and $\hat{F}_{ay}(\lambda, \alpha) := 0$
  end if

Algorithm 2 Pseudo-code implementation of the semi-empirical slip-velocity invariant slide-force model based on Property 11.

Require: λ, α, $(B, C, D, E)_{x,y}$, v/v_0
Produces: $\hat{F}_{sx}(\lambda, \alpha)$, $\hat{F}_{sy}(\lambda, \alpha)$
  λ_0^{vel}, $\alpha_0^{\text{vel}} \Leftarrow \lambda$, α, (155)
  $\hat{F}_{0x}(\lambda_0^{\text{vel}})$, $\hat{F}_{0y}(\alpha_0^{\text{vel}}) \Leftarrow \lambda_0^{\text{vel}}$, α_0^{vel}, $(B, C, D, E)_{x,y}$, (12)
  σ_x°, $\sigma_y^\circ \Leftarrow (B, C, D)_{x,y}$, (94a), (105)
  $\beta \Leftarrow \lambda$, α, (4)
  if $\psi(\sigma_x, \sigma_y) < 1$ (144) **then**
    σ_x, $\sigma_y \Leftarrow \lambda$, α, (143)
    $\psi(\sigma_x, \sigma_y)$, $\psi(\sigma_x, 0)$, $\psi(0, \sigma_y) \Leftarrow \sigma_x$, σ_y, σ_x°, σ_y°, (33)
    $\beta^\circ \Leftarrow \psi(\sigma_x, 0)$, $\psi(0, \sigma_y)$, (34)
  end if
  if $\psi(\sigma_{0x}^{\text{vel}}, 0) < 1$ (156) **then**
    $\sigma_{0x}^{\text{vel}} \Leftarrow \alpha$, λ, (154a)
    $\psi(\sigma_{0x}^{\text{vel}}, 0) \Leftarrow \sigma_{0x}^{\text{vel}}$ (33)
    $\theta_x(\sigma_{0x}^{\text{vel}}) \Leftarrow \sigma_{0x}^{\text{vel}}$ (70)
  else
    $\theta_x(\sigma_{0x}^{\text{vel}}) := 1$
  end if
  if $\psi(0, \sigma_{0y}^{\text{vel}}) < 1$ (156) **then**
    $\sigma_{0y}^{\text{vel}} \Leftarrow \alpha$, λ, (154a)
    $\psi(0, \sigma_{0y}^{\text{vel}}) \Leftarrow \sigma_{0y}^{\text{vel}}$ (33)
    $\theta_y(\sigma_{0y}^{\text{vel}}) \Leftarrow \sigma_{0y}^{\text{vel}}$ (70)
  else
    $\theta_y(\sigma_{0y}^{\text{vel}}) := 1$
  end if
  Γ_x^{vel}, $\Gamma_y^{\text{vel}} \Leftarrow \sigma_x$, σ_y, σ_x°, σ_y°, β, β°, $\psi(\sigma_x, \sigma_y)$, $\psi(\sigma_{0x}^{\text{vel}}, 0)$, $\psi(0, \sigma_{0y}^{\text{vel}})$, v/v_0 (82)
  $\hat{F}_{0sx}(\lambda_0^{\text{vel}}) := \theta_x(\sigma_{0x}^{\text{vel}}) \hat{F}_{0x}(\lambda_0^{\text{vel}}) \Gamma_x^{\text{vel}}$
  $\hat{F}_{0sy}(\alpha_0^{\text{vel}}) := \theta_y(\sigma_{0y}^{\text{vel}}) \hat{F}_{0y}(\alpha_0^{\text{vel}}) \Gamma_y^{\text{vel}}$
  $\beta_f \Leftarrow \lambda$, α, $\hat{F}_{0sx}(\lambda_0^{\text{vel}})$, $\hat{F}_{0sy}(\alpha_0^{\text{vel}})$, (42) using $\mu_{sx}/\mu_{sy} = \hat{F}_{0sx}(\lambda_0^{\text{vel}})/\hat{F}_{0sy}(\alpha_0^{\text{vel}})$ and $v_{sy}/v_{sx} = \sin(\alpha)/(\lambda \cos(\alpha))$.
  $\hat{F}_{sx}(\lambda, \alpha)$, $\hat{F}_{sy}(\lambda, \alpha) \Leftarrow \hat{F}_{0x}(\lambda_0^{\text{vel}})$, $\hat{F}_{0y}(\alpha_0^{\text{vel}})$, $\theta_x(\sigma_{0x}^{\text{reg}})$, $\theta_y(\sigma_{0y}^{\text{reg}})$, β_f, (81)

Algorithm 3 Pseudo-code implementation of the semi-empirical region-invariant adhesion-force model based on Property 8.

Require: λ, α, $(B,C,D,E)_{x,y}$
Produces: $\hat{F}_{ax}(\lambda,\alpha)$, $\hat{F}_{ay}(\lambda,\alpha)$
  if $\psi(\sigma_x,\sigma_y) < 1$ (144) **then**
    λ_0^{reg}, $\alpha_0^{\text{reg}} \Leftarrow \lambda$, α, (153)
    $\hat{F}_{0x}(\lambda_0^{\text{reg}})$, $\hat{F}_{0y}(\alpha_0^{\text{reg}}) \Leftarrow \lambda_0^{\text{reg}}$, α_0^{reg}, $(B,C,D,E)_{x,y}$, (12), (108)
    σ_x°, $\sigma_y^\circ \Leftarrow (B,C,D)_{x,y}$, (94a), (105)
    σ_x, $\sigma_y \Leftarrow \lambda$, α, (143)
    $\psi(\sigma_x,\sigma_y)$, $\psi(\sigma_x,0)$, $\psi(0,\sigma_y) \Leftarrow \sigma_x$, σ_y, σ_x°, σ_y°, (33)
    $\beta^\circ \Leftarrow \psi(\sigma_x,0)$, $\psi(0,\sigma_y)$, (34)
    σ_{0x}^{reg}, $\sigma_{0y}^{\text{reg}} \Leftarrow \psi(\sigma_x,\sigma_y)$, σ_x°, σ_y°, (77)
    $\theta_x(\sigma_{0x}^{\text{reg}})$, $\theta_y(\sigma_{0y}^{\text{reg}}) \Leftarrow \sigma_{0x}^{\text{reg}}$, σ_{0y}^{reg}, (70)
    $\hat{F}_{ax}(\lambda,\alpha)$, $\hat{F}_{ay}(\lambda,\alpha) \Leftarrow \hat{F}_{0x}(\lambda_0^{\text{reg}})$, $\hat{F}_{0y}(\alpha_0^{\text{reg}})$, β°, $\theta_x(\sigma_{0x}^{\text{reg}})$, $\theta_y(\sigma_{0y}^{\text{reg}})$, (78)
  else
    $\hat{F}_{ax}(\lambda,\alpha) := 0$ and $\hat{F}_{ay}(\lambda,\alpha) := 0$
  end if

Algorithm 4 Pseudo-code implementation of the semi-empirical region-invariant sliding-force model based on Property 9.

Require: λ, α, $(B,C,D,E)_{x,y}$
Produces: $\hat{F}_{sx}(\lambda,\alpha)$, $\hat{F}_{sy}(\lambda,\alpha)$
  λ_0^{reg}, $\alpha_0^{\text{reg}} \Leftarrow \lambda$, α, (153)
  $\hat{F}_{0x}(\lambda_0^{\text{reg}})$, $\hat{F}_{0y}(\alpha_0^{\text{reg}}) \Leftarrow \lambda_0^{\text{reg}}$, α_0^{reg}, $(B,C,D,E)_{x,y}$, (12)
  σ_x°, $\sigma_y^\circ \Leftarrow (B,C,D)_{x,y}$, (94a), (105)
  if $\psi(\sigma_x,\sigma_y) < 1$ (144) **then**
    σ_x, $\sigma_y \Leftarrow \lambda$, α, (143)
    $\psi(\sigma_x,\sigma_y) \Leftarrow \sigma_x$, σ_y, σ_x°, σ_y°, (33)
    σ_{0x}^{reg}, $\sigma_{0y}^{\text{reg}} \Leftarrow \psi(\sigma_x,\sigma_y)$, σ_x°, σ_y°, (77)
    $\theta_x(\sigma_{0x}^{\text{reg}})$, $\theta_y(\sigma_{0y}^{\text{reg}}) \Leftarrow \sigma_{0x}^{\text{reg}}$, σ_{0y}^{reg}, (70)
  else
    $\theta_x(\sigma_{0x}^{\text{reg}}) := 1$ and $\theta_y(\sigma_{0y}^{\text{reg}}) := 1$
  end if
  $\hat{F}_{0sx}(\lambda_0^{\text{reg}}) := \theta_x(\sigma_{0x}^{\text{reg}})\hat{F}_{0x}(\lambda_0^{\text{reg}})$
  $\hat{F}_{0sy}(\alpha_0^{\text{reg}}) := \theta_y(\sigma_{0y}^{\text{reg}})\hat{F}_{0y}(\alpha_0^{\text{reg}})$
  $\beta_f \Leftarrow \lambda$, α, $\hat{F}_{0sx}(\lambda_0^{\text{reg}})$, $\hat{F}_{0sy}(\alpha_0^{\text{reg}})$, (42) Using $\mu_{sx}/\mu_{sy} = \hat{F}_{0sx}(\lambda_0^{\text{reg}})/\hat{F}_{0sy}(\alpha_0^{\text{reg}})$ and $v_{sy}/v_{sx} = \sin(\alpha)/(\lambda\cos(\alpha))$
  $\hat{F}_{sx}(\lambda,\alpha)$, $\hat{F}_{sy}(\lambda,\alpha) \Leftarrow \hat{F}_{0x}(\lambda_0^{\text{reg}})$, $\hat{F}_{0y}(\alpha_0^{\text{reg}})$, $\theta_x(\sigma_{0x}^{\text{reg}})$, $\theta_y(\sigma_{0y}^{\text{reg}})$, β_f, (79)

Algorithm 5 Pseudo-code implementation of the semi-empirical region-invariant aligning-moment model based on Property 14.

Require: λ, α, $(B,C,D,E)_{y,z}$
Produces: $\hat{M}_z(\lambda,\alpha)$
  $\alpha_0^{\text{reg}} \Leftarrow \lambda$, α, (153)
  $\hat{F}_{0y}(\alpha_0^{\text{reg}})$, $\hat{M}_{0z}(\alpha_0^{\text{reg}}) \Leftarrow \alpha_0^{\text{reg}}$, $(B,C,D,E)_{y,z}$, (12)
  σ_x°, $\sigma_y^\circ \Leftarrow (B,C,D)_{x,y}$, (94a), (105)
  $\beta \Leftarrow \lambda$, α, (4)
  if $\psi(\sigma_x,\sigma_y) < 1$ (144) **then**
    σ_x, $\sigma_y \Leftarrow \lambda$, α, (143)
    $\psi(\sigma_x,\sigma_y)$, $\psi(\sigma_x,0)$, $\psi(0,\sigma_y) \Leftarrow \sigma_x$, σ_y, σ_x°, σ_y°, (33)
    $\beta^\circ \Leftarrow \psi(\sigma_x,0)$, $\psi(0,\sigma_y)$, (34)
    $\sigma_{0y}^{\text{reg}} \Leftarrow \psi(\sigma_x,\sigma_y)$, σ_y°, (77)
    $\theta_y(\sigma_{0y}^{\text{reg}}) \Leftarrow \sigma_{0y}^{\text{reg}}$, (70)
    $t_{0\alpha}(\sigma_{0y}^{\text{reg}}) \Leftarrow \psi(\sigma_x,\sigma_y)$, $(B,C,D)_y$, $(B,C,D)_z$, (87)
    $\hat{M}_z'(\lambda,\alpha) \Leftarrow \sigma_{0y}^{\text{reg}}$, β, β°, $\hat{F}_{0y}(\alpha_0^{\text{reg}})\,\theta_y(\sigma_{0y}^{\text{reg}})$, $t_{0\alpha}(\sigma_{0y}^{\text{reg}})$, (86)
  else
    $\hat{M}_z'(\lambda,\alpha) := \hat{M}_{0z}(\alpha_0^{\text{reg}})\sin(\beta)$, (86)
  end if

Algorithm 6 Pseudo-code implementation of the semi-empirical region-invariant additional aligning-moment model based on Property 15.

Require: λ, α, $(B, C, D, E)_{x,y}$
Produces: $\hat{M}_z(\lambda, \alpha)$
  λ_0^{reg}, $\alpha_0^{\text{reg}} \Leftarrow \lambda$, α, (153)
  $\hat{F}_{0x}(\lambda_0^{\text{reg}})$, $\hat{F}_{0y}(\alpha_0^{\text{reg}}) \Leftarrow \lambda_0^{\text{reg}}$, α_0^{reg}, $(B, C, D, E)_{x,y}$, (12)
  σ_x°, $\sigma_y^\circ \Leftarrow (B, C, D)_{x,y}$, (94a), (105)
  if $\psi(\sigma_x, \sigma_y) < 1$ (144) **then**
    σ_x, $\sigma_y \Leftarrow \lambda$, α, (143)
    $\psi(\sigma_x, \sigma_y)$, $\psi(\sigma_x, 0)$, $\psi(0, \sigma_y) \Leftarrow \sigma_x$, σ_y, σ_x°, σ_y°, (33)
    σ_{0x}^{reg}, $\sigma_{0y}^{\text{reg}} \Leftarrow \psi(\sigma_x, \sigma_y)$, σ_x°, σ_y°, (77)
    $\theta_x(\sigma_{0x}^{\text{reg}})$, $\theta_y(\sigma_{0y}^{\text{reg}}) \Leftarrow \sigma_{0x}^{\text{reg}}$, σ_{0y}^{reg}, (70)
    Γ_{zx}, Γ_{zy}, $\Gamma_z, \Leftarrow \psi(\sigma_x, \sigma_y)$, (89)
    $M''_{az}(\lambda, \alpha) \Leftarrow \psi(\sigma_x, \sigma_y)$, $\hat{F}_{0x}(\lambda_0^{\text{reg}})$, $\hat{F}_{0y}(\alpha_0^{\text{reg}})$, (88)
  else
    $\theta_x(\sigma_{0x}^{\text{reg}}) := 1$, $\theta_y(\sigma_{0y}^{\text{reg}}) := 1$
    $\Gamma_{zx} := 1$, $\Gamma_{zy} := 1$, $\Gamma_z := 1$
    $M''_{az}(\lambda, \alpha) := 0$
  end if
  $\hat{F}_{0sx}(\lambda_0^{\text{reg}}) := \theta_x(\sigma_{0x}^{\text{reg}})\hat{F}_{0x}(\lambda_0^{\text{reg}})$
  $\hat{F}_{0sy}(\alpha_0^{\text{reg}}) := \theta_y(\sigma_{0y}^{\text{reg}})\hat{F}_{0y}(\alpha_0^{\text{reg}})$
  $\beta_f \Leftarrow \lambda$, α, $\hat{F}_{0sx}(\lambda_0^{\text{reg}})$, $\hat{F}_{0sy}(\alpha_0^{\text{reg}})$, (42) using $\mu_{sx}/\mu_{sy} = \hat{F}_{0sx}(\lambda_0^{\text{reg}})/\hat{F}_{0sy}(\alpha_0^{\text{reg}})$ and $v_{sy}/v_{sx} = sin(\alpha)/(\lambda \cos(\alpha))$.
  $M''_{sz}(\lambda, \alpha) \Leftarrow \hat{F}_{0x}(\lambda_0^{\text{reg}})$, $\hat{F}_{0y}(\alpha_0^{\text{reg}})$, β_f, Γ_{zx}, Γ_{zy}, Γ_z, (88)
  $\hat{M}''_z(\lambda, \alpha) := \hat{M}''_{az}(\lambda, \alpha) + \hat{M}''_{sz}(\lambda, \alpha)$